

Optical Signal Processing and Pulse Shaping for Wavelength Multiplexed High Speed Communication Systems

THÈSE N° 6997 (2016)

PRÉSENTÉE LE 29 JUIN 2016

À LA FACULTÉ DES SCIENCES ET TECHNIQUES DE L'INGÉNIEUR
LABORATOIRE DE SYSTÈMES PHOTONIQUES
PROGRAMME DOCTORAL EN PHOTONIQUE

ÉCOLE POLYTECHNIQUE FÉDÉRALE DE LAUSANNE

POUR L'OBTENTION DU GRADE DE DOCTEUR ÈS SCIENCES

PAR

Mohammad Amin SHOAIE

acceptée sur proposition du jury:

Prof. J.-E. Moser, président du jury
Prof. C. S. Brès, directrice de thèse
Prof. J. Fatome, rapporteur
Prof. K. K. Wong, rapporteur
Prof. L. Thévenaz, rapporteur



ÉCOLE POLYTECHNIQUE
FÉDÉRALE DE LAUSANNE

Suisse
2016

Have no fear of perfection
you will never reach it.
— Salvador Dali

To my dear family for their unconditional love and support.

Acknowledgements

I spent four years of my life at EPFL working on the PhD thesis. During this period I faced desperate and stressed times but also joyful and gracious moments. Here I take the opportunity to express my gratitude to people who supported me in this path.

First of all, I would like to express my deepest gratitude to my thesis director, Prof. Camille-Sophie Brès for her invaluable help and support. Camille gave me the freedom to explore on my research independently, while guiding me into right direction. I admit that her strong perseverance and high ambitious significantly leveraged my professional skills.

My sincere thanks goes to the president of jury, Prof. Jacques-Edouard Moser and the jury members, Prof. Luc Thévenaz, Prof. Julien Fatome and Prof. Kenneth K.Y. Wong for reviewing and commenting on my work.

I would like to extend my appreciation to my former and new colleagues and friends in PHOSL laboratory who provided an excellent and delightful atmosphere for me during my doctoral study (listed in order of appearance to me): Adrien Billat, Dr. Steevy Joyce Cordette, Svyatoslav Kharitonov, Deniz Aydin, Yu-Pei Tseng, Dr. Davide Grassani, Sida Xing and Dr. Thibault North. I also appreciate our past and current lab secretary, Corinne Dubois and Françoise Behn for helping me through the paper works during my stay at EPFL.

The special thanks goes to my dearest friend, Dr. Armand Vedadi who persuaded me to start the PhD and mentored me in past few years. Indeed, not only he was a great teacher while transferring me his deep knowledge, but also he helped me out several times with my problems outside the lab (damet garm dadash).

I would like also to thank my friends in Lausanne with whom I have been sharing wonderful memories; Samira Asgari, Mahdi Aminian, Somayyeh Rahimian, Farhang Nabei and Marie Shamseddin. My thanks extends to Mahdi Khoramshahi, Mehdi Alem, Ehsan Kazemi, Mokhtar Bozorg, Samira Kouchali, Majid Bastankhah, Arizu Ghiasaleh, Farnaz Eslami, Pedram Pad, Mahsa Shoaran and Saba Saeedi.

I am greatly indebted to my dear parent Amir and Nahid who have been constantly supporting me with their unconditional love. I owe them all the achievements I gained throughout my

Acknowledgements

life. Special thanks to my dear sister Shiva, for her spiritual support and empathy.

Lausanne, 8 February 2016

Abstract

The steady growth of capacity demand in telecommunication networks has sparked the development of various photonic devices for ultrafast optical signal processing functions to meet the requirements of future flexible fiber networks in general and backbone in particular. Although these photonic devices expand the electrical bandwidth operation, they mostly operate at single wavelength and hence remain non-viable solutions for practical implementation in WDM networks that are considered as the major technology for high speed communications.

Another key challenge of future optical networks is the ability to merge channels in time and frequency domain in the most efficient way in order to reach the theoretical Nyquist limit of transmission links. A promising technique is the use of sinc-shaped Nyquist pulses that enable multiplexing channels in time domain with no inter-symbol interference (ISI) while exhibiting a rectangular spectrum that alleviates the need for guard-band. The sinc pulse is indeed the basic building block in most theoretical papers that have estimated overall capacity limits, and intense efforts are being made to generate optical Nyquist pulses beyond the limit of electronics that can directly be used at the physical layer.

Within the above context, two approaches, referred to as optical signal processing of WDM networks and generation/detection of Nyquist superchannels, have been studied in this thesis.

The first addressed problem is simultaneous signal processing of WDM channels. We present two principal blocks required for routing and transporting data in WDM networks, both based on dual-pump fiber optical parametric amplifier (FOPA) with (sinusoidally) modulated pumps. We show that this scheme can be designed to operate simultaneously on WDM channels at any desired wavelength range. The former block enables simultaneous wavelength conversion and time compression which is a necessary functionality in connecting dissimilar rate WDM networks. The latter processing block is all-optical 3R regeneration (reamplification, reshaping, retiming) which is crucial for maintaining pulse quality along long-haul WDM links. We use theoretical analysis supported by experimental results to demonstrate the efficiency of the proposed technique.

The second problem that we investigate is the generation and detection of WDM-Nyquist superchannels. We developed a simple technique based on Mach-Zehnder modulators (MZM)

Abstract

to generate a sinc-shaped Nyquist time window by direct synthesis of a rectangular, phase locked frequency comb. We show the produced pulses have exceptional quality as well as high tunability in terms of pulse width and repetition rate. We also further demonstrate a noncoherent method based on the proposed technique to perform real-time demultiplexing of WDM-Nyquist superchannels, simultaneously in time and frequency. The experimental results that are proved by mathematical analysis are employed to demonstrate the effectiveness of the proposed methods.

Key words: fiber optics, nonlinear fiber optics, optical parametric amplification, sinc-shaped pulse, Nyquist superchannel, optical signal processing.

Résumé

La très forte demande pour plus de capacité dans les réseaux de télécommunications a conduit au développement de nombreux composants photoniques pour le traitement tout optique de l'information capables de répondre aux besoins de flexibilité des futurs réseaux à fibre optique en général et des réseaux dorsaux (les autoroutes de l'information) en particulier. Bien que ces composants permettent de dépasser la bande passante électrique, ils n'opèrent en général qu'à une seule longueur d'onde, ce qui limite fortement leur mise en application comme solution viable dans les réseaux multiplexés en longueur d'onde (WDM) qui constituent l'essentiel des réseaux haut débits déployés.

En outre, la recherche de nouvelles méthodes permettant d'agréger de manière optimale l'information en temps et fréquence et d'atteindre ainsi la limite de Nyquist de capacité fait l'objet d'intenses efforts. Une technique prometteuse consiste à utiliser des impulsions optiques possédant une forme sinus cardinal (impulsions de Nyquist). Ces impulsions permettent non seulement le multiplexage dans le domaine temporel sans interférence inter-symbole, mais aussi dans le domaine fréquentiel : En effet, du fait de l'allure rectangulaire de leur spectre fréquentiel, il n'est pas nécessaire d'utiliser de bande de garde. Les impulsions sinus cardinal sont ainsi utilisées dans toutes les études théoriques se proposant d'évaluer la capacité limite des réseaux à fibre optique. Leur mise en œuvre expérimentale présente un intérêt très important.

Dans ce contexte, cette thèse a pour objet d'apporter une contribution dans le traitement tout optique des signaux WDM d'une part, et la mise en œuvre expérimentale et l'utilisation des impulsions de Nyquist sous la forme de « super-canaux » d'autre part.

La première partie de cette thèse repose sur une méthode pour traiter simultanément les canaux WDM. Cette méthode est basée sur l'amplification paramétrique à fibre optique avec deux pompes modulées en intensité. Dans une première mise en œuvre expérimentale, nous démontrons qu'il est possible de convertir en longueur d'onde et compresser en temps simultanément un nombre arbitraire de canaux WDM. Cette fonctionnalité pourrait s'avérer essentielle pour permettre d'interconnecter des réseaux optiques WDM avec des débits différents. Une seconde mise en œuvre expérimentale de cette méthode nous permet de démontrer la régénération toute optique 3R (ré-amplification, remise en forme, recalage en temps), une

Résumé

fonctionnalité cruciale pour le maintien de la qualité d'impulsion dans les réseaux dorsaux WDM. Ces expériences corroborent une analyse théorique approfondie de cette méthode.

La seconde partie de cette these s'attaque à la generation de super-canaux Nyquist-WDM. Nous avons développé une technique simple basée sur les modulateurs Mach-Zehnder (MZM) pour générer un peigne de fréquence rectangulaire et verrouillé en phase, induisant ainsi dans le domaine temporel des impulsions sinus cardinal. Nous démontrons expérimentalement l'efficacité et la flexibilité de cette méthode pour générer des impulsions d'une qualité exceptionnelle à n'importe quelle longueur d'onde avec un taux de répétition flexible. Nous nous inspirons ensuite de cette même méthode pour démultiplexer de manière transparente des super-canaux Nyquist-WDM simultanément en temps-fréquence.

Mots clefs : fibre optique, effets non linéaires dans les fibres optiques, amplificateurs paramétriques à fibre optiques, impulsions de forme sinc, superchannel de Nyquist, traitement du signal optique

Contents

Acknowledgements	i
Abstract (English/Français)	iii
List of figures	ix
List of tables	xvii
1 Introduction	1
1.1 Thesis Motivation	1
1.2 Problem Description	4
1.2.1 Generating High Quality Optical Nyquist Pulses	4
1.2.2 Uniform Optical Signal Processing of WDM Channels	5
1.2.3 Thesis Aims	6
1.3 Thesis Contribution and Organization	6
2 General Principles	9
2.1 Propagation of Light in Optical Fiber	9
2.1.1 Linear Effects	11
2.1.2 Nonlinear Effects	14
2.1.3 Modeling Light Propagation in Optical Fibers	17
2.2 Optical Parametric Amplifiers	19
2.2.1 Single-Pump Parametric Amplifier	19
2.2.2 Dual-Pump Optical Parametric Amplifier	22
2.3 State of Art in Single-Mode Fibers	25
3 Optical Short Pulse Generation Based on Parametric Amplification	27
3.1 Introduction	27
3.2 Investigation of Pulse Generation in Single-Pump FOPA	28
3.2.1 Theory	29
3.2.2 Experiment	33
3.2.3 Results and Discussions	33
3.3 Investigation of Pulse Generation in Dual-Pump FOPA	38
3.3.1 Theory	39
3.3.2 Experiment	46

Contents

3.3.3	Results and Discussions	47
3.3.4	Dissimilar Pump Modulation	48
3.4	Discussion and Conclusion	51
4	All-Optical Signal Processing for WDM Networks	53
4.1	Introduction	53
4.2	Uniform Wavelength Conversion and Time Compression of WDM Channels . .	54
4.2.1	Theory	54
4.2.2	Experiment	58
4.2.3	Results and Discussions	59
4.3	3R Signal Regeneration	61
4.3.1	Results and Discussions	66
4.3.2	Crosstalk Effects	72
4.4	Discussion and Conclusion	74
5	Generation of Nyquist Pulses and Detection of WDM-Nyquist Superchannels	77
5.1	Introduction	77
5.2	All-Optical Nyquist Pulse Generation by Parametric Amplification	78
5.2.1	Theory	79
5.2.2	Experiment	82
5.2.3	Results and Discussions	83
5.3	All-Optical Nyquist Pulse Generation by Intensity Modulator	85
5.3.1	Theory	85
5.3.2	Experiment	87
5.3.3	Results and Discussions	88
5.4	All-optical Detection of WDM-Nyquist Superchannels	95
5.4.1	Principle of Operation	96
5.4.2	Experiment	97
5.4.3	Results and Discussions	98
5.5	Discussion and Conclusion	100
6	Conclusion and Perspective	103
6.1	Summary and Conclusion	103
6.2	Future Works	105
A	Appendix	107
A.1	Gain Sensitivity	107
A.2	Pulse Shape	108
	Bibliography	118
	Curriculum Vitae	119

List of Figures

2.1	(a) Cross section of a conventional optical fiber. The structure shows core, cladding and buffer layers. (b) Principle of light propagation in fiber optic based on successive total internal reflection. Fields that enter the core at incident angle less than θ_{MAX} keep propagating inside the fiber.	10
2.2	Attenuation profile (solid line) of SMF-28 versus wavelength. Dashed line represents the theoretical limit which originates from Rayleigh scattering and silica intrinsic molecular absorption.	12
2.3	Dispersion profile of silica, D_m (dashed line) and standard SMF, D_{total} (solid line) with ZDW around 1300 nm. The difference is due to the waveguide dispersion effect, D_W	13
2.4	Typical gain spectrum of single-pump FOPA. In the region close to the pump ($\Delta\beta_L \approx 0$) the gain is parabolic while for perfect phase-matching condition ($\kappa = 0$) the gain would be exponential.	22
2.5	Spectral model of four-wave interaction in dual-pump FOPA. ω_C is the central frequency of the two pumps. $\Delta\omega_S$ and $\Delta\omega_P$ are respectively signal and pump frequency difference with respect to ω_C	23
2.6	Dual-pump FOPA gain spectrum for (a) high fluctuation and (b) low fluctuation. Dashed line depicts the four-wave interaction model while solid line represents the result of six-wave interaction model.	25
3.1	Gain sensitivity as a function of normalized phase-mismatch, $\Delta\beta_L/\gamma P_0$. The inset illustrates gain spectrum for a typical HNLF with dispersion parameters $\beta_2 = 2.9 \times 10^{-29} \text{s}^2 \text{m}^{-1}$ and $\beta_4 = -6.4 \times 10^{-55} \text{s}^4 \text{m}^{-1}$. Maximum sensitivity is reached at $\Delta\beta_L/\gamma P_0 = -4$ phase-matching condition.	29
3.2	Experimental setup for pulse generation in single-pump FOPA. PC: polarization controller; IM: intensity modulator; PM: phase modulator; BPF: bandpass filter; WDM: wavelength division multiplexer; HNLF: highly nonlinear fiber; OSA: optical spectrum analyzer.	33
3.3	Optical spectra at the HNLF output for pump ON and OFF with signal seed position at $\lambda_S = 1566.6 \text{ nm}$ ($\Delta\beta_L = -2\gamma P_0$) and $\lambda_S = 1570.3 \text{ nm}$ ($\Delta\beta_L = -4\gamma P_0$).	34

List of Figures

3.4	For a pump at $\lambda_P = 1557$ nm, (a) idler waveform and (b) spectrum for the signal at $\lambda_S = 1566.6$ nm; (c) Experiment, simulation and theoretical fit for the signal at $\lambda_S = 1566.6$ nm corresponding to $\Delta\beta_L = -2.2\gamma P_0$; (d) idler waveform, (e) spectrum for the signal at $\lambda_S = 1570.3$ nm; (f) Experiment, simulation and theoretical fit for signal at $\lambda_S = 1570.3$ nm corresponding to $\Delta\beta_L = -3.97\gamma P_0$; (g) idler waveform, (h) spectrum for the signal at $\lambda_S = 1570.5$ nm (i) Experiment, simulation and theoretical fit for signal at $\lambda_S = 1570.5$ nm corresponding to $\Delta\beta_L = -4.11\gamma P_0$	35
3.5	Evolution of idler pulse shape as a function of signal wavelength for (a) 0 dBm signal power and (c) 6 dBm signal power. (b) Experimental full width half maximum (FWHM) of generated idler pulse as a function of signal wavelength for 0 dBm, 3 dBm and 6 dBm of signal power (d) Comparison of the experimental, simulated and theoretical FWHM of generated idler for 0 dBm signal power. . .	36
3.6	Idler pulse shapes for (a)-(c) $\Delta\beta_L = -2\gamma P_0$, (d)-(f) $\Delta\beta_L = -3\gamma P_0$ and (g)-(i) $\Delta\beta_L = -4\gamma P_0$ at three different signal power level.	37
3.7	Idler waveform at near-sinc position for repetition rate (a) 2.75 GHz, (b) 5.5 GHz and (c) 11 GHz. (d) Comparing idler pulse shapes for $\Delta\beta_L = -4\gamma P_0$ with pump position at $\lambda_P = 1552$ nm (dashed line), $\lambda_P = 1556$ nm (solid line) and theoretical fit from Eq. 3.12 for pump position at (e) $\lambda_P = 1552$ nm and (f) $\lambda_P = 1556$ nm at 40 GHz repetition rate.	38
3.8	(a) Gain sensitivity as a function of normalized phase-mismatch, $\Delta\beta_L/\gamma P_0$ for different total pump power and HNLF length. (b) Gain sensitivity as a function of pumps power ratio $\alpha = P_1/P_2 $ for different normalized phase-mismatch terms.	40
3.9	(a) Idler duty cycle (DC) defined as $DC = T_{FWHM} \times f_R$ versus normalized phase-mismatch $\Delta\beta_L/\gamma P_0$, obtained by numerical solution (solid line) and empirical equation in Eq. 3.24 (dashed line) (b) FOPA gain as a function of normalized phase-mismatch, $\Delta\beta_L/\gamma P_0$ for $P_0 = 0.5$ W and $L = 350$ m. The inset shows the inverse relation between DC and $S_{P_0}^{G_{dB}}$	42
3.10	(a) Idler pulse shape over one period as a function of $\Delta\beta_L/\gamma P_0$, (b) Normalized intensity of idler pulses over one period for different values of normalized phase-mismatch, $\Delta\beta_L/\gamma P_0$	43
3.11	Principle of pulse generation in dual-pump FOPA. As $\Delta\beta_L/\gamma P_0$ is bounded to m with a ripple ρ , the DC of generated pulses follow the same trend in frequency. Dual-pump FOPA gain spectra for (b) two synchronous modulated pumps, (c) one modulated and one CW pump. The peak power of each pump is $P_0/2 = 0.25$ W.	45
3.12	Experimental setup for pulse generation in dual-pump FOPA. TL: tunable laser; IM: intensity modulator; PM: phase modulator; PC: polarization controller; TBF: tunable bandpass filter; WDM: wavelength division multiplexer; OSA: optical spectrum analyzer.	46

3.13 Gain spectra and pulse width behavior in dual-pump FOPA for parameters in case 1 and case 2, denoted in Table 3.2. (a) and (c) experimental (dot) and theoretical gain spectrum obtained from TS (dashed line) and FS (solid line) interaction model along with normalized phase-mismatch for case 1 and 2 respectively. (b) and (d): experimental (dot) <i>DC</i> values as well as theoretical results derived from TS (dashed line) and FS (solid line) interaction model for case 1 and 2, respectively.	47
3.14 (a) and (b) depict the evolution of averaged pulse shape with idler wavelength respectively regarding the first and the second phase-matching condition described in Table 3.2. (c) actual (act) and averaged (avg) pulse shape for $\Delta\beta_L/\gamma P_0=0.9$ in the first case and for $\Delta\beta_L/\gamma P_0 = -0.28$ in the second case.	48
3.15 Simulated pulse train of slow modulated pump (solid line), fast modulated pump (dashed line) and idler (dotted line) for (a) $(f_1, f_2) = (10 \text{ GHz}, 10 \text{ GHz})$, (b) $(f_1, f_2) = (5 \text{ GHz}, 10 \text{ GHz})$, $(f_1, f_2) = (2.5 \text{ GHz}, 10 \text{ GHz})$. Experimental idler pulses for $(f_1, f_2) = (5 \text{ GHz}, 10 \text{ GHz})$ and $(f_1, f_2) = (2.5 \text{ GHz}, 10 \text{ GHz})$	50
3.16 (a) Generated idlers for $(f_1, f_2) = (1 \text{ GHz}, 10 \text{ GHz})$ at $\Delta\beta_L/\gamma P_0 = -1$ (solid line) and $\Delta\beta_L/\gamma P_0 = -3$ (dashed line) phase-matching condition. (b) Generated idler for $(f_1, f_2) = (1 \text{ GHz}, 10 \text{ GHz})$ and $\Delta\beta_L/\gamma P_0 = -1$ condition with normal pump modulation (solid line) and modified pump modulation (dashed line).	51
4.1 Simulation: (a) <i>CF</i> at $\kappa = 0$ and $\kappa = -\gamma P_0$, (b) <i>CF</i> as a function of κ for $\gamma P_0 L = 2$ and $\gamma P_0 L = 8$, (c) $1/e$ pulse width after chirp compensation, (d) Time-bandwidth (TB) product before and after chirp compensation for $\kappa = 0$	56
4.2 (a) Experimental idler pulse shape at Gaussian condition before and after chirp compensation, (b) Calculated idler spectral envelop for chirped (solid line) and chirp-free (dashed line) pulses. The chirp-free idler is obtained by proper pre-chirping of the signal.	57
4.3 Experimental setup for simultaneous wavelength conversion and time compression of WDM channels. TL: tunable laser; IM: intensity modulator; TBF: tunable bandpass filter; WDM: wavelength division multiplexer; OSA: optical spectrum analyzer; WSS: wavelength selective switch; BRM: bit rate multiplier.	58
4.4 (a) Experimental (dot) and theoretical (line) FOPA gain spectrum along with normalized phase-mismatch term $\Delta\beta_L/\gamma P_0$ (b) Experimental (dot) and theoretical (line) idler FWHM along with pulse SNR. (c)-(f) Experimental pulse shape (black) with theoretical Gaussian expression (red).	59
4.5 (a) Pulse shape before and after chirp compensation with normal sinusoidal pump modulation, (b) Pulse shape before and after chirp compensation with equalized sideband pump modulation. The experimental data are fit with simulation results from SSF. The pump shape is shown in the inset for each plot. . .	60

List of Figures

4.6	(a) 10 Gb/s RZ trace of single wavelength signal after compression, (b) $\times 4$ multiplexed train of 10 Gb/s RZ pulses, (c) FOPA gain spectrum with modulated WDM band as input signal, (d) Magnified idler spectrum from the FOPA output spectrum.	61
4.7	(a)-(d) Eye-diagrams of frequency demultiplexed 40 Gb/s idler channels. The multiplexed channel is obtained by passing the compressed pulses through a bit rate multiplier (BRM).	62
4.8	(a) Typical experimental optical spectrum of dual-pump FOPA. FWM between two sinusoidal modulated pumps and the NRZ input signal, generates RZ idler data. (b) Illustration of a typical FOPA transfer function (TF). The saturation regime squeezes amplitude fluctuations and improves the pulse Q-factor. . . .	64
4.9	Experimental setup for regeneration of WDM channels. TL: tunable laser; IM: intensity modulator; PM: phase modulator; PC: polarization controller; TBF: tunable bandpass filter; WDM: wavelength division multiplexer; Atn: attenuator; OSA: optical spectrum analyzer; BERT: bit-error rate tester.	65
4.10	(left axis) Experimental (red dot) and theoretical (black line) gain spectrum of dual-pump FOPA. (right axis) Theoretical normalized phase-mismatch term. Blue and red shaded wavelength spans represent signal and idler wavelength ranges, respectively.	66
4.11	Experimental (dot) and theoretical (line) transfer function (TF) of dual-pump FOPA when one, three, and five WDM channels present as the input signal. . . .	67
4.12	BER measurement of single wavelength channel; back-to-back before regeneration stage (red triangle), back-to-back after regeneration stage (black cross), degraded (green square) and regenerated (blue circle) for three OSNR levels at (a) 28 dB, (b) 23 dB and (c) 19 dB.	68
4.13	Optical (left column) and electrical (right column) eye-diagrams of (a),(b) back-to-back channel, (c),(d) degraded channel with OSNR 23 dB and (e),(f) regenerated channel.	69
4.14	Receiver sensitivity gain of individual channel after regeneration at BER level of 10^{-9} . The OSNR of each channel is degraded to 23 dB to check the regenerator performance.	70
4.15	(a) BER of the regenerated middle channel (in presence of other channels) at different values of input power when the OSNR is degraded to 23 dB. (b)-(e) Optical eye-diagram of regenerated middle channel with signal levels at 2 mW, 8 mW and 20 mW.	71
4.16	(a) Normalized idler spectrum of three signal power levels. The middle channel is turned off to show the amount of spurious FWM. (b) Optical spectrum of dual-pump FOPA with five WDM channels as the input signal.	72
4.17	Receiver sensitivity gain of each channel (in presence of other channels) at 10^{-9} BER level when the OSNR is degraded to 23 dB.	73

4.18 BER versus time detuning of the regeneration time window. Three cases are considered; single (blue circle) and multi-channel (red square) operation with OSNR level better than 35 dB and multi-channel (green triangle) operation with 23 dB OSNR level.	73
5.1 Principle of generating near-sinc Nyquist pulses with single-pump FOPA and a subsequent phase modulator for chirp compensation. WDMux: wavelength division multiplexer.	79
5.2 (a) Sinusoidal pump (solid line) and parabolic pump (dashed line), (b) Generated idler by sinusoidal pump (solid line), by a parabolic pump (dashed line) and sinc-shaped pulse (dotted line). (c) Maximum amplitude of idler at Nyquist pulse zeros. T_B corresponds to one bit duration ($T_B = 1/f_R$).	80
5.3 Optical spectrum of the generated idler at $\gamma P_0 L = 4$ by (a) sinusoidal pump, (b) parabolic pump (c) sinc pulse.	81
5.4 Experimental setup for chirp compensation of near-sinc pulses. PC: polarization controller; EDFA: Erbium doped fiber amplifier; BPF: bandpass filter; PM: phase modulator; IM: intensity modulator; OSA: optical spectrum analyzer.	82
5.5 Idler spectrum (a) before chirp compensation, (b) after chirp compensation, (c) before chirp compensation (dB scale), (d) after chirp compensation (dB scale). Idler pulse trace (e) before chirp compensation and (f) after chirp compensation.	83
5.6 Idler spectrum (a) before chirp compensation, (c) after chirp compensation. Idler pulse trace (b) before chirp compensation, (d) after chirp compensation. In all figures we have $\gamma P_0 L = 3$	84
5.7 Time (left) and frequency (right) representation of a single sinc pulse (top) and a sinc-pulse sequence (bottom). The Fourier representation of an unlimited sinc-pulse sequence is a rectangle while the spectrum of an unlimited sinc-pulse train is a frequency comb with uniform phase and an rectangular envelop.	85
5.8 Experimental setup for generating sinc-shaped Nyquist pulses. ECL: external cavity laser; MZM: Mach-Zehnder modulator.	87
5.9 Tunability of sinc-shaped Nyquist pulses from 9 spectral lines. The experimental results (black solid line) are compared with theoretical waveform (red dashed line) over 4 frequency decades. (a) $f_1 = 30$ MHz and $f_2 = \Delta f = 10$ MHz, (b) $f_1 = 300$ MHz and $f_2 = \Delta f = 100$ MHz, (c) $f_1 = 3$ GHz and $f_2 = \Delta f = 1$ GHz and (d) $f_1 = 30$ GHz and $f_2 = \Delta f = 10$ GHz.	88
5.10 Frequency and time domain representation of the generated sinc-shaped Nyquist pulses. Left column shows the measured spectrum and right column represents time domain waveform for (a),(b) $N = 9$ spectral components separated by $\Delta f = 10$ GHz, expanding over 90 GHz bandwidth, (c),(d) $N = 10$, $\Delta f = 10$ GHz and bandwidth of 100 GHz, (e),(f) $N = 15$, $\Delta f = 6$ GHz, and bandwidth of 90 GHz.	89

List of Figures

5.11 Measured stability and quality of periodic sinc pulses. (a) Color grade of one measured sinc-pulsed sequence corresponding to the case depicted in Figs. 5.10(a) and (b). Measurements indicate a SNR > 40 dB and a timing jitter of 82 fs. (b) RMS error between the measured pulses and the theoretical sinc pulse intensity, derived from Eq. 5.7 as a function of the roll-off factor, β . The RMS error is minimized for $\beta = 0$	90
5.12 Spectrum of modulated sinc pulses. Measured spectra of modulated sinc pulses (black solid line) with (a) OOK and (b) BPSK modulation format. The simulated results (red dashed line) are obtained by including OSA finite spectral bandwidth (0.01 nm).	91
5.13 Eye-diagram of intensity modulated sinc pulse, (a) initial pulse train, (b) two times multiplexed pulse train, (c) four times multiplexed pulse train.	92
5.14 Sinc-shaped Nyquist pulse generation using a nonlinear stage between two intensity modulators. TLS: tunable laser source; IM: intensity modulator; PC: polarization controller; BPF: bandpass filter; WSS: wavelength selective switch.	92
5.15 Measured spectra after the (a) 1st stage, (b) HNLFs at the 2nd stage for generating sinc-shaped Nyquist pulse train at 30 GHz repetition rate.	94
5.16 Sinc-shaped Nyquist pulse train at 30 GHz repetition rate (with $N = 1$). (a) Measured spectrum from a bandwidth of 270 GHz. (b) The corresponding temporal profile.	95
5.17 Sinc-shaped Nyquist pulse train at 25 GHz repetition rate (with $N = 5$) (a) Measured spectrum of the 255 GHz rectangular frequency comb, (b) the corresponding temporal profile.	95
5.18 Principle of demultiplexing WDM-Nyquist superchannels. The incoming sequence undergoes an inner product with Nyquist carver. A bandpass filter then integrates the product and selects the WDM channels. The ISI collected from adjacent channels in this technique is ideally zero.	97
5.19 Experimental setup for real-time demultiplexing of WDM-Nyquist superchannels. TLS: tunable laser source; WDM: wavelength division multiplexer, IM: intensity modulator; PC: polarization controller; BRM: bit rate multiplier; VODL: variable optical delay line; BPF: bandpass filter, Atn: attenuator; BERT: bit-error rate tester.	98
5.20 Spectral and temporal representation of WDM-Nyquist superchannel. (a) Eye-diagram of O-TDM tributaries for a single wavelength. (b) Optical spectrum of three guard-band free WDM-Nyquist channels.	99
5.21 Experimental BER of demultiplexed tributaries of a WDM-Nyquist superchannel for (a) single wavelength (b) middle wavelength of three WDM-Nyquist superchannels.	99
5.22 Simulation and experimental eye-diagrams of demultiplexed tributaries for 8 O-TDM, 3 WDM Nyquist superchannels (a,b) single wavelength, (b,e) middle wavelength in 3 WDM channel scheme, (c,f) edge channel in 3 WDM channels scheme.	100

5.23 Simulated optical demultiplexed eye-diagrams of a tributary in a WDM-Nyquist superchannel with 8 orthogonal TDM tributary and 3 WDM channels for (a) Gaussian filter, bit non-assigned, (b) Nyquist filter, bit non-assigned, (c) Nyquist filter, bit assigned, (d) Nyquist filter, bit assigned including rise/fall time a tributary at the edge of bit slot. 101

List of Tables

2.1	Comparing the characteristics of SMF, DSE, HNLF and PCF fiber type.	25
3.1	SNR (dB) of generated pulses corresponding to Fig. 3.6	36
3.2	FOPA settings and parameters for the two experimental cases presented in Fig. 3.13. The normalized phase-mismatch term experiences high fluctuations in case 1 and low fluctuation in case 2.	46
4.1	RMS jitter of the optical eye-diagram before and after regeneration for three OSNR levels.	68

1 Introduction

1.1 Thesis Motivation

Driven by multimedia applications, cloud computing, mobile networking and other emerging technologies, worldwide data traffic is growing at an annual rate estimated to exceed 40%, corresponding to about a 30-fold increase per decade [1]. This immense growth rate concerns all network segments ranging from mobile wireless and fixed access to supercomputers, data center interconnections and long-haul transport. Therefore, a worldwide community of researcher and engineers are seeking an advanced solution for network infrastructure to carry the required data more efficiently than ever before [2].

When talking about increasing or optimizing network capacity, we consider five physical dimensions which can be exploited to convey optical data; time, frequency, quadrature, polarization and space [3]. For decades, these dimensions have been employed to significantly increase the bit rate of communication systems. The time domain is basically used to send the information symbols in a temporal succession in a similar manner as the words are made by concatenating letters. Pulse shaping can be employed to compress the data spectrum and multi-level modulation may be used to transfer more information per symbol in this system. In case the data are modulated on a carrier frequency much higher than the symbol rate, both sine and cosine components of the carrier, termed two quadrature dimensions, can be used. This leads to a two-dimensional symbol which can increase the rate of information transfer.

Frequency is another dimension which lets multiple communication signals be transmitted on distinct carrier frequencies over the same transmission medium. In optical communication this method is known as wavelength division multiplexing (WDM). The scalability of such systems is essentially limited by the inherent bandwidth constraints of the shared medium as well as some engineering limitation. In some techniques, such as the one based on coherent detection, the polarization dimension can be also employed to enable parallel information streams over two orthogonal polarizations. Eventually, there is the possibility of space multiplexing which can be exploited in various ways.

Although all the mentioned multiplexing techniques can be used separately or collectively to increase information transfer rate, the preference and order of each technique is highly dependent on the desired application and the corresponding physical and economical constraints. In general, it is preferable to perform modulation in time domain as fast and economical as possible before using other dimensions. However, with current technology the commercial communication systems can only afford modulation speeds in the range 10-50 Gbaud (symbol per second). Therefore, to achieve higher speeds, other dimensions need to be used. If parallel optical fibers can be employed, spatial multiplexing is an interesting solution. This solution is often used for rack-to-rack interconnects that are no more than few tens of meters. For longer distance connections over single transmission fiber, it is more efficient to rely on frequency dimension by WDM systems. However, the bandwidth over which WDM signals can be transmitted is limited to the low transmission-loss window of standard fiber (1260 nm to 1525 nm, corresponding to 50 THz). Nevertheless, for long-haul transmission where optical amplifiers are required, the amplification bandwidth is another issue (typically 5 THz for C-band amplifier). With these limitations on total transmission bandwidth it is desirable to squeeze as much information as possible into a fixed bandwidth in order to increase network capacity. This signifies the concept of *spectral efficiency* as an important system parameter. To keep pace with the growing data rate, new techniques need to be developed to improve the spectral efficiency of optical channels. Employing polarization multiplexing, multi-level signaling and quadrature modulation are a few approaches that increase the spectral efficiency of a single channel [4, 5]. However, implementing such schemes requires digital coherent detection which substantially increases the systems complexity.

Another approach to enhance the speed of optical links is to combine several low rate but high spectral efficiency channels to form *superchannels* that can be routed and treated as a single entity in the network. Such aggregation can be performed either in time or frequency domain [6, 7]. In orthogonal frequency-division multiplexing (OFDM) several subcarriers are put together to generate the superchannel. Each subcarrier has sinc-shaped spectrum and can therefore be spaced at the baud rate without any inter-channel crosstalk. Equivalently, Nyquist superchannels that are formed in time domain consist of several Nyquist channels. These channels can be multiplexed in time with overlap, without any inter-symbol interference (ISI) [8]. Moreover, as these pulses own a steep spectral profile, they have an inherent high spectral efficiency and can be efficiently multiplexed in frequency to produce WDM-Nyquist superchannels [9]. These properties of Nyquist pulses make them very attractive for communication systems as data transmission rates can be maximized while the bandwidth usage is minimized.

On the other hand, once data channels are generated, routing through long-haul optical networks give rise to other challenges. Especially in WDM technology the problem arises when two channels at similar wavelengths arrive at a node and need to be routed to a single output fiber [10]. To address this conflict, *wavelength conversion* (WC) was proposed to produce a copy of one of the two signals (at λ_S) to a free wavelength (at λ_C) [11]. Although it would seem that a routing node requires many WCs to deal with various scenarios, it is shown in

practice that a much lower number of WCs than the number of incoming wavelengths into a node is sufficient to reduce the blocking probability and allow for efficient wavelength reuse [12]. WC techniques were initially proposed for wavelength-switched networks, which implement circuit switching. However, this concept was later proposed for optical packet switching networks with large switches where various WCs are used to dynamically assign the output wavelength based on the packet header information. All WCs are accompanied by an arrayed waveguide grating (AWG); such that each wavelength-converted packet is routed by the AWG, based on the corresponding wavelength. Recently, the WC problem has become more challenging as the diversity of the interconnected networks has increased in terms of operational speed and modulation format.

The other limiting factor regarding long-haul transport networks is the propagation defects which have their origin in accumulated noise from amplifiers, fiber dispersion, fiber nonlinearities and inter-channel crosstalk. The primary physical mechanism for amplitude noise is the beating between signal and amplified spontaneous emission (ASE) and the interaction among channels. The dispersion and nonlinear effects can also modify the pulse shape in a way that the contrast between '0' and '1' is reduced, which increases the error in resolving the data. The other type of quality degradation arises from the random deviations of the pulse position, a phenomenon known as *timing jitter*. A possible solution to overcome these system limitations is to implement *signal regeneration*. In this solution the link is divided into several independent trunks where the impairments are treated at the end of each trunk by regenerating the data. The basic functions to implement regeneration are *reamplification*, *reshaping* and *retiming*. Reamplification alone provides the "1R" functionality. In the absence of retiming, the regenerator is a "2R" device which only performs reamplification and reshaping. A full "3R" device includes retiming function as well, which necessitates the use of an external clock source that is locked on the incoming sequence.

Traditionally, WC and 3R regeneration require optical-electrical-optical (OEO) conversion where the incoming optical signal is converted to an electrical signal and the WC and 3R functions are realized in electrical domain using digital signal processing (DSP). Taking advantage of mature DSP technology, operating in digital domain provides an extensive flexibility in implementing required functionalities. Moreover, digital domain has the advantage of using forward error correction (FEC) coding to recover the corrupted data. Commercial products for OEO-based WC and 3R are presently available for basic communication systems. However, a major bottleneck of OEO systems is their growing complexity at high symbol rates (i.e. beyond 40 Gbaud). Furthermore, with emerging modulation techniques and multiplexing methods, OEO systems face a severe difficulty. The problem is that apart from limited speed of electronics, the complexity of OEO systems increases at least linearly with the number of channels or the order of modulation format. Therefore, research efforts have been conducted to implement all-optical WC (AOWC) [13, 14] and all-optical 3R (AO-3R) regeneration [15–17] for more than 20 years.

Numerous demonstrations and solutions have been proposed for all-optical 3R and WC, while

various nonlinear processes have been investigated to provide a more effective and robust functionality. From system level point of view, these methods can be characterized based on different parameters among which the most important ones are:

- *Tuning range* : the operating wavelength range of the device. For AOWC it indicates the range over which the converted wavelength λ_C is generated. In AO-3R it defines the input range in which the input signal is regenerated.
- *Polarization independence* : the device's sensitivity to the polarization state of the input. In general, polarization independent devices are more desirable as they do not need additional provisioning.
- *Format transparency* : the ability of the device to operate at different modulation formats. With the emerging modulation techniques it is important that both intensity modulated (IM) and phase modulated (PM) signals can be supported.
- *Operating speed* : the maximum speed at which the device can process data. This parameter is limited by the time constant of the physical phenomena behind the system.

1.2 Problem Description

Current high speed optical networks are designed based on WDM technology to increase the carrier capacity of optical fibers. This technology would also represent the building blocks of future *flexi-grid* networks where the concept of dynamic frequency spacing of the carriers is introduced. To keep pace with the growing data rate, new techniques need to be developed to increase the spectral efficiency of WDM channels and to facilitate their routing and transporting through optical networks.

To this end, we spot and address two major problem regarding the pulse shaping and transporting WDM channels as fallows:

1.2.1 Generating High Quality Optical Nyquist Pulses

Nyquist pulses were initially generated by using electrical arbitrary waveform generators where an offline programmed Nyquist filter is used to shape the baseband signal. An intensity modulator is thereupon employed to modulate an optical carrier with the electrical signal. One parameter to measure the quality of Nyquist pulses is the *roll-off* factor, β that varies between 0 and 1. A roll-off factor close to 0 is attributed to higher quality pulses as the corresponding optical spectrum becomes steeper and therefore provides better spectral efficiency.

The pulses that are generated by electrical Nyquist filter exhibit $\beta = 0.0024$ indicating high quality pulses [18]. However, by increasing the symbol rate to 40 Gbaud and beyond, the limited speed of electronics degrades the quality of the pulses. Indeed, the quality of Nyquist

pulses is highly dependent on the resolution of digital to analog converters [7] which is restricted to the limited sampling rate and processor capacities. As a result, extensive studies have been done to generate Nyquist pulses in optical domain exploiting various optical pulse shaping and spectral filtering techniques. Yet, despite of the complexity of proposed schemes the generated optical Nyquist pulses by prior works do not reach a roll-off factor better than $\beta = 0.5$ [19–21].

On the other hand, demultiplexing of Nyquist superchannels at high symbol rates suffers from similar set of issues as Nyquist pulse generation. For real-time demultiplexing of such superchannels very high speed analog to digital converters are required to sample the incoming sequence while avoiding ISI from neighbor channels. This approach is yet limited to the speed of electronics at the receiver side. Efforts have been made to implement the required sampler in optical domain by sampling the data channels at the exact channel pulse time location using ultra short optical pulses [22, 23]. However, in practice these techniques have low energy efficiency and require extensive electrical and optical apparatus for generating ultra short pulses.

1.2.2 Uniform Optical Signal Processing of WDM Channels

Apart from pulse shape and modulation format, another critical issue regarding WDM channels is the routing problem in optical transport networks. Such routing would certainly require signal processing blocks. Though these blocks can be realized with the aid of OEO conversion and DSP technology, this approach cannot be easily extended to WDM systems. The problem is that the complexity of these blocks increases at least linearly by incrementing the number of input wavelengths or the order of modulation format. Therefore, with the advances in WDM technology and the flexibility of channel spacing in flexi-grid networks, routing nodes should be equipped with extensive electrical and optical devices to deal with various scenarios.

Another approach is to use optical signal processing techniques. Depending on the underlying physical process, these techniques can be functional over a specific bandwidth range and therefore capable of parallel processing of WDM channels. A major difficulty in this approach is to confront the detrimental crosstalk effects among the channels. The corresponding efforts are mostly focused on converting the initial wavelength-multiplexed signal into time or space-multiplexed signals, perform the required processing and then convert the signals back to the wavelength multiplexing scheme. This approach works quite well for small number of channels (up to four channels) but in practice as the channel count increases or the modulation format is modified, the solution fails to be scalable.

WC and 3R regeneration are the two most fundamental processing blocks in routing WDM channels. While the former block provides efficient use of bandwidth resources, the latter one guarantees acceptable quality of optical signals through the links. For WC an additional problem is when two networks with dissimilar speeds are connected. In this case, besides wavelength conversion, time compression of WDM channels is required to adapt the pulse

width of lower speed network to the higher speed one. Obviously, a desirable processing block should provide a uniform response for a specific wavelength range and also be able to provide simultaneous operation for several channels.

1.2.3 Thesis Aims

The first part of this thesis is aimed to introduce a novel all-optical signal processing device which can process WDM channels in parallel. We are interested in a device that is operational over a wide bandwidth range and its complexity remains fixed as the number of input channels increases. Specifically, we aim to implement the two principle signal processing blocks in WDM networks i.e. simultaneous AOWC and time compression for connecting dissimilar rate networks and also AO-3R to retrieve the quality of optical channels. Implementing such a device significantly enhances WDM networks by providing scalable optical signal processing blocks that are of particular interest.

In the second part of the thesis we aim to develop methods for generating a sequence of very high quality optical Nyquist pulses with an almost ideal rectangular spectrum ($\beta \approx 0$). Realizing these pulses in a way that is easily integrable in communication systems, potentially offers a substantial increase in data transmission rates. Additionally, we aim for a non-coherent method to demultiplex WDM Nyquist superchannels. Implementing a simple all-optical real-time demultiplexing method, will further elevate Nyquist superchannels toward practical commercial systems.

1.3 Thesis Contribution and Organization

In the first part of the thesis we introduce for the first time dual-pump fiber optical parametric amplifier (FOPA) with sinusoidal modulated pumps as a signal processing device. We present theoretical models and experimental results to obtain the operating condition of this device to provide a uniform adjustable time window over a wide bandwidth. We will later show that the time window enables successful AOWC and AO-3R of WDM channels. The results show that taking advantage of the introduced device we can perform simultaneous signal processing on several WDM channels without any need to increase the system complexity as the number of channels increases.

In the second part of the thesis we study generation of Nyquist pulses in optical domain. We present a method based on specific FOPA operating condition and one on direct synthesization of a flat phase-locked frequency comb using Mach-Zehnder modulators (MZM). The latter method leads to high quality Nyquist pulses with high flexibility in terms of pulse width and pulse repetition rate. We also propose a novel scheme for real-time demultiplexing of the WDM-Nyquist superchannels in optical domain. This technique is based on the inner product of the incoming sequence with a matched filter. The experimental results successfully verify that our simple scheme is capable to optically generate and demultiplex WDM-Nyquist

superchannels.

The thesis dissertation is organized as following:

- **chapter 2** In this chapter we review the most influential linear and nonlinear processes regarding light propagation through optical fibers. Some of these processes enable a desired functionality and some may inevitably limit the system performance. We also introduce the basics of single and dual-pump FOPAs which will be further discussed in chapter 3.
- **chapter 3** In this chapter we study FOPA in sinusoidal modulated pump regime for single and dual-pump schemes. We show modulated pumps create a time window which shape depends on the system parameters. For dual-pump FOPA we present design rules to enable generating a time window which is uniform over a large wavelength range. This time window would be the key enabling feature for signal processing of WDM channels, which is covered in chapter 4.
- **chapter 4** This chapter presents the application of the optical signal processing device introduced in chapter 3 for WDM networks. We show simultaneous AOWC and time compression as well as AO-3R that are the two important signal processing blocks for routing WDM channels. In both applications the device is shown to be operational for parallel WDM channels.
- **chapter 5** In this chapter we study the generation of optical Nyquist pulses. We start with a method based on single-pump FOPA and later we present a novel technique to generate high quality Nyquist pulses using MZMs. We expand the latter scheme by showing its flexibility in terms of tuning the pulse width and repetition rate. We will also propose a novel real-time demultiplexing technique for WDM-Nyquist superchannels which is based on implementing a matched-filter receiver.
- **chapter 6** This chapter concludes the studies that are presented in this dissertations. Furthermore, we will suggest new directions and potential topics for future research.

2 General Principles

In this chapter we review the most influential effects of light propagation in optical fibers. These effects can be linear, such as absorption and dispersion, or nonlinear like Brillouin, Raman and Kerr effect. Later, we visit the nonlinear Schrödinger equation as a mathematical tool to model the light propagation and review a numerical method to solve it. We study the basics of fiber optical parametric amplifiers afterwards, by inspecting the solutions of underlying coupled-wave equations in single and dual-pump schemes. Finally, we will briefly point out some properties of the fibers that are frequently used in fiber optics experiments.

2.1 Propagation of Light in Optical Fiber

Introduced by quantum mechanics, light is known as a flow of massless particles named *photons*. However, from a macroscopic point of view the photon flux can be assumed as an electromagnetic radiation comprising coupled electric and magnetic fields. In an optical fiber, we can assume the electric field component propagating along the z axis with the following expression :

$$\vec{E}(x, y, z, t) = F(x, y)A(z)e^{-i(\omega_0 t - \beta(\omega_0)z)} \vec{u} \quad (2.1)$$

where $F(x, y)$ is the transverse distribution of the field mode, $A(z)$ is the field slowly varying envelop (SVE), ω_0 is the angular frequency of the carrier, $\beta(\omega_0)$ is the propagation constant and \vec{u} represents the field polarization. In the following sections we assume that $F(x, y)$ is constant along the fiber length and $A(z)$ is a function of light propagation axis.

From the 19th century, guiding the light through a medium was known to be feasible by *total reflection* property. This property occurs when a propagating wave strikes the medium boundary at an angle larger than a particular *critical angle* given that the refractive index is lower on the other side of the boundary. Yet, for many years the existing guiding mediums suffered from substantial propagation losses and therefore were unsuitable for communication applications. In the early 20th century with the invention of optical fibers out of silica (SiO_2)

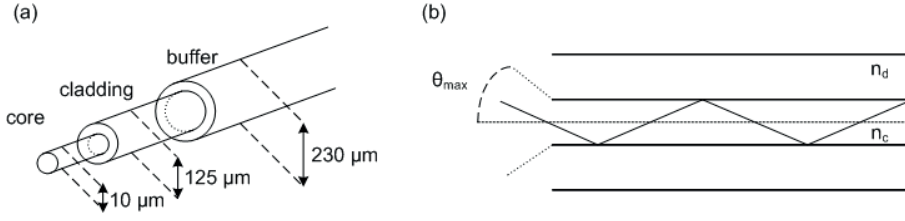


Figure 2.1 – (a) Cross section of a conventional optical fiber. The structure shows core, cladding and buffer layers. (b) Principle of light propagation in fiber optic based on successive total internal reflection. Fields that enter the core at incident angle less than θ_{MAX} keep propagating inside the fiber.

with an extremely low propagation loss, fiber optic communication experienced a rapid growth. A typical silica fiber has a cylindrical core and cladding as shown in Fig. 2.1(a) where the cladding refractive index is slightly lower than the core. Such a design solely allows propagation of transverse modes.

In a simplified model, the fiber holds a step index profile i.e. the core and cladding have constant refractive index, respectively denoted by n_c and n_d ($n_d < n_c$). The lower refractive index of the cladding is generally obtained by doping germanium oxide into silica. As illustrated in Fig. 2.1(b), the principle of light propagation in fiber optic is based on successive total internal reflection at the core-cladding boundary. According to the Snell's law, fields that enter the core at incident angle less than θ_{MAX} , keep propagating inside the fiber without penetrating into the cladding. Using basic rules of geometric optics, θ_{MAX} is related to the fiber indexes by:

$$\sin(\theta_{\text{MAX}}) = \sqrt{n_c^2 - n_d^2} \tag{2.2}$$

In practice, depending on the incident angle, different light rays can traverse different paths inside the fiber referred to as *propagation modes* of the light. Modes are indeed the possible solutions of the Helmholtz equations that are derived from the underlying Maxwell equations and the corresponding boundary conditions [24]. Each mode corresponds to a specific transverse distribution of the light energy. The number and characteristics of these modes are determined by the core and cladding refractive indexes as well as the core radius, a . To approximate the number of propagating modes at wavelength λ , We define the normalized frequency as:

$$V = \frac{2\pi}{\lambda} a \sqrt{n_c^2 - n_d^2} \tag{2.3}$$

It is shown that as long as $V < 2.405$, the fiber supports only one mode named fundamental mode [25]. Such a fiber is called single-mode fiber (SMF). In contrary, multi-mode fiber (MMF) allows for the propagation of several optical modes. The large core area of MMFs facilitates coupling of the light into optical fibers; however, as the modes travel at different speeds (a phenomena known as *modal dispersion*), the existence of several modes leads to the interference of successive bits which strongly limits the distance-throughput of optical

links. Therefore, in fiber optic communication systems where high transmission speed in long distances is required, SMF is preferable which is the case in our forthcoming experiments.

Today's standard SMFs are termed as SMF-28 which exhibit a single-mode operation at wavelengths longer than 900 nm. In the past few years, new type of fibers such as micro-structured fibers have been developed in which guiding is achieved through manipulation of the waveguide structure rather than its index of refraction [26]. Such fibers are built of single material (usually silica) and light guiding is obtained through the presence of air holes in the area surrounding the solid core. The holes are often arranged in the regular pattern in two dimensional arrays. Photonic crystal fibers (PCF) are considered a subgroup of micro-structured fibers where propagation occurs within a photonic defect or due to photonic bandgap effect [27].

2.1.1 Linear Effects

As the light propagates inside SMF, the corresponding electromagnetic wave undergoes absorption and dispersion which are due to the waveguide properties and would be proportional to the field intensity. Such processes are considered as linear effects which in general degrade the quality of the optical pulses and limit the performance of the communication systems.

Absorption

Traveling through any material, light is subject to propagation losses. These losses have various origins but we can group them all into a single absorption coefficient, α and write:

$$P_{\text{out}} = P_{\text{in}} e^{-\alpha L} \quad (2.4)$$

where P_{in} is the light input power and P_{out} is the corresponding output at distance L . This coefficient is generally expressed in dB/km by α_{dB} which is derived from α by:

$$\alpha_{\text{dB}} = \frac{P_{\text{dB}}^{\text{out}} - P_{\text{dB}}^{\text{in}}}{L \text{ [km]}} \simeq 4.4341 \alpha \quad (2.5)$$

Given an absorption coefficient α , a fiber has an effective length, L_{eff} defined by:

$$L_{\text{eff}} = \frac{1 - \exp(-\alpha L)}{\alpha} \quad (2.6)$$

The large absorption coefficient in the early stages of fiber development was due to silica impurities. Accordingly, as the fabrication process improved and the impurities were resolved, optical fiber loss reached the theoretical limits arising from Rayleigh diffusion. Figure 2.2 shows the absorption profile of a conventional SMF-28 as a function of wavelength. This absorption is very close to the Rayleigh diffusion limit over the transparent window in the 1300 nm-1600 nm wavelength range (approximately 50 THz). The peak which appears around 1390 nm is due to absorption of OH^- ions. Yet, with recent fabrication advances it can be reduced

Chapter 2. General Principles

down to the theoretical limit. For wavelengths longer than 1600 nm the intrinsic molecular absorption of the silica induces an additional loss as illustrated in the plot.

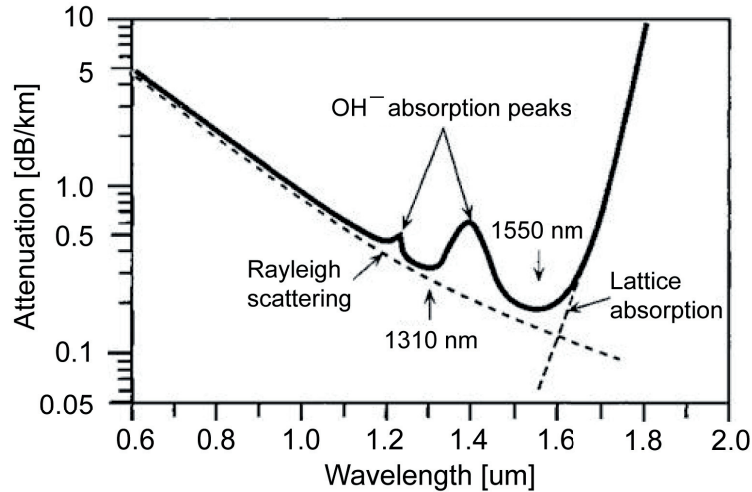


Figure 2.2 – Attenuation profile (solid line) of SMF-28 versus wavelength. Dashed line represents the theoretical limit which originates from Rayleigh scattering and silica intrinsic molecular absorption [25].

Chromatic Dispersion

The refractive index of silica is in essence frequency dependent. Therefore, each frequency component of a propagating signal travels at a different speed leading to pulse distortion at the fiber output. This phenomena is called *chromatic dispersion*. Dispersion has an important impact on propagation of optical pulses as a pulse has always a finite spectral width that can be affected and in consequence the pulse duration is modified [25]. If the pulse is initially unchirped, dispersion in a medium will always increase its duration. Yet, for a chirped pulse, dispersion can be employed for re-compression. When combined with the nonlinear effects, dispersion can give rise to the formation of *solitons* that are extremely short pulses of light.

In nonlinear optics, dispersion has manifold influences. Most notably, it determines the options for phase-matching of a parametric nonlinear process. It also limits the effective interaction length of short pulses via the velocity mismatch termed as temporal *walk-off*. Pulse broadening via dispersion is another factor which limits the nonlinear interaction length as it reduces the pulse peak power and therefore the efficiency of the nonlinear process.

Waveguide dispersion is a type of chromatic dispersion which arises from waveguide effects as the dispersive phase shift for a wave in a waveguide differs from that of a homogeneous medium. The total dispersion therefore is the combination of material dispersion and waveguide dispersion which becomes important in waveguides with small effective mode areas such as optical fibers. Waveguide dispersion may be tailored via the fiber design to obtain the

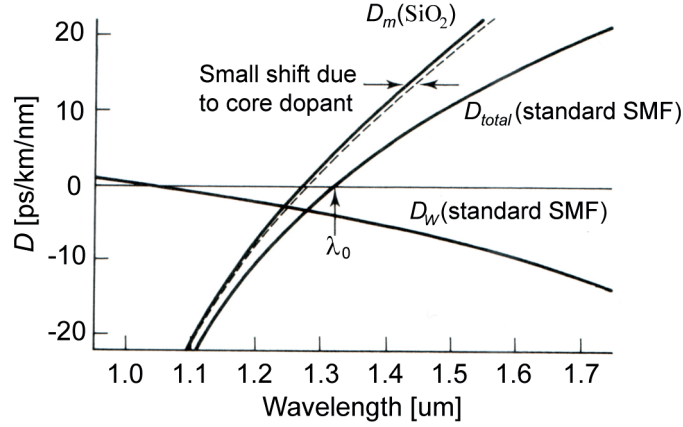


Figure 2.3 – Dispersion profile of silica, D_m (dashed line) and standard SMF, D_{total} (solid line) with ZDW around 1300 nm. The difference is due to the waveguide dispersion effect, D_W [25].

desired dispersion properties [28].

In optical communication, it is preferable to operate at wavelengths which are closer to the zero-crossing of dispersion curve termed zero-dispersion wavelength (ZDW). Operating in this region induces the minimum pulse broadening, increasing the data transmission distance. However, zero chromatic dispersion is not necessarily ideal for optical communication systems. Particularly for the transmission of multiple channels, the interference caused by inter-channel crosstalk becomes much stronger if the dispersion is too weak.

For conventional SMF the dispersion profile (D_{total}) is close to that of silica (D_m) with a zero-crossing around 1300 nm, see Fig. 2.3. Note that the corresponding difference is due to waveguide dispersion, denoted by D_W . Essentially, the dispersion profile can be expressed by a Taylor series where the propagation constant $\beta(\omega)$ can be expanded to:

$$\beta(\omega) = \beta(\omega_0) + \sum_{k=1}^{\infty} \frac{\beta_k}{k!} (\omega - \omega_0)^k \quad (2.7)$$

here β_k are the k th derivative of propagation constant at ω_0 . In practice, for telecommunication signals it is sufficient to account for up to the 4th dispersion order to cover all influential physical effects. These derivatives are also related to the group velocity, v_g by $\beta_1 = 1/v_g$ and $\beta_2 = -\frac{1}{v_g^2} \frac{dv_g}{d\omega}$. Note that β_2 which is called group velocity dispersion (GVD) and expressed in s^2/m , shows the dependence of the group velocity to the frequency. In telecommunications we also define dispersion coefficient, D which is directly expressed in wavelength (ps/km/nm) as:

$$D = \frac{d\beta_1}{d\lambda} = -\frac{2\pi c}{\lambda^2} \beta_2 \quad (2.8)$$

An operating region in which D is negative ($\beta_2 > 0$) it is called normal dispersion regime

Chapter 2. General Principles

whereas positive D ($\beta_2 < 0$) is denoted anomalous dispersion regime.

Even though the second order dispersion vanishes at ZDW, the dispersive effect is still present as the third order dispersion, β_3 becomes the dominant term close to the ZDW and must be considered especially for propagation of short pulses. To take this term into account, dispersion slope is defined as $D_S = dD/d\lambda$ and related to β_2 and β_3 through:

$$D_S = \frac{\omega}{\lambda^2} (2\beta_2 + \omega\beta_3) \quad (2.9)$$

2.1.2 Nonlinear Effects

Maxwell's equations are used to describe the interaction of the electromagnetic wave with the material in which the wave is propagating. The equations express that the electromagnetic field induces a polarization to the material. The propagation equation which takes this polarization into account would be:

$$\nabla^2 E = \frac{1}{c^2} \frac{\partial^2 E}{\partial t^2} + \mu_0 \frac{\partial^2 P}{\partial t^2} \quad (2.10)$$

where c is the speed of light in free-space and μ_0 is the permeability of the vacuum. We remind that we keep to the scalar field approximation. To solve Eq. 2.10 it is necessary to know the relation between polarization, P and electrical field, E . As long as P is only proportional to E we are in linear regime. However, once the field intensity is increased, the induced polarization itself will change the dipoles orientation and induce an extra polarization. This process is known as nonlinear polarization and is responsible for creating new harmonics from the initial electrical field. The induced polarization in a material in terms of the electrical field can be written as:

$$P = \epsilon_0 \left(\chi^{(1)} E + \chi^{(2)} E^2 + \chi^{(3)} E^3 + \dots \right) \quad (2.11)$$

The linear susceptibility, $\chi^{(1)}$ represents the linear effects experienced by the field through refractive index $n \approx \sqrt{1 + \text{Re}(\chi^{(1)})}$ and attenuation $\alpha \approx \frac{\omega}{c.n} \text{Im}(\chi^{(1)})$. Silica is a centroid-symmetry material which means the second order nonlinear susceptibility $\chi^{(2)}$ does not exist. However, the third order susceptibility $\chi^{(3)}$ is responsible for the Brillouin, Raman and Kerr effects that are described in the following.

Brillouin Effect

The *Brillouin* effect originates from the coupling of optical fields and acoustic waves via electrostriction. An incident photon in a medium can be converted into a scattered photon of slightly lower energy which usually propagates in the backward direction and an acoustic *phonon*. This effect can occur spontaneously even at low optical power, reflecting the thermally generated phonon field. For higher optical powers the optical fields substantially contribute

to the phonon population through a stimulated process. Above a certain threshold power, stimulated Brillouin scattering (SBS) can reflect most of the power of an incident beam.

The frequency shift of the reflected beam, referred to as Brillouin frequency shift, ν_B corresponds to the frequency of emitted phonon and is set by phase-matching requirement. For pure backward Brillouin scattering, the Brillouin shift can be calculated from the refractive index n , the acoustic velocity ν_a and the incident wavelength λ as:

$$\nu_B = \frac{2n\nu_a}{\lambda} \quad (2.12)$$

The Brillouin frequency shift depends on the material composition as well as temperature and pressure, through variations of ν_a . In optical fibers, Brillouin scattering essentially occurs in the backward direction. However, rather weak forward Brillouin scattering is also possible. For SMF-28 this shift is about 10 GHz.

The Brillouin threshold, P_B^{th} is another critical parameter defined as the input power for which the power of back scattered light is equal to the injected power. This power threshold is obtained by [29]:

$$P_B^{th} \approx \frac{21A_{\text{eff}}}{g_0L_{\text{eff}}} \frac{\Delta\nu_B + \Delta\nu_S}{\Delta\nu_B} \quad (2.13)$$

where A_{eff} is the effective area of the transverse mode, g_0 is the Brillouin gain coefficient, $\Delta\nu_B$ is the Brillouin line width and $\Delta\nu_S$ is the signal spectral width. Typical threshold power for SBS in optical communication fibers is in the order of few mW.

SBS indeed introduces the most stringent power limit for the amplification and the passive propagation of narrow-band optical signals in fibers. However, it can be suppressed by broadening the optical spectrum either by direct current modulation of the laser [30] or by external phase modulation [31]. This can be verified in Eq. 2.13 that increasing $\Delta\nu_S$ raises the SBS threshold. It is also possible to increase the threshold by increasing the effective core area or by distributing the Brillouin frequency down-shift using dopant concentration and temperature or strain gradient along the fiber [32, 33].

Among these various possibilities, phase modulation is an effective method to increase the SBS threshold. By applying an electrical signal to the phase modulator, one can adjust the power of the generated sidebands by tuning the electrical power. One common way is to modulate the phase by a pseudo random bit sequence (PRBS) signal [34]. An alternative method is to use several sinusoidal waves which amplitude and frequency are carefully chosen to broaden the spectrum evenly [31].

Raman Effect

Once vibrations of molecules in silica are induced by a strong field, photons will be generated at frequencies comparable to the optical frequency (order of 100 THz in silica). In this phenomena which is called *Raman* effect, one incident photon is converted into one lower energy photon and the difference of photon energies is carried away by a vibrational phonon similar to Brillouin effect. The generated light at higher wavelength is called *Stokes* wave. In principle, it is also possible that an already existing phonon interacts with a pump photon to generate one higher-energy photon, belonging to an *anti-Stokes* wave at a shorter wavelength. The latter process; however, is generally weak particularly at low temperatures. The generation of Stokes wave happens in a spectral range of 30 THz with a peak at 13 THz in silica fiber. The Raman power threshold which is defined as the input power at which the backscattered power is equal to the incident power is obtained by [35]:

$$P_R^{th} \approx \frac{16A_{\text{eff}}}{g_R L_{\text{eff}}} \quad (2.14)$$

where g_R is the Raman gain coefficient. Typical values of Raman threshold is much larger than Brillouin threshold for various fibers.

It is noteworthy that Raman effect allows for a gain band at Stokes side and an attenuation band at anti-Stokes side. This gain region is exploited to realize optical amplifiers. A larger gain bandwidth can be obtained by combining several pumps [36]. It is also possible to reach high wavelength ranges by concatenating Raman gains [37].

Kerr Effect

The optical *Kerr* effect is a nonlinear quasi-instantaneous phenomena which induces a modulation on the refractive index proportional to the injected power in the medium. The proportionality coefficient n_2 is referred to as nonlinear refractive index given by:

$$n_2 = \frac{3}{8n} \text{Re}(\chi_{nl}^{(3)}) \quad (2.15)$$

where $\chi_{nl}^{(3)}$ is a contribution of $\chi^{(3)}$ resulting from electrical dipoles inside the atoms. In this case we can define a Kerr index as:

$$n_{\text{Kerr}} = n + n_2 I \quad (2.16)$$

where I is the intensity of incident field. Although n_2 is relatively low in silica (order of 10^{-20} m^2/W), the long interaction length as well as very small effective area A_{eff} leads to a non-negligible Kerr effect in SMF. By taking all parameters into account the nonlinear characteristic of a medium can be expressed by nonlinear coefficient γ , defined as:

$$\gamma = \frac{2\pi n_2}{\lambda A_{\text{eff}}} \quad (2.17)$$

One phenomena that originates from the Kerr effect in an optical fiber is *self-phase modulation* (SPM). Due to the nonlinear refractive index, SPM induces a nonlinear phase shift after a propagation distance L , to the traveling optical wave given by [25]:

$$\Delta\Phi_{\text{SPM}} = \gamma PL \quad (2.18)$$

In case the power of incident wave is modulated, the time-varying phase term in Eq. 2.18 leads to a frequency chirp. This chirp is increased with the fiber length, producing new frequency components and thus continuously broadening the optical spectrum. In normal dispersion regime it also leads to pulse broadening. With CW waves, though the frequency chirp is removed, it is shown that the corresponding solution is unstable in anomalous dispersion regime [25]. Consequently the CW will break up due to small perturbations and grow exponentially with the fiber length. This process is referred to as *modulation instability* (MI).

Other similar effect to SPM is *cross-phase modulation* (XPM) with the exception that XPM requires at least two waves at different wavelengths. The wave at one wavelength is influenced by the additional wave through an extra phase term. The nonlinear phase shift due to XPM is given by [25]:

$$\Delta\Phi_{\text{XPM}} = 2\gamma P_2 L \quad (2.19)$$

where P_2 is the power of second optical wave. The factor 2 in E. 2.19 shows that XPM effect is doubled compared to the SPM for a certain pump power. Likewise SPM, modulated P_2 results in a chirp which might lead to the amplitude modulation after propagating in a dispersive medium.

Four-wave mixing is another phenomena which has its origin in Kerr effect. It can occur if at least two different frequency components propagate together in a nonlinear medium such as optical fiber. Modulation of refractive index at these frequencies, in effect creates two additional frequency components. As this process is central to this thesis it will be explained in details in section 2.2.

2.1.3 Modeling Light Propagation in Optical Fibers

To understand various phenomena in optical fiber, it is necessary to present a mathematical model for light propagation in this medium which takes the most influential linear and nonlinear processes into account. In this subsection we introduce the model that we used to provide the simulation results for the rest of the thesis. The forthcoming model is developed for co-propagating waves, therefore incapable to include Brillouin and Raman processes. However, as these two processes have negligible contribution to the experimental results this model can be safely used to verify the experimental data.

Nonlinear Schrödinger Equation

We assume that all propagating fields in fiber are co-polarized and that the birefringence effect is negligible; therefore, we can consider a scalar SVE. The propagation of electromagnetic fields is governed by Maxwell's equations. In optical fiber, these equations can be reduced to the nonlinear Schrödinger equation (NLSE) given by [25]:

$$\frac{\partial A}{\partial z} = -\frac{\alpha}{2}A + i \left(\sum_{k=2}^4 i^k \frac{\beta_k}{k!} \frac{\partial^k A}{\partial \tau^k} + \gamma |A|^2 A \right) \quad (2.20)$$

where A represents the amplitude of the fields SVE that evolve along the fiber. We assume a reference time window that is moving with group velocity speed $1/\beta_1$. To approximate dispersion around the ZDW with high accuracy, it is necessary to consider β_2 , β_3 (dispersion slope) and β_4 (dispersion curvature).

The last term in Eq. 2.20 represents the Kerr effect which is responsible for generating new harmonics and frequencies. To take the Raman process into account this term can be modified to [25]:

$$i\gamma \left((1 - \rho)|A|^2 + \rho \int_{-\infty}^{\tau} \chi R(\tau - t') |A|^2 dt' \right) A \quad (2.21)$$

where $\chi R(\tau)$ is the delayed Raman response [38] and ρ denotes the contribution of $\chi R(\tau)$ over the Kerr effect with typical value of 0.18 in silica fibers.

Split-Step Fourier Method

To understand and predict the propagation of optical fields in the fiber, one needs to solve Eq. 2.20. A rigorous solution of this equation is not efficient in terms of computation and memory. However, there are a few techniques which help solving this problem in an efficient way, such as *split-step Fourier* (SSF) method [39]. In this technique Eq. 2.20 can be treated as the form $\frac{\partial A}{\partial z} = (\tilde{D} + \tilde{N})A$ where \tilde{N} is the nonlinear operator ($i\gamma|A|^2$) and \tilde{D} is the differential operator taking fiber dispersion and absorption into account ($-\frac{\alpha}{2} + i \sum_{k=2}^4 i^k \frac{\beta_k}{k!} \frac{\partial^k}{\partial \tau^k}$). Therefore, this equation can be solved stepwise in z as $A(z + \Delta z) = A(z) e^{(\tilde{D} + \tilde{N})\Delta z}$. From a numerical point of view it is much easier to deal with the operator $e^{\tilde{N}}$ in time domain and the operator $e^{\tilde{D}}$ in frequency domain. In this case the SSF method can be approximated by:

$$e^{(\tilde{D} + \tilde{N})\Delta z} = e^{\tilde{D}\frac{\Delta z}{2}} e^{\tilde{N}\Delta z} e^{\tilde{D}\frac{\Delta z}{2}} \quad (2.22)$$

This means in a Δz interval, the equation is first solved in frequency domain in $\frac{\Delta z}{2}$ interval then by converting back to the time domain we solve the nonlinear operator in time domain over Δz , and finally by reverting back to the frequency domain we complete the solution of linear operator over $\frac{\Delta z}{2}$ interval. The error that corresponds to this solution compared to the direct solution is in the order of $O(\Delta z^3)$. This method can be implemented in a way leading

to rapid numerical solution that is much more efficient than other finite element methods [25, 40].

2.2 Optical Parametric Amplifiers

In a Kerr medium such as optical fiber, the nonlinear coupling between distinct waves at two or three frequencies generates a wave at new frequency. This process which is named *four-wave mixing* (FWM) results from intensity modulation of the refractive index via Kerr effect and involves transferring energy between one or two *pumps*, a *signal* and an *idler*. Fiber optic parametric amplifiers (FOPA) operate based on this energy transfer occurring between four waves.

From a quantum point of view this process corresponds to the annihilation of two pump photons and creation of a photon at signal and another photon at idler frequency, such that energy is conserved. In case the two pumps are at the same frequency it is called a *degenerate* process (single-pump) and if they are at two different frequencies the process is termed *non-degenerate* (dual-pump). In this section we review the basics of FOPA in single or dual-pump schemes. We study the underlying wave propagation equations and obtain the conditions in which an efficient interaction takes place between waves.

2.2.1 Single-Pump Parametric Amplifier

The simplest way to realize parametric amplification is to use a degenerate pump. This process is based on FWM interaction between a pump at angular frequency ω_P and the signal and idler respectively at ω_S and ω_I . In this case the law of conservation of energy requires that:

$$2\omega_P = \omega_I + \omega_S \quad (2.23)$$

With these three waves, we can write the combined SVE of the fields around ω_P as $A = A_I \exp(-i((\omega_I - \omega_P)t - (\beta_I - \beta_P)z)) + A_P + A_S \exp(-i((\omega_S - \omega_P)t - (\beta_S - \beta_P)z))$ where β_I , β_P and β_S are respectively the propagation constants of the idler, pump and signal angular frequency. For simplicity of theoretical analysis we neglect other harmonics that are created through FWM of the fields. By inserting the combined field into NLSE and performing the mathematics, we obtain:

$$\begin{aligned} \frac{dA_P}{dz} &= i\gamma \left((|A_P|^2 + 2|A_S|^2 + 2|A_I|^2) A_P + 2A_P^* A_S A_I \exp(i\Delta\beta_L z) \right) \quad (a) \\ \frac{dA_S}{dz} &= i\gamma \left((|A_S|^2 + 2|A_P|^2 + 2|A_I|^2) A_S + A_I^* A_P^2 \exp(-i\Delta\beta_L z) \right) \quad (b) \\ \frac{dA_I}{dz} &= i\gamma \left((|A_I|^2 + 2|A_S|^2 + 2|A_P|^2) A_I + A_S^* A_P^2 \exp(-i\Delta\beta_L z) \right) \quad (c) \end{aligned} \quad (2.24)$$

where $\Delta\beta_L = \beta_S + \beta_I - 2\beta_P$ is the linear phase-mismatch term and A_P , A_S and A_I are the pump,

Chapter 2. General Principles

signal and idler SVEs. The first term in the right side of Eq. 2.24 corresponds to the SPM and XPM of the fields and the second term associates to the FWM among fields.

We assume that the pump power $P = |A_P|^2$ is much higher than signal power P_S . As a result, P remains almost constant along the fiber (non-depleted pump approximation). In this case Eq. 2.24 is reduced to:

$$\begin{aligned} \frac{dA_P}{dz} &= i\gamma P A_P & (a) \\ \frac{dA_S}{dz} &= i\gamma \left(2PA_S + A_I^* A_P^2 \exp(-i\Delta\beta_L z) \right) & (b) \\ \frac{dA_I}{dz} &= i\gamma \left(2PA_I + A_S^* A_P^2 \exp(-i\Delta\beta_L z) \right) & (c) \end{aligned} \quad (2.25)$$

Equation 2.25 shows that Kerr effect is in principle induced by the pump power. It also shows the pump undergoes SPM leading to a pump field expression: $A_P = \sqrt{P} \exp(i\gamma P)$. Using this expression, Eq. 2.25 can be written as:

$$\begin{aligned} \frac{dA_S}{dz} &= i\gamma \left(2PA_S + A_I^* P \exp(i(\gamma P - \Delta\beta_L)z) \right) & (a) \\ \frac{dA_I}{dz} &= i\gamma \left(2PA_I + A_S^* P \exp(i(\gamma P - \Delta\beta_L)z) \right) & (b) \end{aligned} \quad (2.26)$$

According to Eq. 2.26 the signal and idler experience phase modulation by the pump and the FWM components produced from the interaction between pump and the conjugate of signal and idler. Note that the phase shift induced by pump on signal and idler is $2\gamma P$ referred to as the *nonlinear phase shift*. To further proceed with the equations we introduce modified signal and idler with $\frac{\Delta\beta}{2} - \gamma P$ phase shift. The new envelopes therefore would become $A'_S = A_S e^{i(\gamma P - \frac{\Delta\beta}{2})z}$ and $A'_I = A_I e^{i(\gamma P - \frac{\Delta\beta}{2})z}$. Rewriting Eq. 2.26 with new variables leads to:

$$\begin{aligned} \frac{dA'_S}{dz} &= i\frac{\kappa}{2} A'_S + i\gamma P A'_I^* & (a) \\ \frac{dA'_I}{dz} &= i\frac{\kappa}{2} A'_I + i\gamma P A'_S^* & (b) \end{aligned} \quad (2.27)$$

where κ is the phase-matching between pump, signal and idler and is defined as:

$$\kappa = 2\gamma P + \Delta\beta_L \quad (2.28)$$

In fact κ includes the contribution of linear and nonlinear phase shift in interaction between the fields. Combining equations 2.27(a) and (b), the general solution of A_S has the form of:

$$A_S = (ae^{gz} + be^{-gz}) e^{i(2\gamma P - \frac{\kappa}{2})z} \quad (2.29)$$

where

$$g^2 = (\gamma P)^2 - \left(\frac{\kappa}{2}\right)^2 \quad (2.30)$$

Equations 2.29 and 2.30 imply that the parametric gain on signal is obtained if the gain factor, g is real or equally if $|\kappa| \leq 2\gamma P$. For a phase-insensitive amplifier, where only the signal and pump fields are present at the fiber input we can write $A_S(z=0) = \sqrt{P_S}e^{i\phi_S}$ (ϕ_S is the initial phase of signal at fiber input) and $A_I(z=0) = 0$. Therefore, the solution of Eq. 2.27 is $a = b^* = \sqrt{P_S}e^{i\phi_S}(1 + i\frac{\kappa}{2g})$ and the parametric gain at the fiber output defined as $\frac{|A_S(z=L)|^2}{|A_S(z=0)|^2}$ would become:

$$G = 1 + \left(\frac{\gamma P}{g} \sinh(gL) \right)^2 \quad (2.31)$$

Since Eq. 2.31 is independent of the phase of input signal, this scheme is called *phase-insensitive* parametric amplification for which the necessary and sufficient requirement of amplification is the phase-matching condition. In case an idler is also present at the fiber input, the parametric gain would depend on the initial phase of signal and idler referring to as *phase-sensitive* parametric amplification [41]. Note that amplification of a high power input signal violates these results as the non-depletion pump assumption is not valid anymore.

Equation 2.30 suggests that it is possible to design amplifiers ($g > 0$) with large bandwidth by reaching the quasi phase-matching condition. It is therefore appropriate to express $\Delta\beta_L$ as a function of dispersion parameters at ω_P as:

$$\Delta\beta_L = 2 \sum_{k=1}^{\infty} \frac{\beta_{2k}}{(2k)!} (\Delta\omega_S)^{2k} \quad (2.32)$$

where $\Delta\omega_S$ is the frequency difference between signal and pump and β_{2ks} are the even derivatives of the propagation constant at pump angular frequency. As mentioned before, in practice it is sufficient to take β_2 and β_4 into account to model the phenomena inside the fiber [42]. Equations 2.31 and 2.32 show that the gain bandwidth is symmetric with respect to the pump angular frequency as it depends on even powers of $\Delta\omega$. Moreover, as the condition of quasi phase-matching is $-4\gamma P \leq \Delta\beta_L \leq 0$, we deduce that by increasing γ or P , the FOPA gain bandwidth is improved.

Figure 2.4 depicts a typical gain spectrum of single-pump FOPA. Two different gain regions can be identified on this plot. In the region close to the pump we can neglect $\Delta\beta_L$. The gain expression in this region is obtained by $G = 1 + (\gamma PL)^2$, called *parabolic* regime. In case the phase-matching condition is perfect ($\kappa = 0$), the gain region is called *exponential* with the expression $G = 1 + (\sinh(\gamma PL))^2$. Regarding the position of pump wavelength with respect to ZDW, if $\lambda_P > \lambda_0$ (anomalous dispersion regime, $\beta_2 < 0$) as the nonlinear phase-mismatch is always positive it can exactly compensate the linear phase-mismatch $\Delta\beta_L$ at some wavelength which corresponds to the perfect phase-matching condition. Note that the further λ_P is from λ_0 , the narrower gain region would become.

In normal dispersion regime where $\lambda_P < \lambda_0$ ($\beta_2 > 0$), the perfect phase-matching condition cannot be attained; only a parabolic gain would exist close to the pump region with an overall sinc-shaped spectrum centered on the pump wavelength. In the close neighborhood of λ_0

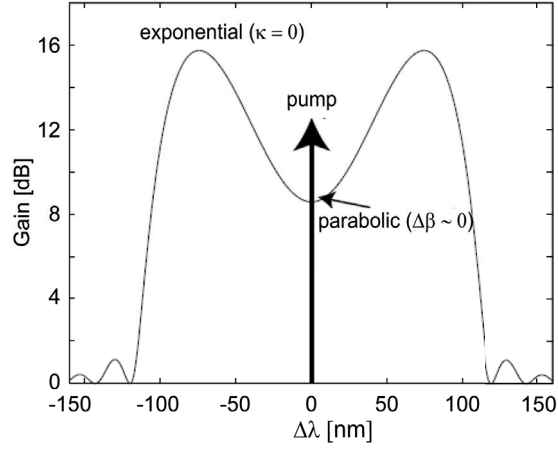


Figure 2.4 – Typical gain spectrum of single-pump FOPA. In the region close to the pump ($\Delta\beta_L \approx 0$) the gain is parabolic while for perfect phase-matching condition ($\kappa = 0$) the gain would be exponential.

which leads to $\beta_2 \approx 0$, the term with β_4 is responsible to provide the perfect phase-matching condition. As a result, very large gain bandwidths up to 100 nm can be obtained in this operating regime [43].

As illustrated in Fig. 2.4 the gain varies quite strongly over the specific wavelength range. On the other hand, phase-matching equation is a polynomial of the 4th order in $\Delta\omega_S$. Therefore, the roots of this equation are two symmetric pairs. To obtain perfect phase-matching at 4 distinct roots, it is essential to have $\beta_2 < 0$ and $\beta_4 > 0$. At this condition by setting the pump wavelength (and thus β_2) it is possible to obtain two symmetric bands around ω_P to produce a flat gain [42]. However, in all these cases the gain changes rapidly around the pumps as κ gets negative, limiting the possibility to realize a broadband flat gain region. One interesting approach for enabling a broadband gain is to concatenate several fibers with different dispersions. By changing the phase-matching condition, this technique allows to flatten the gain over a wide wavelength range; theoretically shown to reach 200 nm [44]. Another approach to generate a broadband flat gain is to implement dual-pump FOPA which is explained in the next subsection.

2.2.2 Dual-Pump Optical Parametric Amplifier

Compared to the single-pump scheme, dual-pump FOPA employs four distinct waves at different frequencies as shown in Fig. 2.5. Therefore, the fields SVE would be similar to the single-pump case except that A_P is replaced with $A_{P_1} + A_{P_2}$. Inserting the field expression into

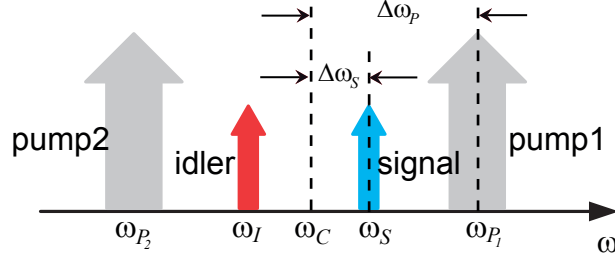


Figure 2.5 – Spectral model of four-wave interaction in dual-pump FOPA. ω_C is the central frequency of the two pumps. $\Delta\omega_S$ and $\Delta\omega_P$ are respectively signal and pump frequency difference with respect to ω_C .

NLSE, the coupled waves equations of the pumps, signal and idler are derived as:

$$\begin{aligned} \frac{dA_{P_1}}{dz} &= i\gamma \left((|A_{P_1}|^2 + 2|A_{P_2}|^2 + 2|A_S|^2 + 2|A_I|^2) A_{P_1} + 2A_{P_2}^* A_S A_I \exp(i\Delta\beta_L z) \right) \quad (a) \\ \frac{dA_{P_2}}{dz} &= i\gamma \left((|A_{P_2}|^2 + 2|A_{P_1}|^2 + 2|A_S|^2 + 2|A_I|^2) A_{P_2} + 2A_{P_1}^* A_S A_I \exp(i\Delta\beta_L z) \right) \quad (b) \\ \frac{dA_S}{dz} &= i\gamma \left((|A_S|^2 + 2|A_{P_1}|^2 + 2|A_{P_2}|^2 + 2|A_I|^2) A_S + 2A_{P_1}^* A_{P_2} \exp(-i\Delta\beta_L z) \right) \quad (c) \\ \frac{dA_I}{dz} &= i\gamma \left((|A_I|^2 + 2|A_S|^2 + 2|A_{P_1}|^2 + 2|A_{P_2}|^2) A_I + 2A_S^* A_{P_2} \exp(-i\Delta\beta_L z) \right) \quad (d) \end{aligned} \quad (2.33)$$

To continue solving Eq. 2.33, we assume a non-depleted operation regime where signal and idler power is small compared to the pumps power. In the same analogy to the single-pump scheme, if there is no idler field at the fiber input ($A_I(0) = 0$) the parametric amplification is phase-insensitive and the corresponding gain can be derived as [45]:

$$G = 1 + \left(\frac{2\gamma\sqrt{P_1 P_2}}{g} \sinh(gL) \right)^2 \quad (2.34)$$

where the FOPA gain factor g is obtained by:

$$g^2 = 4 \left(\gamma\sqrt{P_1 P_2} \right)^2 - \left(\frac{\kappa}{2} \right)^2 \quad (2.35)$$

and the phase-mismatch term is:

$$\kappa = \gamma(P_1 + P_2) + \Delta\beta_L \quad (2.36)$$

In Eq. 2.36, $\gamma(P_1 + P_2)$ is the nonlinear phase-mismatch and $\Delta\beta_L$ is the linear phase-mismatch between the interacting waves. We can develop $\Delta\beta_L$ with Taylor series around ω_C as:

$$\Delta\beta_L = \beta_2 (\Delta\omega_S^2 - \Delta\omega_P^2) + \frac{\beta_4}{12} (\Delta\omega_S^4 - \Delta\omega_P^4) \quad (2.37)$$

where $\Delta\omega_S = \omega_S - \omega_C$ and $\Delta\omega_P = \omega_{P1} - \omega_C$ are respectively the signal and pump frequency detuning from the pumps central frequency, ω_C . Compared to the single-pump FOPA, the phase-matching in dual-pump FOPA is not only a function of relative signal and pump position but also depends on pumps frequency difference. This offers a new degree of freedom to provide the quasi phase-matching between the interacting waves as will be explained in following.

Indeed, it has been shown that depending on the value of β_4 it is possible to obtain a quasi phase-matching condition which results in a flat gain between the pumps [42, 46]. In case $0 < \beta_4$ and $\beta_2 = 0$, κ would be minimized at ω_C . By setting the frequency difference and the power of the two pumps such that $(P_1 + P_2)/\Delta\omega_P^4 = \beta_4/(12\gamma)$, κ has a root at ω_C which is of the forth order and leads to a flat gain in a band between the pumps.

If the difference between the two pumps increases ($(\frac{\beta_4}{12\gamma(P_1+P_2)})^{1/4} < \Delta\omega_P$), κ would have two second order roots that are located symmetrically around ω_C between the two pumps. In this case if the roots are not close enough, the gain undergoes intensive variations. If $0 < \beta_2$, the value of κ increases compared to the previous condition. As a result, to retain the flat gain either $\Delta\omega_P$ should decrease or the pump power must increase. If $\beta_2 < 0$, κ can have four distinct roots between the two pumps. In this case it is possible to associate $\frac{\kappa}{\gamma(P_1+P_2)}$ to a forth order Chebychev polynomial, T_4 in a certain spectral range, $\Delta\omega_t$ between the two pumps. Note that this polynomial is defined as $T_4(x) = \cos(4 \cos^{-1}(x)) = 8x^4 - 8x^2 + 1$ over the interval $[-1, 1]$ and it has four roots over this interval.

If we choose the right value for β_2 based on the method explained in [42], we can realize a condition where $\frac{\kappa}{\gamma(P_1+P_2)} = \rho T_4\left(\frac{\Delta\omega_S}{\Delta\omega_t}\right)$ with $\rho < 1$. Adjusting pumps wavelength and frequency detuning therefore makes it possible to obtain a gain which oscillates with the order of ρ^2 over the bandwidth $\Delta\omega_t$ that is at least $(\frac{\beta_4}{12\gamma(P_1+P_2)})^{1/4}$. Figure 2.6 shows typical gain spectra of dual-pump FOPA respectively for high (Fig. 2.6(a)) and low (Fig. 2.6(b)) gain fluctuations. Note that if β_4 is negative, κ would have at least two roots outside the interval $[\omega_{P1}, \omega_{P2}]$. In this case to obtain a gain with minimum fluctuations, κ should have at least two roots inside the interval $[\omega_{P1}, \omega_{P2}]$ which is achieved by designing a positive β_2 .

The gain expression obtained for dual-pump FOPA is based on the interaction between four waves. However, in practice the number of interacting waves is higher. In a more accurate model, the two generated waves at the outer band of the pumps are also included in coupled wave equations. This analysis is called six-wave interaction model compared to former four-wave interaction model. The latter model does not have a closed form solution but can be solved numerically. Figure 2.6 depicts the gain spectrum for both four-wave (dashed line) and six-wave (solid line) interaction models. It is observed that four-wave model can be used to estimate the gain spectrum quite good in the wavelength range between the two pumps. However, close to the pumps one should employ six-wave model to get precise results. In the following sections we utilized four-wave model unless an analysis is required close to the pump where six-wave model will then be employed.

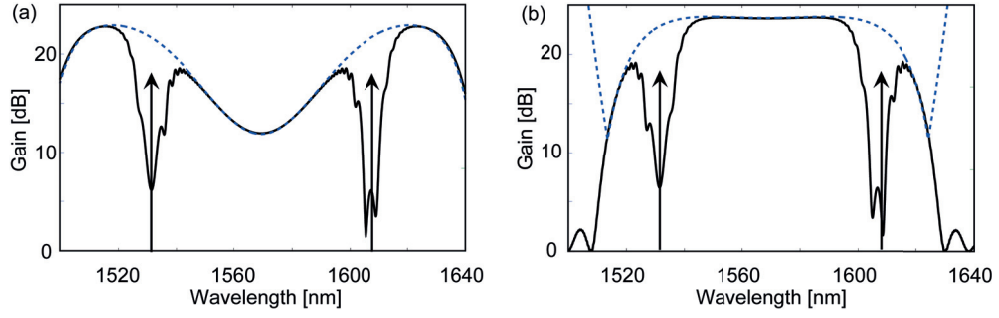


Figure 2.6 – Dual-pump FOPA gain spectrum for (a) high fluctuation and (b) low fluctuation. Dashed line depicts the four-wave interaction model while solid line represents the result of six-wave interaction model.

Table 2.1 – Comparing the characteristics of SMF, DSF, HNLF and PCF fiber type.

Fiber	SMF	DSF	HNLF	PCF
$A_{\text{eff}} (\mu\text{m}^2)$	70	60	10	6
α (dB/km) at 1550 nm	0.2	0.2	0.56	12
$\lambda_0 (\mu\text{m})$	1.27-1.30	1.55	1.4-1.9	1-2
D_S (ps/nm ² /km)	0.07	0.07	0.04	0.05
γ (W ⁻¹ km ⁻¹)	2	2	15	1100

2.3 State of Art in Single-Mode Fibers

Today various types of fibers with different properties are available in market, each suitable for specific application. Dispersion-shifted fiber (DSF) is one such type made to provide both low dispersion and low attenuation. This fiber is in fact a type of SMF with a core-cladding index profile tailored to shift the ZDW from the natural 1300 nm in silica to the minimum-loss window at 1550 nm. The shift is achieved by modifying the index profile and therefore making a more negative waveguide dispersion to offset the fixed material dispersion.

In this thesis we performed all the experiments with highly nonlinear fiber (HNLF). This type of fiber is receiving an increasing interest as it can offer high nonlinear coefficient, γ in the order of $12 \text{ W}^{-1}\text{km}^{-1}$ while maintaining a relatively low attenuation of 0.5 dB/km [47]. This combination along with being a DSF, makes HNLF suitable for parametric amplification. In order to improve the fiber nonlinearity, dopants such as GeO_2 can be used [48]. However, the loss of such fibers will increase due to the scattering from doped molecules.

Another approach to increase the nonlinear parameter is to reduce the effective area of the fiber core, A_{eff} . Yet, small core fibers require more precise manufacturing process and in general result in large ZDW variations along the fiber. PCFs that have been extensively developed in recent years also offer a very small core area. These fibers can be constructed by several capillary tubes that are stacked together in a specific pattern. It is possible to adjust fiber characteristics by designing the size of the holes and the distance between them [49].

Chapter 2. General Principles

Taking advantage of PCF high nonlinearity can reduce the fiber length in FOPA as the gain is proportional to γPL [50]. The reduction of fiber length is beneficial since the fiber would be less sensitive to environmental changes or longitudinal fluctuations. Though PCFs have very high nonlinear coefficient they still suffer from a considerable propagation and splicing losses. Table 2.1 compares the characteristics of a few type of fibers namely SME, DSE, HNLF and PCF. For fibers with broad range of parameters typical value is denoted.

3 Optical Short Pulse Generation Based on Parametric Amplification

In this chapter we study the FOPA functionality (single and dual-pump schemes), in pulsed pump regime. We show that by modulating the intensity of the pumps it is possible to generate pulses or time windows with high flexibility in terms of width and repetition rate. We investigate the characteristics of the generated time window in theory and verify it by experimental results. In particular, we obtain design rules for uniform generation of the time window over a large bandwidth. Later in chapter 4, we will demonstrate how this window is exploited in optical signal processing applications.

3.1 Introduction

Optical short pulse generation has been subject to a great interest due to its various applications in medical imaging, microscopy, spectroscopy as well as optical communication. One popular short pulse source is the mode-locked laser (MLL). A MLL is based on *Fabry-Perot* laser which consists of a gain medium of length L placed between two highly reflective mirrors. When the amplitude and phase conditions of the Fabry-Perot resonator are satisfied, the light that is bouncing in the cavity will constructively interfere and generate standing waves between the two mirrors. These waves correspond to the discrete set of favored longitudinal modes that are equally spaced in frequency at $\Delta\nu = \frac{c}{2nL}$ (n is the refractive index of the propagation medium). The frequency spacing and total number of modes for such laser depend on the cavity length and the bandwidth of the gain medium respectively.

In a simple Fabry-Perot laser, random phases of each individual mode induce random fluctuations to the output intensity. For lasers with hundreds of modes these interference effects tend to average out to near constant output intensity and the laser operation is known as continuous wave (CW). However, if the laser modes operate with a fixed relative phase, they would interfere constructively and produce a pulse of light instead. The period of this pulse is the inverse of modes frequency spacing and its duration is inversely proportional to the gain bandwidth.

Although various MLLs with remarkable performance in terms of amplitude and phase jitter with sub-picosecond duration have been realized [51], the strict phase-locking constraint results in a non-trivial operation as well as high sensitivity to external perturbation. Therefore, MLLs require complex and rigorous phase-locking arrangement to maintain stability. Moreover, not only is the repetition rate dictated by the cavity mode spacing, the gain bandwidth also limits the pulse duration and the operational wavelength. An alternative approach to generate optical short pulses is to employ a straightforward *cavity-less* technique. In this method an initial wide pulse is manipulated by nonlinear and/or dispersion effects to undergo a significant compression. In comparison to MLLs, cavity-less pulse generation takes advantage of single pass structure, allowing them to be less sensitive to environmental fluctuations. Another advantage is the possibility to easily tune the operating wavelength and the repetition frequency over a wide range without any need to adjust a cavity correspondingly.

One remarkable technique for cavity-less short pulse generation is using FOPA. As explained in previous chapter the underlying Kerr effect in FOPA leads to the interaction between signal and pump which generates the idler. In CW operating condition of signal and pump, the idler would be CW as well. However, when the pump is modulated in intensity the parametric gain will be gated in time creating a time window around signal and idler centered on the pump's peak. Owing to the nonlinear characteristics of the medium, this time window is compressed compared to the initial width of the pumps leading to the generation of a shorter pulsed signal and idler. In sections 3.2 we investigate pulse generation in single-pump FOPA and demonstrate how its characteristics vary depending on the phase-matching condition. In particular we show the possibility of Nyquist pulse generation in this scheme, under certain condition. In section 3.3 we study the characteristics of the generated pulses in dual-pump FOPA. We show by adjusting FOPA parameters, it is possible to create a uniform pulse source over a wide wavelength range, with high flexibility in terms of pulse shape and repetition rate. We also investigate new schemes in pulse generation by introducing dissimilar pump modulation.

3.2 Investigation of Pulse Generation in Single-Pump FOPA

We start this section by reviewing a recent theoretical investigation of pulse generation in single-pump FOPA [52]. We will then revisit the theory of pulse generation considering the impact of phase-matching on the pulse shape and width. Later, we will present a new mathematical approach to study the effect of walk-off and pump phase modulation. Finally, we demonstrate the experimental results to verify the theory.

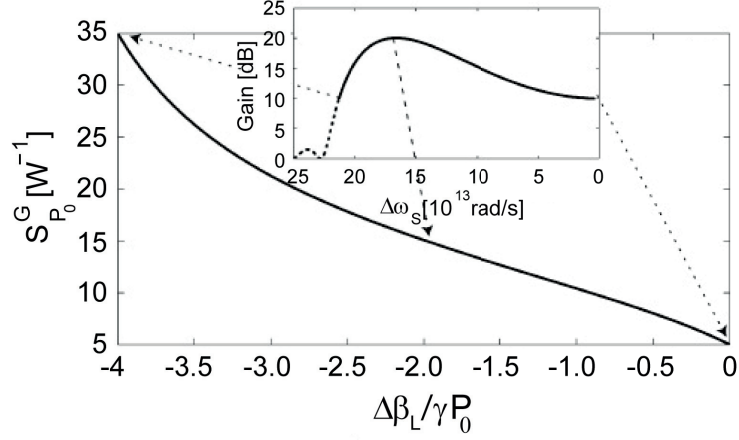


Figure 3.1 – Gain sensitivity as a function of normalized phase-mismatch, $\Delta\beta_L/\gamma P_0$. The inset illustrates gain spectrum for a typical HNLF with dispersion parameters $\beta_2 = 2.9 \times 10^{-29} \text{s}^2 \text{m}^{-1}$ and $\beta_4 = -6.4 \times 10^{-55} \text{s}^4 \text{m}^{-1}$. Maximum sensitivity is reached at $\Delta\beta_L/\gamma P_0 = -4$ phase-matching condition [52].

3.2.1 Theory

Gain Sensitivity to the Pump Power

We assume that the parametric pump, signal and idler are propagating in a HNLF, respectively at angular frequencies ω_P , ω_S and ω_I . Considering the energy conservation property of parametric process we have: $|\omega_I - \omega_P| = |\omega_S - \omega_P| = \Delta\omega_S$. As described in previous chapter, for non-depleted pump regime the slowly varying envelope (SVE) of the sinusoidal pump field becomes:

$$A_P(L, t) = A_P(0, t) e^{i\gamma|A_P(0, t)|^2 L} = \sqrt{P_0} \cos(\pi f_R \tau) e^{i\gamma P_0 \cos^2(\pi f_R \tau) L} \quad (3.1)$$

where γ is the nonlinear coefficient of the medium, L is the amplifying fiber length, f_R is the repetition rate of the pump and $\tau = t - z/v_g$ is the time in a reference frame moving at the pump group velocity. In Eq. 3.1 we assumed that SPM effect is dominant over dispersion along the fiber [53]. Using 3.1 the general expression for FOPA gain is derived as:

$$G(L, \tau) = \left(\frac{\gamma P(\tau)}{g(\tau)} \sinh(g(\tau) \times L) \right)^2 \quad (3.2)$$

where $P(\tau) = P_0 \cos^2(\pi f_R \tau)$ is the time varying pump intensity with $g^2(\tau) = (\gamma P(\tau))^2 - (\kappa(\tau)/2)^2$ and $\kappa(\tau) = 2\gamma P(\tau) + \Delta\beta_L$ is the phase-matching term between the pump, signal and idler. We know from the previous chapter that $\Delta\beta_L = \beta_2 \Delta\omega_S^2 + \beta_4 \Delta\omega_S^4/12$ is the linear phase-mismatch with β_2 and β_4 the dispersion and dispersion curvature at ω_P respectively. Note that $\Delta\beta_L$ is not time varying and solely depends on the fiber dispersion parameters and relative position of the waves ($\Delta\omega_S$). It is worth noting that almost all studies and demonstrations of pulse generation

Chapter 3. Optical Short Pulse Generation Based on Parametric Amplification

in FOPAs concentrate on $\kappa = 0$ condition corresponding to maximum gain regime. However, in the case of single-pump FOPA this region is very narrow (i.e. at a very specific detuning between pump and signal). Therefore, it is interesting to investigate the behavior of the generated pulses in other regimes by studying FOPA at different phase-matching conditions.

From Eq. 3.1 it is clear that the parametric gain decreases as the pump power is reduced. Yet, the rate at which the gain drops depends on the signal position. In order to investigate this dependency, we introduce the sensitivity of the gain relative to the pump power defined as [52]:

$$S_{P_0}^G = \frac{\partial \ln(G)}{\partial P_0} = \frac{\partial G / \partial P_0}{G} \quad (3.3)$$

$S_{P_0}^G$ can be interpreted as a measure of how sharp the idler normalized power drops with decreasing the pump power. This parameter is plotted in Fig. 3.1 as a function of $\Delta\beta_L$. Maximum sensitivity is reached when $\Delta\beta_L = -4\gamma P_0$ and it decreases as $\Delta\beta_L$ increases. The location of the highest sensitivity corresponds to the edge of the gain spectrum when $P(\tau) = P_0$. In other words when the pump power is decreased, the signal which is located at the edge of the gain spectrum will fall out of gain bandwidth sooner compared to signals located closer to the pump. As a result, $S_{P_0}^G$ would be the highest at the corresponding idler position and leads to the generation of idler pulses with shorter duration. Note that this location corresponds to the minimum idler gain, therefore leading to a trade-off between the generated pulse duration and peak power.

Pulse Duration and Shape

In this section we derive the expressions for idler pulse shape and duration at arbitrary phase-matching condition. Compared to the equations in [52] we use a more rigorous formulation to include more parameters and obtain a comprehensive solution. We consider the most general case where the pump, signal and idler SVEs evolve in time as $A_P(z, \tau)$, $A_S(z, \tau)$ and $A_I(z, \tau)$. Assuming negligible absorption and Raman scattering, the propagation of the waves inside the HNLF can be modeled by NLSE as:

$$\frac{\partial A}{\partial z} = i \left(\sum_{k=2}^{\infty} \frac{\beta_k}{k!} \frac{\partial^k A}{\partial \tau^k} + \gamma |A|^2 A \right) \quad (3.4)$$

Equation 3.4 is written in a time frame moving at the group velocity ($\tau = t - z\beta_1$) where γ is the nonlinear coefficient of the fiber and β_k are the k th derivative of propagation constant at ω_P . For the standard HNLF, knowledge of the dispersion (β_2), dispersion slope (β_3) and dispersion curvature (β_4) is sufficient to model all significant processes inside the fiber. Assuming A as the SVE of the total propagating electrical field we have: $A(z, \tau) = A_P(z, \tau) + A_S(z, \tau) e^{i\Delta\omega_S \tau} + A_I(z, \tau) e^{-i\Delta\omega_S \tau}$ with $\Delta\omega_S = \omega_I - \omega_P = \omega_P - \omega_S$. As in our study $\Delta\omega_S$ remains small compared to the Raman shift, excluding Raman process does not introduce any error. Assuming that the pump is undepleted ($|A_P| \gg |A_S|$), the coupled wave equations of propagating pump, signal

and idler can be written as:

$$\frac{\partial A_P}{\partial z} = i \left(\sum_{k=2}^4 \frac{\beta_k}{k!} \frac{\partial^k A_P}{\partial \tau^k} + \gamma |A_P|^2 A_P \right) \quad (a)$$

$$\frac{\partial A_S}{\partial z} = i \left(\sum_{k=2}^4 \frac{\beta_k}{k!} \left[\sum_{m=0}^k C_k^m \frac{\partial^m A_S}{\partial \tau^m} (i\Delta\omega_S)^{k-m} \right] + \gamma A_P^2 A_S^* \right) \quad (b) \quad (3.5)$$

$$\frac{\partial A_I}{\partial z} = i \left(\sum_{k=2}^4 \frac{\beta_k}{k!} \left[\sum_{m=0}^k C_k^m \frac{\partial^m A_I}{\partial \tau^m} (-i\Delta\omega_S)^{k-m} \right] + \gamma A_P^2 A_S^* \right) \quad (c)$$

where C_k^m is the binomial coefficient defined as $\frac{k!}{m!(k-m)!}$. The first term on the right side of Eqs. 3.5 accounts for dispersion phenomena and depends on the SVE through the time derivatives. Assuming that the pump is modulated by a single RF tone at frequency f_R , the pump power can be written as $P_P(0, \tau) = P_0 \cos^2(\pi f_R \tau)$ leading to an amplitude expression $A_P = \sqrt{P_0} \cos(\pi f_R \tau)$ where the pump initial phase was arbitrary set to zero without loss of generality. In case the dispersion length $D_L = 1 / \sum_{k=2}^4 \frac{\beta_k}{k!} (2\pi f_R)^k$ is much longer than the nonlinear length $L_{NL} = 1 / (\gamma P_0)$, only the SPM term should be considered in Eq. 3.5. The pump field output therefore is obtained as:

$$A_P(L, \tau) = \sqrt{P_0} \cos(\pi f_R \tau) e^{i\gamma P_0 \cos^2(\pi f_R \tau) L} \quad (3.6)$$

To solve Eqs. 3.4 for signal and idler, we assume that their bandwidth remain negligible compared to $\Delta\omega_S$ throughout the HNLF. In this case, the signal and idler SVE time derivatives can be neglected and the system of equations become similar to standard FOPA equations. The idler SVE at HNLF output can then be derived as:

$$A_I(L, \tau) = i A_S^*(0) \frac{\gamma P_0 \cos^2(\pi f_R \tau)}{g} \sinh(gL) \times e^{i(\gamma P_0 \cos^2(\pi f_R \tau) + \frac{\beta_3}{6} \Delta\omega_S^3) L} \quad (3.7)$$

where $g^2 = (\gamma P_0 \cos^2(\pi f_R \tau))^2 - (\kappa/2)^2$ and $\kappa = 2\gamma P_0 \cos^2(\pi f_R \tau) + \Delta\beta_L$ is the phase-mismatch term between the interacting waves. This term is composed of the time varying nonlinear phase shift ($2\gamma P_0 \cos^2(\pi f_R \tau)$) and the linear phase shift ($\Delta\beta_L = \sum_{k=1}^2 \frac{\beta_{2k}}{(2k)!} \Delta\omega_S^{2k}$) which is constant in time. Equation 3.7 implies that the shape of generated idler depends on the linear phase-mismatch and therefore on the relative pump-signal position, $\Delta\omega_S$ [52]. The phase term in Eq. 3.7 also signifies two effects. First, the generated pulses experience a chirp given by the expression $\gamma P_0 \cos^2(\pi f_R \tau)$ and second they undergo a walk-off relative to the pump that is equal to $\beta_3 \Delta\omega_S^2 / 2$. The fact that walk-off between the generated pulse and the pump only depends on the dispersion slope has already been demonstrated experimentally in parametric slow and fast light processes [54], likewise in modulation instability induced by a localized perturbation [55].

Assuming that the generated pulse width is short compared to the repetition period $1/f_R$, the pump power can be approximated by $P_P(L, \tau) \approx P_0(1 - (\pi f_R \tau)^2)$. As a result, g can be written

Chapter 3. Optical Short Pulse Generation Based on Parametric Amplification

as:

$$g = \sqrt{-\frac{\Delta\beta_L}{4}(4\gamma P_0 + \Delta\beta_L) \left(1 - \frac{4\gamma P_0}{4\gamma P_0 + \Delta\beta_L}(\pi f_R \tau)^2\right)} \approx g_0 \left(1 - \frac{2\gamma P_0}{4\gamma P_0 + \Delta\beta_L}(\pi f_R \tau)^2\right) \quad (3.8)$$

where $g_0 = g(\tau = 0) = \sqrt{-\Delta\beta_L(4\gamma P_0 + \Delta\beta_L)/4}$. The approximated g is valid as long as $\frac{2\gamma P_0}{4\gamma P_0 + \Delta\beta_L}$ is small. Since g is in the denominator of Eq. 3.7, one can safely use Taylor expansion provided that $2\gamma P_0 < 4\gamma P_0 + \Delta\beta_L$, which is equivalent to $\kappa(\tau = 0) \geq 0$. Performing the calculation, Eq. 3.7 becomes:

$$A_I(L, \tau) = i A_S^*(0) \frac{\gamma P_0}{g_0} \left(1 - \frac{2\gamma P_0 + \Delta\beta_L}{4\gamma P_0 + \Delta\beta_L}(\pi f_R \tau)^2\right) \sinh \left(g_0 L \left(1 - \frac{2\gamma P_0}{4\gamma P_0 + \Delta\beta_L}(\pi f_R \tau)^2\right) \right) \times e^{i \left(\gamma P_0 \cos^2(\pi f_R \tau) + \frac{\beta_3}{6} \Delta\omega_S^3 \right) L} \quad (3.9)$$

Note that $\kappa(\tau = 0) \geq 0$ corresponds to the portion of the spectrum that is located between the pump location and the maximum gain location. For large $g_0 L$, one can write in the vicinity of $\kappa = 0$:

$$A_I = i A_S^*(0) \frac{\gamma P_0}{g_0} \frac{e^{g_0 L \left(1 - \frac{2\gamma P_0}{4\gamma P_0 + \Delta\beta_L}(\pi f_R \tau)^2\right) + i \left(\gamma P_0 (1 - (\pi f_R \tau)^2) + \frac{\beta_3}{6} \Delta\omega_S^3 \right) L}}{2} \quad (3.10)$$

Equation 3.10 results in the same Gaussian pulse expression obtained in [56]. The full-width half maximum (FWHM) of generated pulses is derived as:

$$T_{\text{FWHM}} = \frac{1}{\pi} \sqrt{\frac{2 \ln(2)}{\gamma P_0 L}} \times \frac{1}{f_R} \quad (3.11)$$

Note that Eq. 3.10 is only valid for large $g_0 L$ and $\kappa(\tau = 0) \geq 0$ which corresponds to a narrow portion of the gain bandwidth. In particular, when $\kappa(\tau = 0) = -2\gamma P_0$ which represents a signal located at the edge of parametric gain spectrum, we have $g \approx 2\pi i \gamma P_0 f_R \tau$ leading to:

$$A_I = i A_S^*(0) \gamma P_0 L \text{sinc}(2\pi \gamma P_0 L f_R \tau) e^{i \left(\gamma P_0 \cos^2(\pi f_R \tau) + \frac{\beta_3}{6} \Delta\omega_S^3 \right) L} \quad (3.12)$$

where the sinc function is represented by $\text{sinc}(x) = \sin(x)/x$. The FWHM of generated pulses in this case would be:

$$T_{\text{FWHM}} \approx \frac{0.443}{\gamma P_0 L} \times \frac{1}{f_R} \quad (3.13)$$

The expression in Eq. 3.12 shows a new approach for generating all-optical near-sinc pulses which have potential applications in WDM-Nyquist transmission. We will study these special pulses in detail in chapter 5.

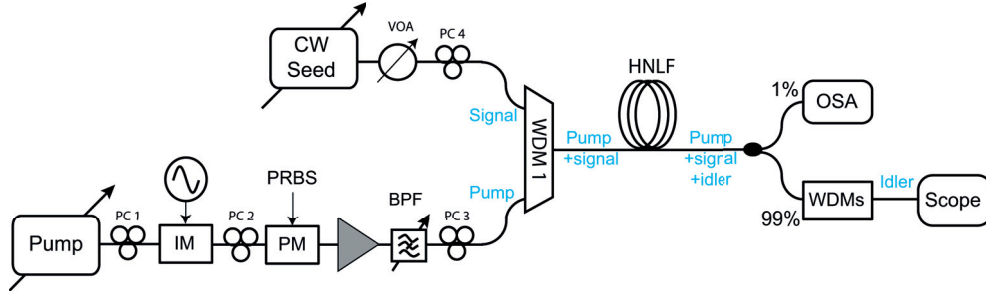


Figure 3.2 – Experimental setup for pulse generation in single-pump FOPA. PC: polarization controller; IM: intensity modulator; PM: phase modulator; BPF: bandpass filter; WDM: wavelength division multiplexer; HNLF: highly nonlinear fiber; OSA: optical spectrum analyzer [57].

3.2.2 Experiment

Figure 3.2 illustrates the experimental setup used to investigate pulse generation in single-pump FOPA. A CW tunable laser with high OSNR is used as the FOPA pump. The pump is intensity modulated by a sinusoidal wave and subsequently phase modulated by a pseudo random bit sequence (PRBS) in order to suppress the stimulated Brillouin scattering (SBS). Note that to suppress amplitude fluctuations by pump phase modulation on the generated pulses, it is necessary to delay the PRBS in a way that pump phase jumps do not coincide with the generated pulses [52]. The pump power is amplified by an EDFA and then filtered by a 2 nm width bandpass filter to eliminate ASE. Another tunable CW laser is used as the signal which power is controlled by a variable optical attenuator (VOA). The signal and pump are coupled by a wavelength division multiplexer (WDM) and launched into a HNLF with the length $L = 500$ m and the average zero dispersion wavelength (ZDW) of $\lambda_0 = 1551$ nm. The nonlinear coefficient of the fiber and the corresponding dispersion slope are measured $\gamma = 12$ $W^{-1}km^{-1}$ and $\beta_3 = 27 \times 10^{-3}$ $ps.nm^{-2}km^{-1}$ respectively. At the HNLF output the parametric process is monitored by a 1% tap on an optical spectrum analyzer (OSA). The remainder of the light is passed through a WDM to block the pump and filter out the idler. The idler is then monitored by a 500 GHz optical sampling oscilloscope and an OSA. To investigate and validate our developed theory of pulse generation, the signal envelope was swept from the Gaussian condition $\Delta\beta_L = -2\gamma P_0$ to beyond the sinc-shaped condition ($\Delta\beta_L = -4\gamma P_0$). We also investigated the effect of signal power on the pulse shape.

3.2.3 Results and Discussions

In the first experiment we set the FOPA pump at $\lambda_P = 1557$ nm (anomalous dispersion) and modulate its intensity with a 40 GHz sinusoidal wave. The average pump power inside the HNLF is 410 mW. To obtain Gaussian and sinc-shaped pulses we calculated according to theory the signal position to be $\lambda_S = 1566.6$ nm and $\lambda_S = 1570.3$ nm respectively. Figure 3.3 shows the optical spectra at the HNLF output corresponding to the two signal positions. The FOPA gain at

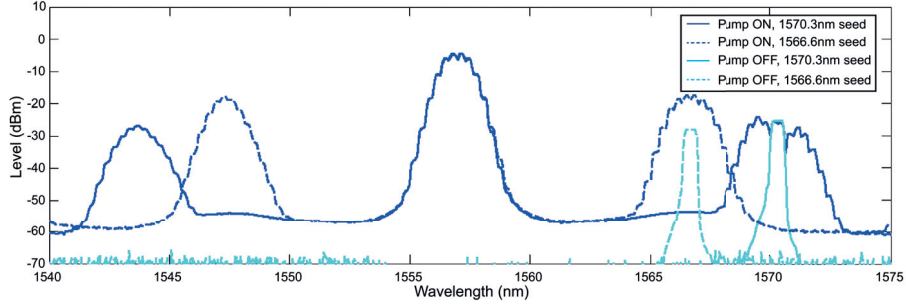


Figure 3.3 – Optical spectra at the HNLF output for pump ON and OFF with signal seed position at $\lambda_s = 1566.6 \text{ nm}$ ($\Delta\beta_L = -2\gamma P_0$) and $\lambda_s = 1570.3 \text{ nm}$ ($\Delta\beta_L = -4\gamma P_0$) [57].

Gaussian condition is 14 dB while at sinc-shaped position it reduces to 3 dB. Figure 3.4 shows the temporal and spectral profile of the generated pulses at Gaussian and near-sinc condition. An extra case with signal at $\lambda_s = 1570.5 \text{ nm}$ (beyond sinc condition) is included for comparison. The first column in Fig. 3.4 shows the temporal waveform detected on a 500 GHz optical sampling scope. It is observed that the generated idler exhibits a significant compression compared to the input sinusoidal wave. Moreover, the pulse shape varies depending on the linear phase-mismatch as predicted by theory. The second column depicts the corresponding idler spectrum taken with 0.02 nm precision. One can check that the spectra shape evolves along with the pulse temporal shape. Near the sinc-shaped position, the spectrum bandwidth is larger as the pulse width is reduced. Note that ideally the spectral shape of a sinc-shaped pulse is square. However, the pump induced chirp that was discussed before, modifies the spectrum by redistributing the energy to the higher harmonics. And finally the third column illustrates the simulation results from VPIphotonics platform as well as the theoretical fits. Comparing experimental and simulation results shows an excellent agreement not only in terms of pulse width but also noise. The theoretical fits confirm the linear phase-mismatch of $\Delta\beta_L = -2.2\gamma P_0$ for the Gaussian condition, $\Delta\beta_L = -3.98\gamma P_0$ at near-sinc condition and $\Delta\beta_L = -4.12\gamma P_0$ for beyond the sinc condition.

To further investigate pulse generation, signal wavelength was swept between $\lambda_s = 1565 \text{ nm}$ and $\lambda_s = 1572.8 \text{ nm}$. The pump wavelength was moved to $\lambda_p = 1556 \text{ nm}$ in this case to optimize the utilization of WDM filter which blocks/filters the pump/idler. Therefore, the idler pulses are generated over the interval $\lambda_I = 1539.5 \text{ nm}$ to $\lambda_I = 1547.1 \text{ nm}$. We also tried three different signal power level of 0 dBm, 3 dBm and 6 dBm for all wavelength sweeps. The results are plotted in Fig. 3.5. For low input signal power the shape of the generated idler evolves from Gaussian profile to near-sinc profile. When the signal wavelength exceeds the gain limits, a strong distortion of the pulses can be observed. The FWHM of the idler pulses start decreasing as the wavelength gets closer to the edge of gain spectrum. When the signal power is high enough the pump is depleted by the signal that is close to the exponential gain region. This leads to distorted idler pulses that are widened compared to the low input power signals. For signals closer to the edge of parametric gain, the low gain avoids depletion and the near-sinc pulse shapes are not affected. In general, increasing the signal power generates wider pulses

3.2. Investigation of Pulse Generation in Single-Pump FOPA

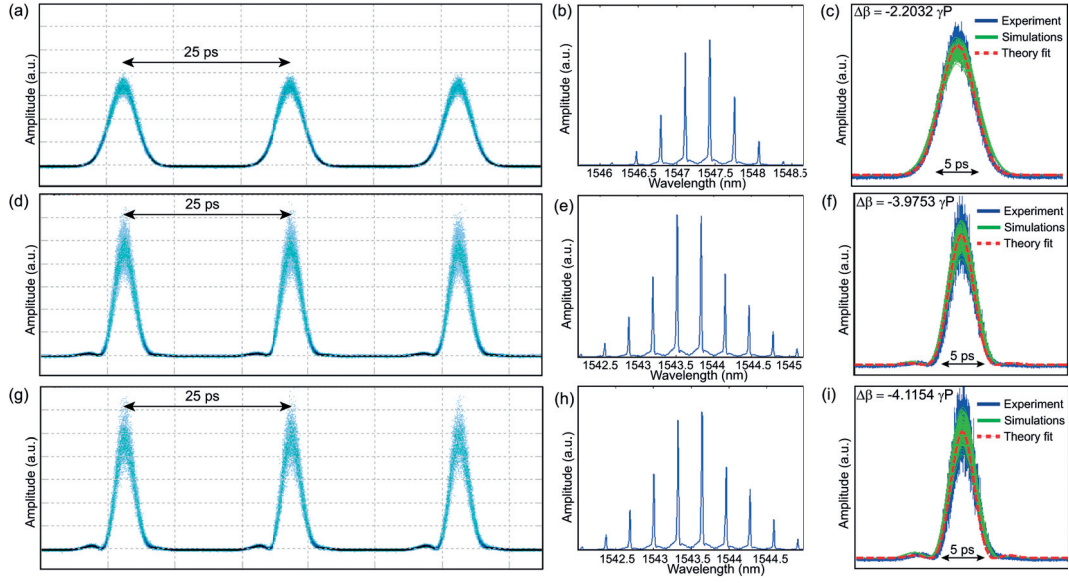


Figure 3.4 – For a pump at $\lambda_P = 1557$ nm, (a) idler waveform and (b) spectrum for the signal at $\lambda_S = 1566.6$ nm; (c) Experiment, simulation and theoretical fit for the signal at $\lambda_S = 1566.6$ nm corresponding to $\Delta\beta_L = -2.2\gamma P_0$; (d) idler waveform, (e) spectrum for the signal at $\lambda_S = 1570.3$ nm; (f) Experiment, simulation and theoretical fit for signal at $\lambda_S = 1570.3$ nm corresponding to $\Delta\beta_L = -3.97\gamma P_0$; (g) idler waveform, (h) spectrum for the signal at $\lambda_S = 1570.5$ nm (i) Experiment, simulation and theoretical fit for signal at $\lambda_S = 1570.5$ nm corresponding to $\Delta\beta_L = -4.11\gamma P_0$ [57].

for signals close to the exponential gain regime. Figure 3.5(b) also shows how FWHM of the generated pulses evolves as a function of signal wavelength for 0 dBm, 3 dBm and 6 dBm input power. The pulse width decreases in all input powers as the signal approaches the edge of gain bandwidth. However as the signal power increases, the pulse width close to Gaussian position becomes wider due to the pump depletion effect. When the signal position gets closer to the sinc-shaped position the pulse width for all signal power levels start converging. For 0 dBm input power the comparison between experimental FWHM, the FWHM from numerical simulation and the theoretical values obtained from non-depleted pump regime is demonstrated in Fig. 3.5(d) where a very good agreement is observed.

For a better comparison Fig. 3.6 shows sample pulses at various phase-matching condition when the pump wavelength was set at $\lambda_P = 1556$ nm with peak power of 650 mW. The signal power is swept from 0 dBm to 6 dBm and its position was selected at $\lambda_S = 1568.6$ nm, $\lambda_S = 1570$ nm and $\lambda_S = 1572$ nm to respectively approximate the condition $\Delta\beta_L = -2\gamma P_0$, $\Delta\beta_L = -3\gamma P_0$ and $\Delta\beta_L = -4\gamma P_0$. As illustrated for signals located further from the pump, the generated pulses become noisier. In fact with an increase in $\Delta\omega_S$, $\Delta\beta_L$ decreases and therefore the parametric gain becomes more sensitive to pump power fluctuations [52]. Note that these results are previously verified in studies of noise and signal degradation in CW pump regime [56]. Figure 3.6 shows that at high signal power the pulse peak is clipped at Gaussian position because of the pump depletion. For larger signal detuning, depletion is avoided and the

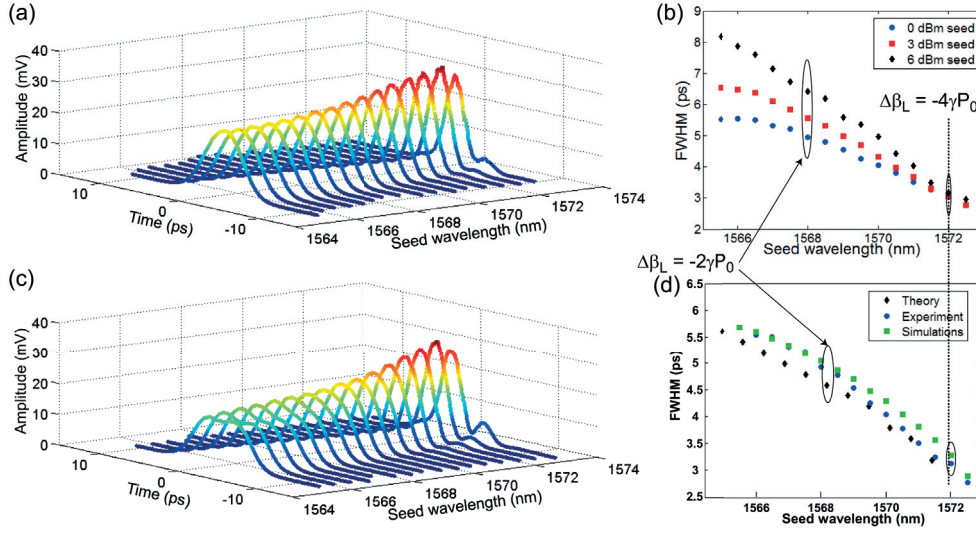


Figure 3.5 – Evolution of idler pulse shape as a function of signal wavelength for (a) 0 dBm signal power and (c) 6 dBm signal power. (b) Experimental full width half maximum (FWHM) of generated idler pulse as a function of signal wavelength for 0 dBm, 3 dBm and 6 dBm of signal power (d) Comparison of the experimental, simulated and theoretical FWHM of generated idler for 0 dBm signal power [57].

Table 3.1 – SNR (dB) of generated pulses corresponding to Fig. 3.6

Signal power [dBm]	$\Delta\beta_L = -2\gamma P_0$ (Gaussian)	$\Delta\beta_L = -3\gamma P_0$	$\Delta\beta_L = -4\gamma P_0$ (sinc)
0	27.58	22.43	15.9
3	31.15	25.78	19.2
6	31.38	30.13	20.9

generated pulses exhibit less noise at higher input power. The corresponding SNR is denoted in Table. 3.1. We verified that for any signal position there is an optimum seed power which provides the highest SNR.

Figure 3.6 also illustrates an asymmetry in generated pulses which is essentially due to *walk-off*. This effect is investigated as shown in Fig. 3.7, by generating sinc-shaped pulses at lower repetition rates. For $f_R = 2.75$ GHz no asymmetry is observed. As the repetition rate is increased, the pump, signal and idler pulses become shorter, but also due to walk-off the interacting pulses loose their overlapping along the fiber leading to pulse asymmetry. Indeed walk-off is an important issue in generating symmetric pulses at high repetition rates. To have a better understanding of the walk-off origin, we preform a mathematical analysis which includes the first order derivative of the SVEs in Eq. 3.5. We can align the fields phases with the pump phase rotation by $B_S = A_S e^{i\gamma P_0 \cos^2(\pi f_R \tau) z}$. Considering $|\frac{\partial B_S}{\partial \tau}|^2 \ll |B_S \gamma P_0 z \pi f_R|$ and

3.2. Investigation of Pulse Generation in Single-Pump FOPA

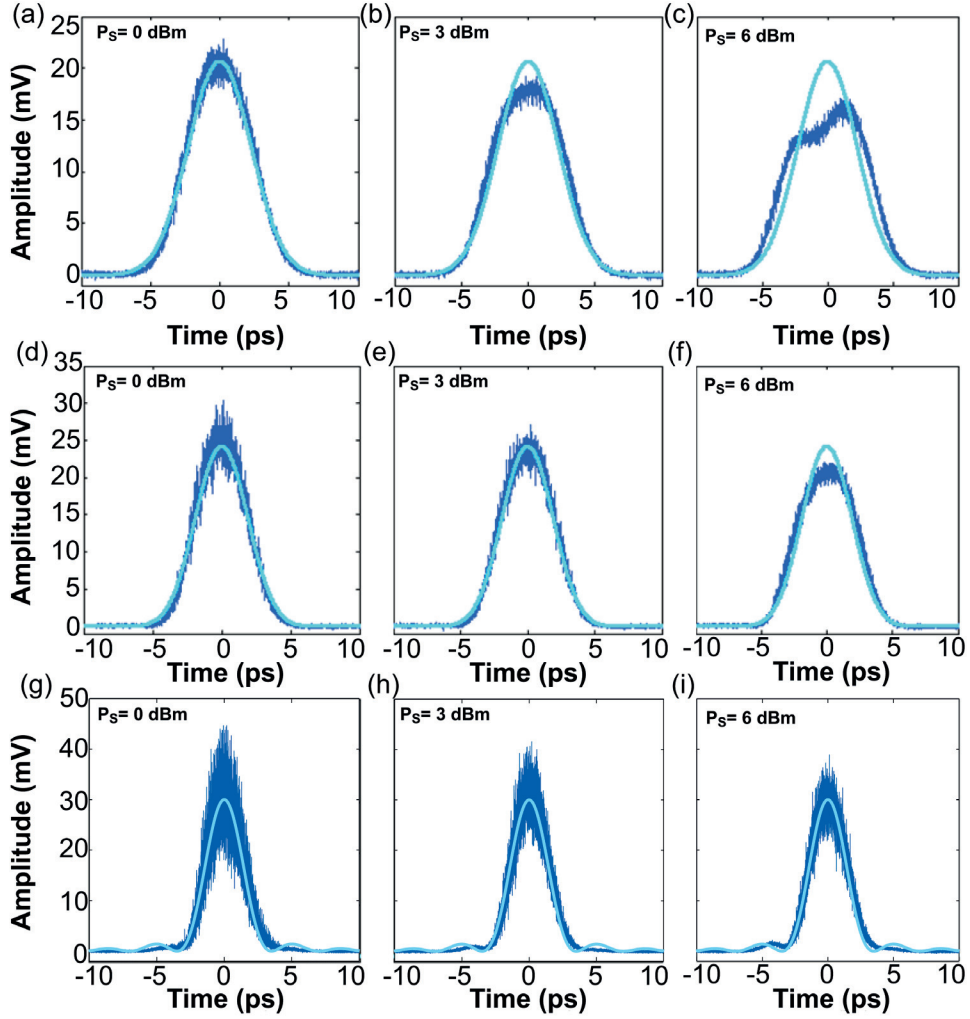


Figure 3.6 – Idler pulse shapes for (a)-(c) $\Delta\beta_L = -2\gamma P_0$, (d)-(f) $\Delta\beta_L = -3\gamma P_0$ and (g)-(i) $\Delta\beta_L = -4\gamma P_0$ at three different signal power level [57].

making the following change of variable:

$$B_k = C_k e^{\alpha_k i \left\{ \frac{\beta_3}{6} \Delta\omega_S^3 z + \gamma P_0 \pi f_R \sin(2\pi f_R \tau) \left(\frac{\beta_2}{2} \Delta\omega_S + \frac{\beta_4}{12} \Delta\omega_S^3 \right) z^2 \right\}} \quad K = S, I \quad (3.14)$$

with $\alpha_I = +1$ and $\alpha_S = -1$, the following equation can be derived:

$$\frac{\partial^2 C_{S,I}}{\partial z^2} = \left[(\gamma P_0 \cos^2(\pi f_R \tau))^2 - \left(\frac{\kappa + WOz}{2} \right)^2 + i \frac{WO}{2} z \right] C_{S,I} \quad (3.15)$$

where $WO = \beta_3 \gamma P_0 \pi f_R \sin(2\pi f_R \tau) \Delta\omega_S^2$. Equation 3.15 can be solved using complicated hypergeometric functions, which do not provide any valuable physical insight [42]. Yet, this equation clearly shows that the phase-matching term, κ is increased by WOz that is a function of dispersion slope and the pump derivative. It also shows that κ is incremented for shorter times

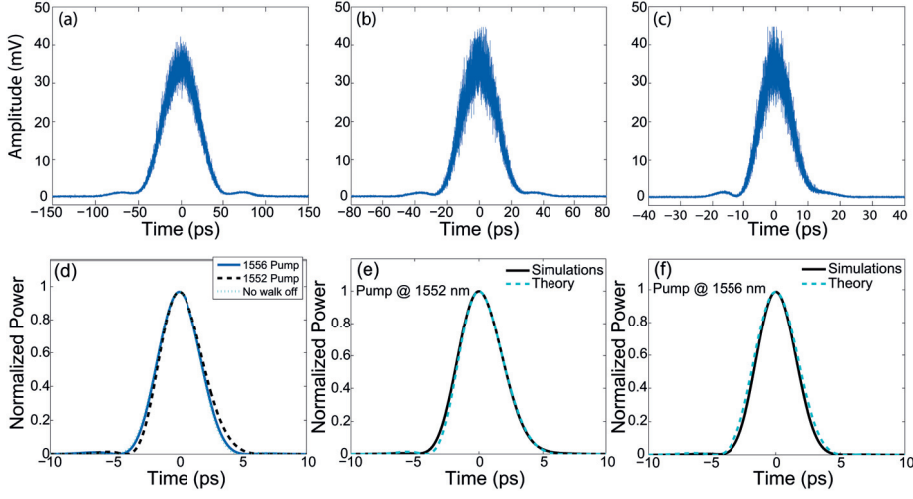


Figure 3.7 – Idler waveform at near-sinc position for repetition rate (a) 2.75 GHz, (b) 5.5 GHz and (c) 11 GHz. (d) Comparing idler pulse shapes for $\Delta\beta_L = -4\gamma P_0$ with pump position at $\lambda_P = 1552$ nm (dashed line), $\lambda_P = 1556$ nm (solid line) and theoretical fit from Eq. 3.12 for pump position at (e) $\lambda_P = 1552$ nm and (f) $\lambda_P = 1556$ nm at 40 GHz repetition rate [57].

and decremented for longer times compared to the ideal case. Note that a higher detuning of signal and pump ($\Delta\omega_S$) increases the asymmetry. This behavior is verified in Fig. 3.7 by showing the simulated sinc pulses for a pump located at $\lambda_P = 1556$ nm and $\lambda_P = 1552$ nm. The asymmetry of the sinc-shaped pulse is enhanced for the pump at $\lambda_P = 1552$ nm as the signal is located further than pump in this case. By replacing κ with $\kappa + WO \times L$ in Eq. 3.10, the obtained pulse shapes are in a better agreement with simulation results, reinforcing the physical insight of Eq. 3.15.

3.3 Investigation of Pulse Generation in Dual-Pump FOPA

Despite the many capabilities of single-pump FOPA in manipulating optical signals, new important features can be obtained when using dual-pump FOPA. For instance it enables generating a flat gain region over a wide wavelength range, in comparison to single-pump scheme. In addition, the possibility of modulating two pumps independently, provides more flexibility in pulse generation context.

In this section we study the generation of short pulses based on dual-pump FOPA. Similar to the previous section we introduce the concept of gain sensitivity and then study the impact of FOPA parameters on the generated pulses. Moreover, we will present design rules for generating uniform pulses over a wide wavelength range. Finally, the theoretical studies are verified by experiment.

3.3.1 Theory

As explained in section 2.2.2, dual-pump FOPA operates based on non-degenerate FWM where two high power pumps at angular frequencies ω_{P_1} and ω_{P_2} are launched into a HNLF together with a signal at ω_S which is located in the middle range of the two pumps. The conservation of energy requires $\omega_{P_1} + \omega_{P_2} = \omega_S + \omega_I$ where ω_I is the angular frequency of the generated idler. Considering only the interaction between these four waves, this model is referred to as two sideband (TS) interaction model. However, in case the signal is located close to either of the pumps, the TS model is not applicable and one should take the two sidebands generated out of pumps band into account to obtain an accurate gain spectrum in that range [58]. The latter model is referred to as four-sideband (FS) interaction model which can be solved numerically.

The energy transfer efficiency from the two pumps to the signal and idler is mainly determined by the phase-matching condition between pumps, signal and idler. Assuming scalar fields, negligible loss and no pump depletion, the idler gain based on (TS) model can be written as:

$$G_I = \left(\frac{r}{g} \sinh(gL) \right)^2 \quad (3.16)$$

where r and gain coefficient, g are obtained by:

$$\begin{aligned} r &= 2\gamma\sqrt{P_1P_2} & (a) \\ g^2 &= r^2 - (\kappa/2)^2 & (b) \end{aligned} \quad (3.17)$$

In Eq. 3.17, γ represents the nonlinear coefficient of the waveguide while P_1, P_2 refer to the pumps peak power. We define P_0 as the total pump power ($P_0 = P_1 + P_2$). Also $\kappa = \Delta\beta_L + \Delta\beta_{NL}$ is the total phase-matching between the interacting waves which consists of linear phase-mismatch $\Delta\beta_L$ induced by fiber dispersion and nonlinear phase-mismatch $\Delta\beta_{NL}$ due to the cross-phase modulation of the pumps given by:

$$\begin{aligned} \Delta\beta_L &= \beta_2(\Delta\omega_S^2 - \Delta\omega_P^2) + \frac{\beta_4}{12}(\Delta\omega_S^4 - \Delta\omega_P^4) & (a) \\ \Delta\beta_{NL} &= \gamma(P_1 + P_2) = \gamma P_0 & (b) \end{aligned} \quad (3.18)$$

Denoting $\omega_C = (\omega_{P_1} + \omega_{P_2})/2$ as the central angular frequency of the two pumps, we can define signal and pump detuning from ω_C as $\Delta\omega_S = \omega_S - \omega_C = (\omega_S - \omega_I)/2$ and $\Delta\omega_P = \omega_{P_1} - \omega_C = (\omega_{P_1} - \omega_{P_2})/2$. In Eq. 3.18, β_2 and β_4 are respectively the second and fourth order dispersion coefficients of the fiber at ω_C .

Gain Sensitivity

Now we define the gain sensitivity parameter, $S_{P_0}^G$ as:

$$S_{P_0}^G = \frac{\partial G / \partial P_0}{G} = \frac{\partial \ln(G)}{\partial P_0} \quad (3.19)$$

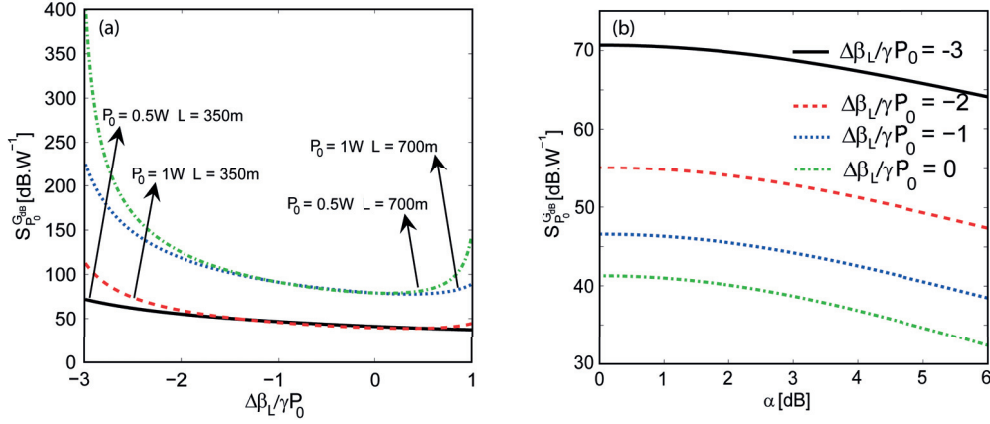


Figure 3.8 – (a) Gain sensitivity as a function of normalized phase-mismatch, $\Delta\beta_L/\gamma P_0$ for different total pump power and HNLF length. (b) Gain sensitivity as a function of pumps power ratio $\alpha = |P_1/P_2|$ for different normalized phase-mismatch terms [59].

The expression in Eq. 3.19 is a measure of how sharp the parametric gain G varies with small fluctuations δP_0 from the total pump power, P_0 . Thus, high sensitivity signifies that pump fluctuations and leads to more intense change of signal and idler power. Using the partial derivative rule, Eq. 3.19 can be decomposed into two terms as: $S_{P_0}^G \delta P_0 = S_{P_1}^G \delta P_1 + S_{P_2}^G \delta P_2$. The closed form mathematical expression of $S_{P_{1,2}}^G$ which is derived in Appendix A.1 is as following:

$$S_{P_0}^G = \frac{1}{P_n} - \frac{\gamma}{g^2} (4\gamma P_{3-n} - \kappa/2) + \frac{L\gamma}{g} (4\gamma P_{3-n} - \kappa/2) \coth(gL) \quad n = 1, 2 \quad (3.20)$$

Equation 3.20 shows that sensitivity parameter is a function of $\Delta\beta_L$ through κ . Note that $S_{P_0}^G$ has unit of $1/W$ while a more practical definition is $S_{P_0}^{G_{dB}}$ in dB/W which is obtained by: $S_{P_0}^{G_{dB}} = \partial \log(G)/\partial P_0 = 10 S_{P_0}^G / \log(10) \approx 4.343 \times S_{P_0}^G$, measuring gain variations in dB for 1 Watt of total pump power variation.

Figure 3.8(a) shows the sensitivity parameter as a function of normalized phase-mismatch term, $\Delta\beta_L/\gamma P_0$ for different values of P_0 and L in a typical HNLF with $\gamma = 15 \text{ W}^{-1}\text{km}^{-1}$. We assumed that the pumps have equal power i.e. $P_1 = P_2$. It is verified that for equal pumps power, $S_{P_0}^{G_{dB}}$ is always strictly positive meaning that if the total pump power decreases, FOPA gain shrinks at a higher rate. Therefore, it can be deduced that when the pumps are modulated by sinusoidal waves with total peak power P_0 , the generated signal and idler pulses will become narrower. For all simulated cases shown in Fig. 3.8 the highest sensitivity is obtained for $\Delta\beta_L = -3\gamma P_0 L$. The mathematical proof of this statement is provided in Appendix A.1. Figure 3.8(a) shows that the sensitivity behaves differently when changing either L or P_0 as is the case with the parametric gain. In fact doubling the length of HNLF leads to an intense increase of the sensitivity, while doubling P_0 increases the sensitivity only close to the extreme values of $\Delta\beta_L/\gamma P_0$. Figure 3.8(b) illustrates the effect of unequal pump power on the sensitivity. In this figure, assuming constant total pump peak power ($P_0 = 0.5 \text{ W}$), the sensitivity is plotted as a function of power ratio, $\alpha = |P_1/P_2|$. The results show that gain sensitivity is decreased

3.3. Investigation of Pulse Generation in Dual-Pump FOPA

as the power imbalance increases. From Eqs. 3.19 and 3.20 one can find that P_1 and P_2 have symmetrical influence in power imbalance. Note that Eq. 3.20 is in a very good agreement with FS interaction model for $0.25 \leq \alpha \leq 1$.

Generation of Optical Short Pulses in Dual-Pump FOPA

Investigating the gain sensitivity showed that when pumps are periodically modulated, shorter pulses are generated at signal and idler sides. Besides, we can set the desired sensitivity level by selecting appropriate linear phase-mismatch $\Delta\beta_L$, HNL length L and pumps peak power P_0 . As we seed the FOPA with CW signal, the generated pulse at signal side experiences a constant optical power. As a result a higher extinction ratio is obtained on the idler side. Therefore, in this study we only focus on pulse generation at the idler side.

In general, the two pumps can be modulated with two arbitrary waveforms. However, in the rest of this thesis we consider the case of sinusoidal intensity modulation, where the pumps power can be written as:

$$P_n(t) = P_{n0} \cos^2(\pi f_n t + \phi_n) \quad n = 1, 2 \quad (3.21)$$

Equation 3.21 implies that by tuning frequencies f_1 , f_2 and phases ϕ_1 , ϕ_2 as well as the gain sensitivity, pulses with various repetition rate and pulse width can be obtained. For example in case the FOPA is designed such that it has a high sensitivity when the pumps peak coincide in time, there would be significant gain only at that instant and as a result the pulses will be generated at a period which is the least common multiple of $1/f_1$ and $1/f_2$. This expresses the potential of dual-pump FOPA as a flexible pulse generator in terms of repetition rate and pulse width. As a first insight on pulse generation using dual-pump FOPA, we study the case of $f_1 = f_2 = f_R$ and $\phi_1 = \phi_2$. As a result, the period of generated pulses would be $1/f_R$. For the remainder of the thesis we assume that P_0 is the total peak power, i.e. $P_0 = P_{10} + P_{20}$. We also assume that the pumps power remain equal and undepleted as it was shown $P_{10} = P_{20}$ leads to the highest sensitivity and therefore shortest pulse. Note that in Fig. 3.8(b) the slope of sensitivity close to $\alpha = 0$ dB is small so that slight imbalance of the pumps power is tolerated.

By inserting Eq. 3.21 into Eqs. 3.16 and 3.17, we calculate the duty cycle ($DC = T_{FWHM} \times f_R$) of generated pulses as a function of $\Delta\beta_L/\gamma P_0$. The results are shown in Fig. 3.9(a) for $-3 \leq \Delta\beta_L/\gamma P_0 \leq 1$, using the same parameters as in Fig. 3.8. Figure 3.9(a) shows that the evolution of DC and $S_{P_0}^{G_{dB}}$ are inversely proportional to $\Delta\beta_L$. In fact the shortest pulse widths are obtained when $\Delta\beta_L = -3\gamma P_0$. Similar to Fig. 3.8(a) for higher P_0 and L , an inflexion point is obtained which shifts towards lower values of $\Delta\beta_L$. Yet, converse to the gain sensitivity, with doubling P_0 or L , DC would drastically decrease in a similar way for both parameters. Figure 3.9(b) depicts the peak gain as a function of $\Delta\beta_L/\gamma P_0$. As predicted, the highest peak gain of pulses is obtained for perfect phase-matching condition at the pumps peak power ($\Delta\beta_L = -\gamma P_0$) corresponding to exponential gain regime whereas the lowest pulses peak gain is obtained in parabolic regime with $\Delta\beta_L = -3\gamma P_0$ or $\Delta\beta_L = +\gamma P_0$. As a result, Figs. 3.9(a) and (b) depict a

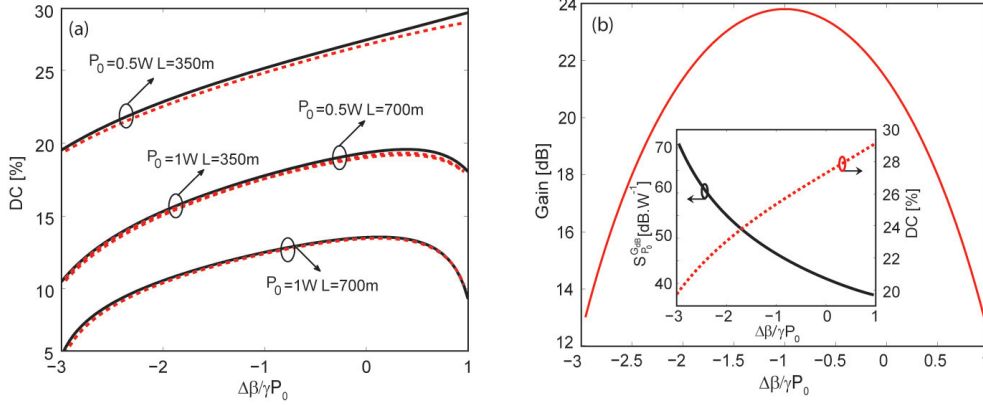


Figure 3.9 – (a) Idler duty cycle (DC) defined as $DC = T_{FWHM} \times f_R$ versus normalized phase-mismatch $\Delta\beta_L/\gamma P_0$, obtained by numerical solution (solid line) and empirical equation in Eq. 3.24 (dashed line) (b) FOPA gain as a function of normalized phase-mismatch, $\Delta\beta_L/\gamma P_0$ for $P_0 = 0.5$ W and $L = 350$ m. The inset shows the inverse relation between DC and $S_{P_0}^{G_{dB}}$ [59].

trade-off between pulse peak power and pulse width likewise the pulse generation in single-pump FOPA [56].

To obtain further insight on the behavior of generated pulses and regarding the gain sensitivity discussion, it would be sufficient to study pulse generation in the vicinity of pumps peak power and use the following approximation:

$$P(z, t) \approx P_0 (1 - (\pi f_R t)^2) \quad (3.22)$$

where $P(z, t)$ is the total pump power. This approximation is valid as long as the generated pulse width is small compared to the repetition rate. By replacing Eq. 3.22 in Eqs. 3.16 and 3.17 we derive the closed-form analytical expression for temporal gain in Appendix A.2 at $\Delta\beta_L = +\gamma P_0 (G_1)$, $\Delta\beta_L = -\gamma P_0 (G_{-1})$ and $\Delta\beta_L = -3\gamma P_0 (G_{-3})$ as:

$$G_{-3}(t) \approx (\gamma P_0 L)^2 \text{sinc}^2(\sqrt{3}\gamma P_0 L f_R t) \quad (a)$$

$$G_{-1}(t) \approx \exp(2\gamma P_0 L)/4 \times \exp(-2\gamma P_0 L(\pi f_R t)^2) \quad (b) \quad (3.23)$$

$$G_1(t) \approx (\gamma P_0 L)^2 \text{sinc}^2(\gamma P_0 L f_R t) \quad (c)$$

where $\text{sinc}(x) = \sin(\pi x)/(\pi x)$. Equations 3.23(a) and (b) show the generated pulses in exponential gain regime exhibit a Gaussian profile, while those generated in parabolic gain regimes experience near-sinc shape. This latter pulse is of particular interest as it has many application in sampling and optical communication. Using the closed form expression, one can obtain the value of DC in each case. Knowing from the inset in Fig. 3.9(a) that DC and $S_{P_0}^G$ are inversely proportional, the general empirical relation of DC can be obtained using linear regression as:

$$DC = \frac{1}{\pi} \sqrt{\frac{2 \ln(2)}{\gamma P_0 L}} + \frac{0.62}{\sqrt{P_0}} \left(\frac{1}{\ln(S_{P_0}^G)} - \frac{1}{\ln(2\gamma L \coth(\gamma P_0 L))} \right) \quad (3.24)$$

3.3. Investigation of Pulse Generation in Dual-Pump FOPA

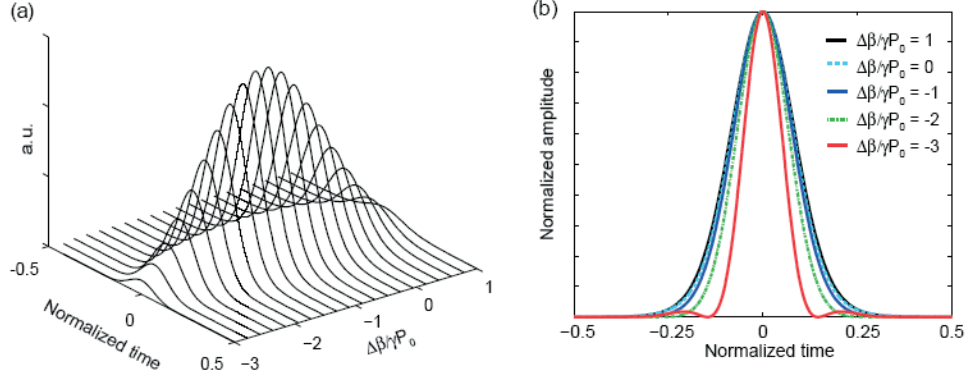


Figure 3.10 – (a) Idler pulse shape over one period as a function of $\Delta\beta_L/\gamma P_0$, (b) Normalized intensity of idler pulses over one period for different values of normalized phase-mismatch, $\Delta\beta_L/\gamma P_0$ [59].

Equation 3.24 is depicted in Fig. 3.9(a) (dashed line) and shows a very good agreement with duty cycles obtained from numerical solutions (solid line). Figures 3.10(a) and (b) show idler pulse evolution as a function of $\Delta\beta_L/\gamma P_0$ for $L = 350$ m and $P_0 = 0.5$ W. We checked that for $\Delta\beta_L = -\gamma P_0$ and $\Delta\beta_L = -3\gamma P_0$ the pulse shape fits well with the analytical formula. In the case $\Delta\beta_L = +\gamma P_0$, the DC can be obtained by Eq. 3.23 but the sinc shape is not retrieved. The reason is when the pulse width is too long, Eq. 3.23 does not fit the generated pulse over the entire period. It can be verified that for higher P_0 or L , the pulse expression fits the generated pulses. Therefore, in order to generate near-sinc shape pulses, it is preferable to operate at $\Delta\beta_L = -3\gamma P_0$.

Generation of Identical Shaped Pulses Over a Wide Bandwidth

In the former subsection it was shown how pulse shape and width varies depending on the linear phase-mismatch $\Delta\beta_L$. In this part we will show one can bound $\Delta\beta_L$ over a wide bandwidth and therefore generate uniform pulse shapes over that bandwidth. This feature is a significant advantage of dual-pump FOPA compared to single-pump FOPA where $\Delta\beta_L$ is essentially different at different signal detuning from pump frequency. Note that this bounding was first shown in CW pump operation of dual-pump FOPA in exponential gain regime [42]. The novelty of this work is the proof that such bounding can be extended to any $\Delta\beta_L$ in the interval $[-3\gamma P_0, \gamma P_0]$.

Assuming that $m \in [-3, 1]$, when $\beta_2 \cdot \beta_4 < 0$, $\Delta\beta_L$ can be expressed in terms of Chebyshev polynomial as:

$$\frac{\Delta\beta_L}{\gamma P_0} = m + \rho T_4\left(\frac{\Delta\omega_S}{\Delta\omega_t}\right) \quad (3.25)$$

Chapter 3. Optical Short Pulse Generation Based on Parametric Amplification

where $T_4 = 8x^4 - 8x^2 + 1$ is the fourth order Chebyshev polynomial, ρ is the ripple in $\Delta\beta_L$, and $\Delta\omega_t$ designates half the bandwidth over which the ripple still remain between the Chebyshev extrema [42]. Using Eq. 3.18 the two sides of Eq. 3.25 are equal for any $\Delta\omega_S$ if and only if we have:

$$\begin{aligned} \Delta\omega_t &= \sqrt{-12 \frac{\beta_2}{\beta_4}} & (a) \\ \rho &= \frac{3}{2} \frac{\beta_2^2}{\beta_4 \gamma P_0} & (b) \\ \left(\frac{\beta_4}{12\gamma P_0} \right) \Delta\omega_P^4 + \left(\frac{\beta_2}{\gamma P_0} \right) \Delta\omega_P^2 + (\rho + m) &= 0 & (c) \end{aligned} \quad (3.26)$$

when the conditions in Eqs. 3.26 are satisfied, the normalized phase-mismatch term is bounded to m in the frequency range $2\Delta\omega_t$ with amplitude ripple of ρ . It worth noting that Eq. 3.26(c) has a valid solution if and only if $\text{sgn}(\beta_4)m < |\rho|$. Consequently, depending on the sign of β_4 and the value of m , four distinct operating region can be identified.

Type (i) corresponds to $\text{sgn}(\beta_4) > 0$, $m \in [-3, 0]$ and type (ii) to $\text{sgn}(\beta_4) < 0$, $m \in [0, 1]$, where $\text{sgn}(\beta_4)m$ is strictly negative and always satisfies the condition for any set of m and ρ . In these two cases m and ρ can be chosen arbitrary. To provide conditions so that $|\rho| < |m|$, (ripples are smaller than m) it is essential to set the pumps central frequency such that:

$$\beta_2 = -\frac{\beta_4 \Delta\omega_P^2}{3} \left[1 - \left(\frac{1}{2} - \frac{6m\gamma P_0}{\beta_4 \Delta\omega_P^4} \right)^{1/2} \right] \quad (3.27)$$

which leads to:

$$\Delta\omega_t = 2\Delta\omega_P \left[1 - \frac{1}{2} \left(1 + \left(\frac{\Delta\omega_4}{\Delta\omega_P} \right)^4 \right)^{1/2} \right]^{1/2} \quad (3.28)$$

where $\Delta\omega_4 = (12m\gamma P_0/\beta_4)^{1/4}$. Equations 3.27 and 3.28 show that as $\Delta\omega_P$ varies between $\Delta\omega_4$ and $2^{3/4}\Delta\omega_4$, $\Delta\omega_t$ ranges from 0 to $\Delta\omega_P$ while $|\rho|$ ranges from 0 to $|m|$. Therefore, there is a trade-off between the bandwidth of the pulses and the ripples in $\Delta\beta_L$ which induce fluctuations to the pulse width and peak power.

Type (iii) corresponds to $\text{sgn}(\beta_4) > 0$ and $m \in [0, 1]$ while in type (iv) we have $\text{sgn}(\beta_4) < 0$ and $m \in [-3, 0]$. For these two operating condition we always have $|m| < |\rho|$, indicating that the minimum achievable ripple would be more than the absolute value of m . As a result to confine the normalized phase-mismatch with low ripple, operating conditions of type (i) or (ii) should be employed. This analysis therefore shows that fibers with positive dispersion curvature (β_4) are useful in generating identical pulses over a wide bandwidth.

Figure 3.11(a) demonstrates how the ripples in $\Delta\beta_L/\gamma P_0$ influence the ripples of DC in a type (i) operating condition. Since the normalized phase-mismatch is bounded between $m - \rho$ and

3.3. Investigation of Pulse Generation in Dual-Pump FOPA

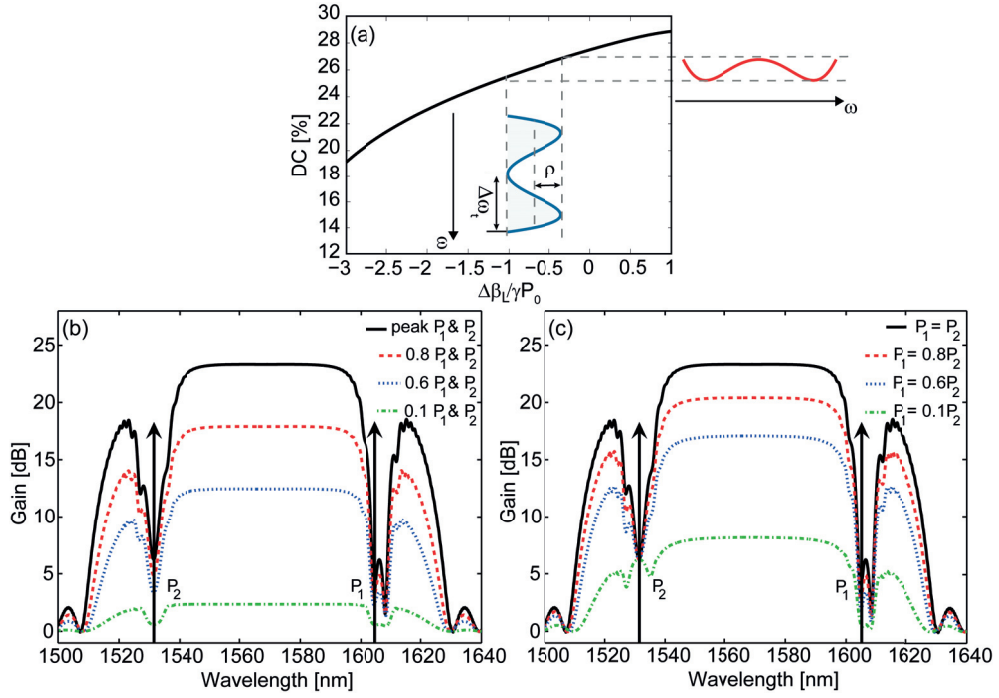


Figure 3.11 – Principle of pulse generation in dual-pump FOPA. As $\Delta\beta_L/\gamma P_0$ is bounded to m with a ripple ρ , the DC of generated pulses follow the same trend in frequency. Dual-pump FOPA gain spectra for (b) two synchronous modulated pumps, (c) one modulated and one CW pump. The peak power of each pump is $P_0/2 = 0.25$ W [59].

$m + \rho$ over $2\Delta\omega_t$, the DC of generated pulses will be confined to a certain value over the same bandwidth. The oscillation amplitude of DC is determined by ρ and the slope of the DC curve versus $\Delta\beta_L/\gamma P_0$ at the operating point m .

To show the uniform pulse generation over a wide bandwidth in dual-pump FOPA, Fig. 3.11(b) depicts the gain spectra of a typical dual-pump FOPA when both P_1 and P_2 are varying simultaneously and in Fig. 3.11(c) when either P_1 or P_2 is varied while the other one is fixed at $P_0/2$. The latter case which is studied in [60] is easier to implement as it requires only one modulated pump. The fiber parameters used in Fig. 3.11 are the same as in Fig. 3.8 with dispersion parameters $\beta_2 = -5.8 \times 10^{-31} \text{ s}^2\text{m}^{-1}$, $\beta_3 = 3.6 \times 10^{-41} \text{ s}^3\text{m}^{-1}$ and $\beta_4 = 5 \times 10^{-56} \text{ s}^4\text{m}^{-1}$ to achieve $m = -0.28$ and $\rho = 0.001$. All the spectra are calculated using FS model. It can be observed that for all cases, the gain is decreased considerably over the entire bandwidth when at least one pump is slightly decreased. In case both pumps power are reduced by 20%, Fig. 3.11 shows that the gain drops by more than 7 dB over 40 nm range between the two pumps. In [60] it was demonstrated that for Gaussian condition the FWHM of generated pulses is increased by $\sqrt{2}$ when only a single pump is modulated compared to the case of two simultaneous modulated pumps. Note that except for the region close to the pumps the gain behavior would be similar when either P_1 or P_2 is decreased in agreement with Eq. 3.20 which is obtained from TS model. As a result, modulating either of the pumps leads to generation

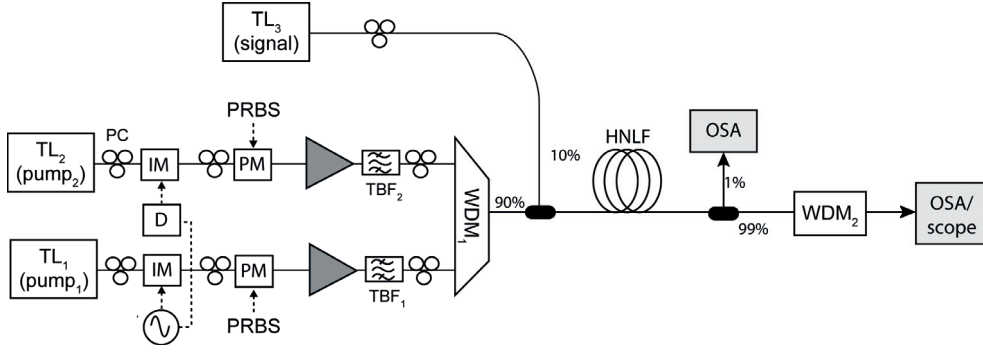


Figure 3.12 – Experimental setup for pulse generation in dual-pump FOPA. TL: tunable laser; IM: intensity modulator; PM: phase modulator; PC: polarization controller; TBF: tunable bandpass filter; WDM: wavelength division multiplexer; OSA: optical spectrum analyzer [59].

Table 3.2 – FOPA settings and parameters for the two experimental cases presented in Fig. 3.13. The normalized phase-mismatch term experiences high fluctuations in case 1 and low fluctuation in case 2.

	Pump 1	Pump 2	β_2 (s ² m ⁻¹)	m	$ \rho $	$2\Delta\omega_t/2\pi$
Case 1	1532.3 nm	1608.3 nm	-1.5×10^{-29}	0.35	0.55	Non applicable
Case 2	1532.3 nm	1607.2 nm	-5.8×10^{-31}	-0.28	0.001	4.9 THz

of the same pulses over the bandwidth where the TS model is valid. Although simultaneous modulation of two pumps is more complex to implement, generates shorter pulses compared to single-pump modulation.

3.3.2 Experiment

Figure 3.12 illustrates the experimental setup used to test the pulse generation in dual-pump FOPA theory. Two tunable CW lasers (TL₁ and TL₂) with OSNR>50 dB are used as the two pumps. The lasers are modulated in intensity by a sinusoidal wave at 5 GHz. A variable RF delay line is used to provide synchronous pumps. Both pumps are phase modulated by a 2.5 GHz PRBS to suppress the SBS. The delay of each PRBS source is set so that the phase jumps occur during the dip of the sinusoidal pumps [52]. The pumps are then amplified and filtered to eliminate the ASE and then coupled using a WDM filter. Another CW laser (TL₃) is used as the signal source and combined with the pumps through a 90/10 coupler. The three optical waves are launched into a HNLF with $L = 350$ m length, nonlinear coefficient $\gamma = 15$ W⁻¹km⁻¹ and ZDW $\lambda_0 = 1568.9$ nm. The dispersion slope and dispersion curvature of the fiber are $\beta_3 = 3.6 \times 10^{-41}$ s³m⁻¹ and $\beta_4 = 5 \times 10^{-56}$ s⁴m⁻¹, respectively. The signal power is kept low enough to avoid pump depletion and multiple FWM process. At the fiber output the parametric process is monitored using a 1% tap on an OSA. Finally, a WDM and a tunable filter separate the generated idler from other spectral components. The temporal and spectral characteristics of the idler pulses are then monitored on an OSA and a 50 GHz oscilloscope.

3.3. Investigation of Pulse Generation in Dual-Pump FOPA

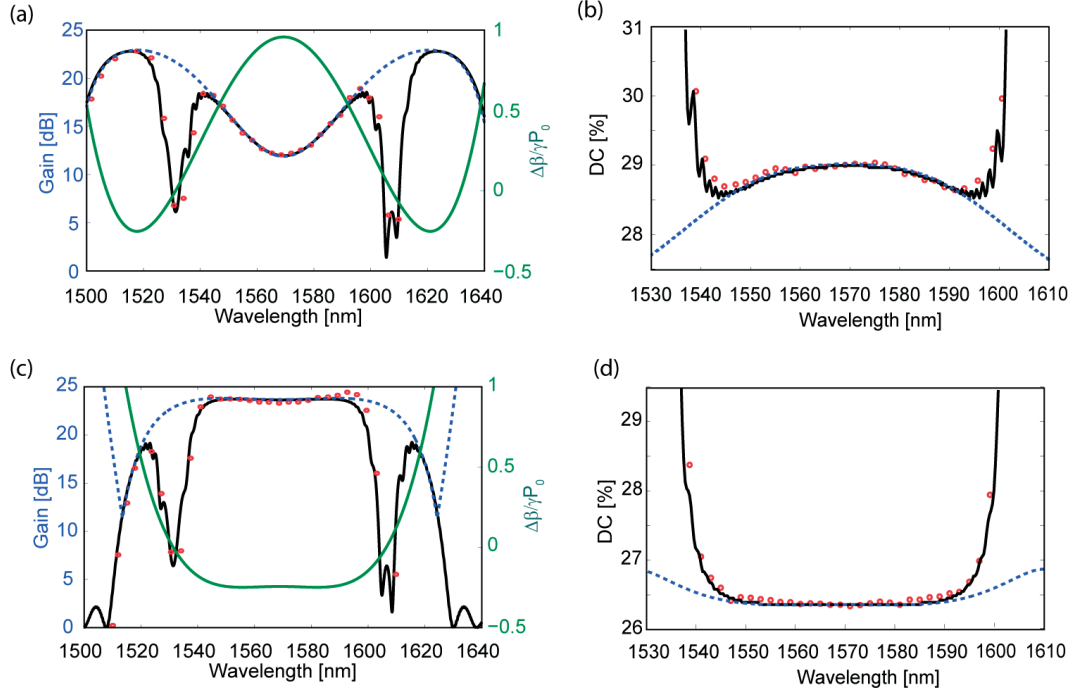


Figure 3.13 – Gain spectra and pulse width behavior in dual-pump FOPA for parameters in case 1 and case 2, denoted in Table 3.2. (a) and (c) experimental (dot) and theoretical gain spectrum obtained from TS (dashed line) and FS (solid line) interaction model along with normalized phase-mismatch for case 1 and 2 respectively. (b) and (d): experimental (dot) DC values as well as theoretical results derived from TS (dashed line) and FS (solid line) interaction model for case 1 and 2, respectively [59].

3.3.3 Results and Discussions

Two cases are experimentally investigated regarding different operating condition to verify the theory. In the first case we set $\lambda_1 = 1532.3$ nm and $\lambda_2 = 1608.3$ nm which leads to $\beta_2 = -1.5 \times 10^{-29} \text{s}^2 \text{m}^{-1}$ and corresponds to $m = 0.35$ with high ripple amplitude of $\rho = 0.55$. In the second case λ_2 is adjusted to provide a phase-matching that is bounded with minimum ripple. The wavelength of the second pump is set at $\lambda_2 = 1607.2$ nm for which the resulting dispersion $\beta_2 = -5.8 \times 10^{-31} \text{s}^2 \text{m}^{-1}$ leads to $m = -0.28$ and $\rho = 0.001$ over $2\Delta\omega_t/2\pi = 4.9$ THz. Table 3.2 summarizes the settings and parameters in two cases. Note that as higher ripple is tolerated in case 1, the bandwidth is also larger compared to the second case. Besides, due to the positive β_4 of the fiber used in the experiment, we were limited to the operating region of type (iii) for case 1 and type (i) for case 2.

Figures 3.13(a) and (c) depict the experimental and theoretical gain spectra together with the normalized phase-mismatch derived from the theory. The corresponding experimental DC measurements are plotted in Figs. 3.13(b) and (d). Both TS and FS interaction models are used to plot the data in all figures. Figures 3.13(a) and (b) demonstrate that in case 1, $\Delta\beta_L/\gamma P_0$ varies significantly between 0.45 and 0.95 over 54 nm range between the pumps leading to

1.72% fluctuations of the averaged duty cycle. In the second case shown in Figs. 3.13(c) and (d), low ripple of linear phase-mismatch is demonstrated over 40 nm wavelength range. Flat gain of 23 dB and flat linear phase-mismatch of $0.28\gamma P_0$ are obtained simultaneously. The DC measurement shows less than 0.04% variations over 40 nm range. For both cases the increase of DC in region close to the pumps which is correctly predicted by FS interaction model, is mainly due to sidebands generated in the outer band of the two pumps.

Figures 3.14(a) and (b) show the evolution of the experimental averaged pulse shape with idler wavelength for the two experimental cases. The peak power variation of the idler pulses follow the same trend as the gain spectrum. It can be verified from Figs. 3.14 and 3.13 that an identical pulse source in terms of DC and peak power is realized only when the phase-mismatch is bounded according to Eqs. 3.26. In Fig. 3.14(c) the idler pulses and the averaged profiles are demonstrated when $\Delta\beta_L/\gamma P_0 = 0.9$ corresponding to an idler wavelength at 1570 nm in case 1 as well as $\Delta\beta_L/\gamma P_0 = -0.28$ corresponding to an idler wavelength anywhere between 1548 nm and 1588 nm in case 2. The pulse width difference between these two cases is 5 ps, in agreement with theoretical predictions.

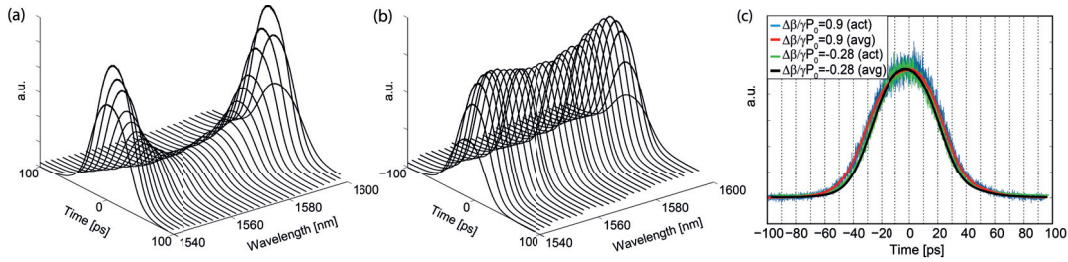


Figure 3.14 – (a) and (b) depict the evolution of averaged pulse shape with idler wavelength respectively regarding the first and the second phase-matching condition described in Table 3.2. (c) actual (act) and averaged (avg) pulse shape for $\Delta\beta_L/\gamma P_0 = 0.9$ in the first case and for $\Delta\beta_L/\gamma P_0 = -0.28$ in the second case [59].

3.3.4 Dissimilar Pump Modulation

As described in previous sections, modulating the FOPA pumps allows for creating a time window on signal and idler waves through gating the parametric gain. We verified in case of sinusoidal modulated pumps either for single or dual-pump FOPA, the time window duration is inversely proportional to repetition rate of the pump modulation. From a pulse generation point of view, this means the pulse duration and repetition rate are highly correlated, limiting the flexibility of the pulse source. In several applications of tunable optical pulses such as microscopy and spectroscopy, it is desired to make the duration and period of pulses independent, so that one is not necessarily scaled by changing the other.

In this section we investigate dissimilar modulation of the pumps in dual-pump FOPA. We show that by driving the two pumps with sinusoidal waves at different frequencies it is possible to increase the flexibility of the pulse source by de-coupling pulse duration and period to some

extend. In the following we will review the principle of this technique and then present the experimental results and discussion.

Principle of Operation

As explained in section 3.3.1, in a dual-pump FOPA with modulated pumps, a significant gain exists only at the time instances where the peak of the two pumps coincide in the time domain. Therefore, with sinusoidal modulated pumps at arbitrary frequencies f_1 and f_2 , the pulses are produced at a period that is the least common multiple (LCM) of $1/f_1$ and $1/f_2$. In case the LCM does not exist, the generated pulses are not periodic and cannot be employed in pulse generation applications. Otherwise, a pulse source can be realized which duration and period are partially de-coupled.

To clarify the operation of this source, assume that the two pumps are driven by sinusoidal waves at f_1 and f_2 ($f_2 > f_1$) with $\text{LCM}(f_1, f_2) = n$. In this case the fast modulation, f_2 mainly determines the pulse duration as it limits the overlapping time between the two pumps. Note that the pulse duration will also depend on f_1 ; however as mentioned in section 3.3.1, by varying f_1 in the range $[0, f_2]$ the maximum variation of pulse duration will be $\sqrt{2}$ times, i.e. the order of magnitude remains unchanged. On the other hand, the slower modulation frequency, f_1 defines the pulse period as an efficient gain is produced only at its peak positions. As a result, the repetition period of the pulse can be down rated n times without any substantial change in the pulse duration.

Results and Discussions

Figure 3.15 shows the simulated and experimental pulse waveforms for several values of (f_1, f_2) . The simulated results (Figs. 3.15(a)-(c)), include slow (solid line) and fast (dashed line) modulated pumps as well as idler pulses (dotted line). Fig. 3.15(a) corresponds to the similar pump modulation, $(f_1, f_2) = (10 \text{ GHz}, 10 \text{ GHz})$ leading to idler pulses of FWHM duration $\tau_{\text{FWHM}} = 19.5 \text{ ps}$ and period $T = 100 \text{ ps}$. By reducing f_1 to 5 GHz (Fig. 3.15(b)) and 2.5 GHz (Fig. 3.15(c)), the pulse period is respectively increased to $T = 200 \text{ ps}$ and $T = 400 \text{ ps}$, while the pulse duration changes only slightly. Figure 3.15(d) shows the corresponding experimental results for $(f_1, f_2) = (5 \text{ GHz}, 10 \text{ GHz})$ and $(f_1, f_2) = (2.5 \text{ GHz}, 10 \text{ GHz})$ are in a good accordance with simulated data.

Though reducing f_1 increases the pulse period, a major problem is the existing pedestals at the two sides of the pulse peak. These pedestals appear where the total power at the intersection of the pump waveforms becomes significant and they grow with decreasing f_1 . One way to lower the pedestals is to operate FOPA in higher sensitivity ($S_{P_0}^G$) condition. Indeed higher sensitivity correspond to a more intense drop of FOPA gain at lower powers, resulting in pedestals with reduced amplitude. Figure 3.16(a) demonstrates the idler pulses with modulation frequencies $(f_1, f_2) = (1 \text{ GHz}, 10 \text{ GHz})$ respectively at $\Delta\beta_L/\gamma P_0 = -1$ (solid line) and $\Delta\beta_L/\gamma P_0 = -3$ (dashed

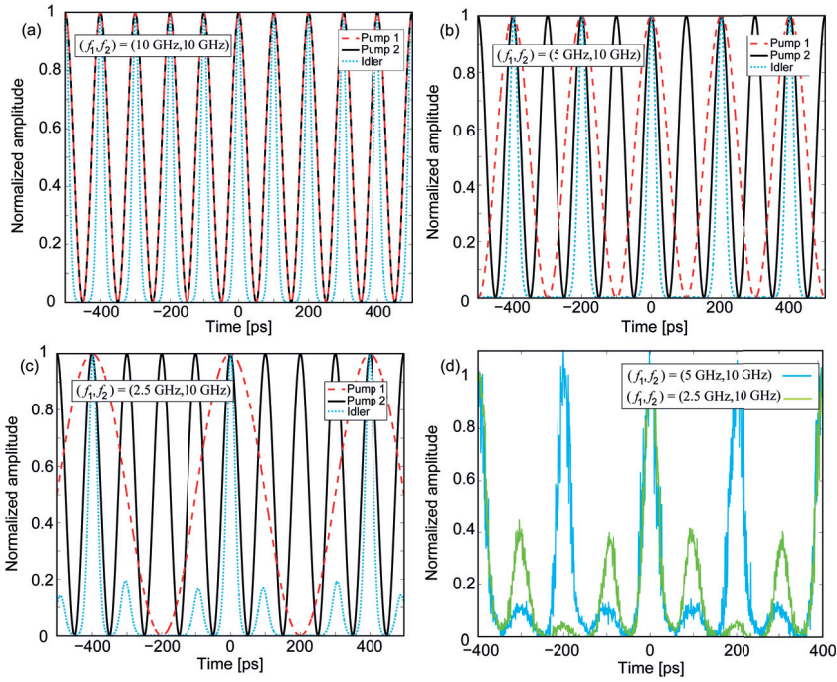


Figure 3.15 – Simulated pulse train of slow modulated pump (solid line), fast modulated pump (dashed line) and idler (dotted line) for (a) $(f_1, f_2) = (10 \text{ GHz}, 10 \text{ GHz})$, (b) $(f_1, f_2) = (5 \text{ GHz}, 10 \text{ GHz})$, $(f_1, f_2) = (2.5 \text{ GHz}, 10 \text{ GHz})$. Experimental idler pulses for $(f_1, f_2) = (5 \text{ GHz}, 10 \text{ GHz})$ and $(f_1, f_2) = (2.5 \text{ GHz}, 10 \text{ GHz})$.

line) phase-matching condition. From section 3.3.1 it is known that the latter condition has a higher sensitivity which leads to lower pedestals as shown.

Another technique to reduce the pedestals is to modify pumps modulation to shorten their width so that intersections take place at lower total power. Figure 3.16(b) shows the generated idlers at $(f_1, f_2) = (1 \text{ GHz}, 10 \text{ GHz})$ and $\Delta\beta_L/\gamma P_0 = -1$ condition. The pump modulation for lower frequency is modified by adjusting the bias voltage to create a pump with three equal frequency components corresponding to lower FWHM. It is seen the amplitude of pedestals is reduced in the case of modified pump modulation (dashed line) compared to normal modulation (solid line).

Note that pedestal suppression can be also implemented externally, using various thresholding techniques such as intensity discrimination in birefringent fibers [61] or nonlinear optical loop mirror [62].

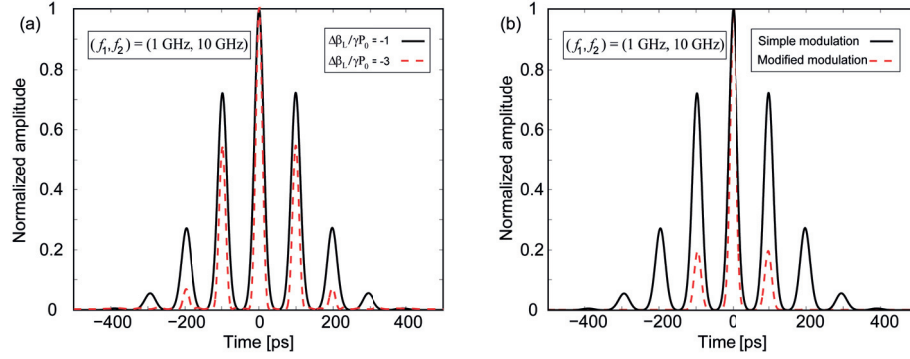


Figure 3.16 – (a) Generated idlers for $(f_1, f_2) = (1 \text{ GHz}, 10 \text{ GHz})$ at $\Delta\beta_L/\gamma P_0 = -1$ (solid line) and $\Delta\beta_L/\gamma P_0 = -3$ (dashed line) phase-matching condition. (b) Generated idler for $(f_1, f_2) = (1 \text{ GHz}, 10 \text{ GHz})$ and $\Delta\beta_L/\gamma P_0 = -1$ condition with normal pump modulation (solid line) and modified pump modulation (dashed line).

3.4 Discussion and Conclusion

In section 3.2 we verified the theory introduced in [52] by performing an experiment. Mathematically we proved that the generated pulses based on single-pump FOPA can be approximated Gaussian only for high g_0L and $\Delta\beta_L \leq -2\gamma P_0$. The experimental results show an excellent agreement with the theory. Particularly, we demonstrated all-optical near-sinc pulse generation at repetition rates as high as 40 GHz. The FWHM of the pulses at that repetition rate was measured at 3.5 ps which represents a compression factor of 7. Using numerical simulations we studied the effect of pump depletion and signal power on the generated pulses. We found a good agreement with the experimental results and showed that for any phase-matching condition the signal power can be optimized to obtain low noise pulses. Moreover, we studied walk-off and revealed that the generated pulses exhibit an asymmetry which is due to the dispersion slope and the pump time derivative.

The possibility to generate different pulse shapes, opens up the path for various applications in ultrafast all-optical signal processing. In particular for signals that are located at the edge of FOPA gain spectrum, it is possible to generate near-sinc pulses. The ability to generate a window in the time domain with a near-sinc shape response allows for the development of all-optical Nyquist-limited receivers and samplers. However, this regime is the most sensitive to the pump power fluctuations and to walk-off. To fully exploit the near-sinc pulses, the development of viable low-noise sinusoidal pumps or new architectures employing two dissimilar frequency pumps is necessary.

In section 3.3 we studied for the first time the theory of pulse generation in dual-pump FOPA. By introducing the gain sensitivity parameter we showed that the *DC* of generated pulses depends on total input power P_0 , fiber length L and linear phase-mismatch between the interacting waves. We obtained a general empirical formula for the *DC* of generated pulses. The gain sensitivity parameter could be used to investigate other properties of dual-pump

Chapter 3. Optical Short Pulse Generation Based on Parametric Amplification

FOPA such as pump relative intensity noise (RIN) transfer.

We also showed that it is possible to bound the linear phase-mismatch term in dual-pump FOPA over a large bandwidth to any value between $-3\gamma P_0$ and γP_0 to achieve a constant *DC* and peak power in that bandwidth. The theory is verified by an experiment that generates uniform pulses at 5 GHz repetition rate over 40 nm bandwidth with 0.04% fluctuations. The setup was limited to 50 GHz electrical bandwidth of the oscilloscope and can be extended to higher repetition rates. The good agreement between theoretical and experimental results shows that walk-off effect between the interaction waves is negligible. However for higher repetition rate of pumps, a dedicated study is required to understand how the pulse shape is affected. One way to reduce walk-off is to decrease the HNL length. In this case the pumps power have to be recalculated to achieve uniform operation over a wide bandwidth.

It worth noting that the amplitude of generated pulses exhibits a phase that is equal to $\beta_3 \Delta\omega_s^3 L/6 + \gamma P_0 \cos^2(\pi f_R t)L$ [42]. The latter expression shows that β_3 is the underlying term in producing walk-off [63], while $\gamma P_0 \cos^2(\pi f_R t)L$ which comes from the pump cross-phase modulation, induces a chirp on the generated pulses. Therefore, the pulses are not transform-limited. Note that similar to the single-pump FOPA, Gaussian pulses could be shortened by using a dispersive medium to reach a transform limited pulse. The SNR of produced pulses in the case of uniform pulse generation was measured at 27 dB. In this study we mostly focused on demonstrating uniform pulse generation over a wide bandwidth; yet by improving the pumps OSNR, using for example narrower filters and/or two-stage amplifying modules for the pumps, it is possible to further improve the pulse SNR [64, 65].

Finally, generation of pulses using dual-pump FOPA enables the possibility of modulating the two pumps independently. This unique flexibility can ease generating a broad variety of pulses and time window shapes. In [60], we demonstrated pulse generation in dual-pump FOPA by modulating only one of the two pumps. However, the corresponding pulse width is wider by a factor of $\sqrt{2}$ compared to the two synchronous modulated pumps. The possibility of modulating the pumps at different frequencies could also pave the way to realize a pulse source which width and repetition rate are independent. The proposed scheme can be also used to compress input signals in the time domain. Specifically for WDM pulses carrying data for subsequent optical time division multiplexing this scheme allows transparent connection of dissimilar rate networks.

4 All-Optical Signal Processing for WDM Networks

In this chapter we investigate dual-pump FOPA as a key enabling device for all-optical signal processing applications, in particular for WDM networks. We aim for two major functionalities in such networks; all-optical wavelength conversion and all-optical signal regeneration. We first study wavelength conversion problem for networks with dissimilar tributary speeds. We will show experimentally that by proper design of FOPA, simultaneous wavelength conversion and time compression of WDM channels is achievable. In the second application we study optical 3R regeneration for WDM channels. We provide theoretical design rules and experimental results showing simultaneous signal regeneration for WDM channels.

4.1 Introduction

With the immense growth of network traffic and with 10 Gb/s technology reaching maturity, service providers have already started installing new technologies aiming at 40 Gb/s and 100 Gb/s per wavelength [66]. According to the 50 GHz wavelength grid standard of international telecommunication union (ITU), the spectral range 1530 nm-1565 nm is divided into fixed 50 GHz spectrum slots. This rigid carrier frequency distribution is problematic for 100 Gb/s bit rates and beyond as they might not fit well into the existing slots. Even if sufficient spectrum is available, high data-rate signals become hard to transmit over long distances with high spectral efficiency. Therefore, it is beneficial to maximize the spectral efficiency by adapting the network conditions as well as the traffic demand.

To address this challenge, we require adaptive networks equipped with flexible transceivers and network elements which can adapt to actual traffic needs. Combining adaptive transceivers, flexible frequency grid and intelligent nodes enables a new *elastic* networking paradigm. In such networks electrical switching of the channels arriving at a single node becomes very costly and complicated due to the considerable degree of freedom in system configuration. Therefore, reconfigurable optical add-drop multiplexer (ROADM) is known as the ultimate solution to overcome this complication. A conventional ROADM should basically be able to perform add, drop and pass-through operations where switching is accomplished without

optical-electrical-optical (OEO) conversion. ROADM functionality originally appeared in long-haul dense wavelength division multiplexing (DWDM) systems. Routing through such network requires a single channel be converted to another wavelength at certain nodes. More importantly, the channel quality has to be constantly maintained through the links. Therefore, wavelength conversion (WC) and signal regeneration are two crucial functionalities in such networks.

These functionalities have been of great interests and subject to research studies for more than 20 years. However, one serious challenge in this regard is realizing a flexible all-optical device which is operational in a large wavelength range for parallel input channels. The next two sections are dedicated to present dual-pump FOPA as a device enabling signal processing of WDM channels.

4.2 Uniform Wavelength Conversion and Time Compression of WDM Channels

In essence, dual-pump FOPA satisfies key requirements of an excellent wavelength converter. This device provides broadband operating range, controlled inter-channel crosstalk and good conversion efficiency. Moreover, it is transparent to advanced modulation formats and can operate in polarization insensitive mode and high symbol rates [67–69]. In almost all previous studies on WC, continuous wave (CW) FOPA pumps seeds were employed. However, by exploiting pulsed pump operation regime, new flexibilities can be introduced in terms of pulse compression, adaptation to networks with various speed/granularity and also demultiplexing capabilities.

In this section we demonstrate a broadband uniform wavelength converter based on dual-pump FOPA with sinusoidal modulated pumps. In a theoretical analysis we study the pulse compression techniques for FOPA output in two steps. The first step is exploiting chirp compensation for generated idler and calculating maximum achievable compression factor after chirp compensation. In the second step we study pump modulation to achieve additional compression. Taking advantage of the high compression and uniform frequency response of the device, we demonstrate experimental results on simultaneous wavelength conversion and time compression of WDM channels. This is a key enabling feature for multi-granular networks where it is essential to change the bit rate transparently between dissimilar rate networks.

4.2.1 Theory

Maximum Compression Factor of Idler Pulses After Chirp Compensation

Consider a single-pump ($n = 1$) or dual-pump ($n = 2$) FOPA which pump(s) is (are) intensity modulated by a sinusoidal wave at frequency f_R . The pump(s) with total peak power P_0 is

4.2. Uniform Wavelength Conversion and Time Compression of WDM Channels

(are) launched into a fiber with nonlinear coefficient γ and length L . The general idler field in this case can be written as:

$$A_I(L, t) = \left(A_S(0) \frac{i\gamma P_0}{g} \sinh(gL) \right) e^{i(\phi_n(t) + \frac{\Delta\beta_L}{2}L)} \quad \phi_n = \left(\frac{n+1}{2} \gamma P(t)L \right) \quad n = 1, 2 \quad (4.1)$$

The gain coefficient $g^2 = (\gamma P_0)^2 - (\kappa/2)^2$ is a function of phase-matching $\kappa = n\gamma P_0 + \Delta\beta_L$ where $\Delta\beta_L$ is the linear phase-mismatch between the interacting waves and depends on the wave frequency and the fiber dispersion profile. $\phi_n(t)$ represents the induced chirp which originates from pump(s) cross-phase modulation. This chirp can be compensated using a first order dispersive medium and lead to pulse compression.

In pulse generation context it is always desirable to evaluate the pulse chirp and the amount of compression after chirp compensation. The studies regarding chirp analysis in FOPA are limited to the Gaussian condition where the chirp can be approximated linear [56]. Therefore, it is advantageous to evaluate maximum compression of the generated idler pulses in various operating condition of FOPA. To quantify compression limits after chirp compensation, we calculate maximum compression factor defined as $CF = T_1/T_0$, where T_1 is the pulse width after chirp compensation and T_0 is the pulse width at the FOPA output at $1/e$ width. Note that CF is equivalent to the broadening factor in pulse propagation literature within dispersive medium [25]. Taking into account the sinusoidal modulation of the pumps $P(t) = P_0 \cos^2(\pi f_R t)$, the chirp term would become:

$$\phi_n(t) = \alpha_n \gamma P_0 L \times \cos(2\pi f_R t) \quad \alpha_n = (n+1)/4 \quad n = 1, 2 \quad (4.2)$$

An important point which is not discussed in previous works is the sinusoidal term in Eq. 4.2 which leads to carrier linewidth broadening. Note that this broadening is analogous to the frequency modulation (FM) of RF signals where Bessel functions of the first kind are utilized to break the exponential term into an infinite sum of weighted carrier harmonic frequencies as [70]:

$$Ae^{i\omega t + i\beta \sin(\Omega t)} = Ae^{i\omega t} \left(J_0(\beta) + \sum_{k=1}^{\infty} J_k(\beta) e^{ik\Omega t} + \sum_{k=1}^{\infty} (-1)^k J_k(\beta) e^{-ik\Omega t} \right) \quad (4.3)$$

Comparing Eqs. 4.1 and 4.3, one can conclude that the sinusoidal phase in Eq. 4.2 produces higher harmonics and results in linewidth broadening. This broadening would influence CF through modifying the pulse width. Defining $V = 2\pi\delta f \times T_0$ where δf is the $1/e$ carrier half linewidth, analytical solution shows that T_1 is a function of V [71]. Moreover, it is shown that the pulse RMS width has a parabolic variation with distance of the propagation. The coefficients of the parabola are determined by using the differential operator \hat{H} and the commutator $[\hat{H}, t]$ which accounts for dispersive effects [72]. For an arbitrary symmetric pulse shape, CF is derived as $CF = [1 - b_1^2/(4b_0 \times b_2)]^{1/2}$, where b_i coefficients are obtained by

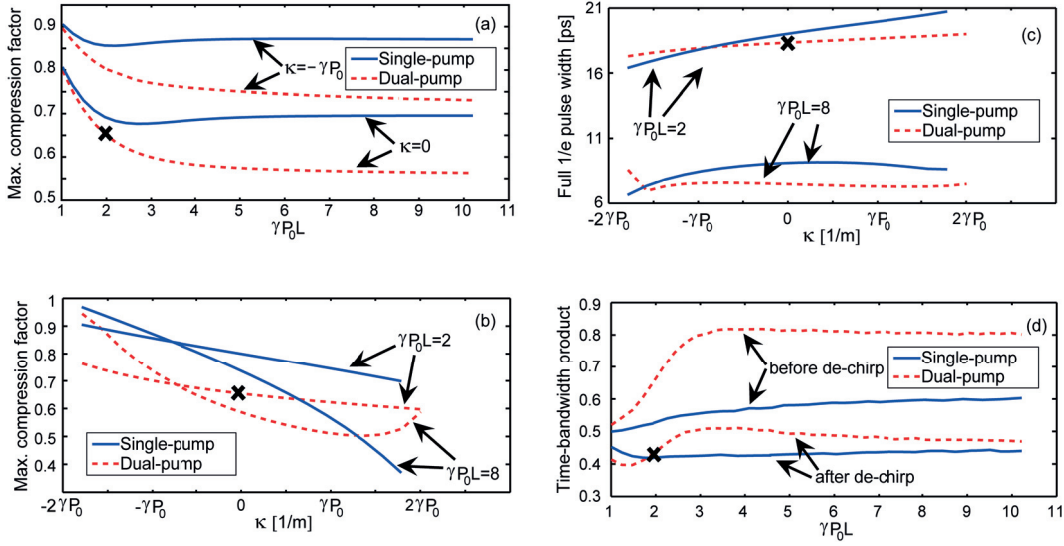


Figure 4.1 – Simulation: (a) CF at $\kappa = 0$ and $\kappa = -\gamma P_0$, (b) CF as a function of κ for $\gamma P_0 L = 2$ and $\gamma P_0 L = 8$, (c) $1/e$ pulse width after chirp compensation, (d) Time-bandwidth (TB) product before and after chirp compensation for $\kappa = 0$.

analytical integration as [72]:

$$b_0 = \int_{-\infty}^{\infty} \psi_0^*(\tau) \tau^2 \psi_0(\tau) d\tau \quad (a)$$

$$b_1 = i \int_{-\infty}^{\infty} \psi_0^*(\tau) [\hat{H}, \tau^2] \psi_0(\tau) d\tau \quad (b) \quad (4.4)$$

$$b_2 = -\frac{1}{2} \int_{-\infty}^{\infty} \psi_0^*(\tau) [\hat{H}, \tau^2]_2 \psi_0(\tau) d\tau \quad (c)$$

where $\psi_0(\tau)$ is the normalized field amplitude profile. Since Eqs. 4.4 take carrier linewidth and chirp into account, they can be used to obtain CF for idler pulses after chirp compensation for any arbitrary FOPA condition with no simplifying assumption.

To gain some insight, we investigate CF at various FOPA conditions for single and dual-pump FOPA schemes. Figure 4.1(a) depicts CF for $\kappa = -\gamma P_0$ and $\kappa = 0$ as a function of $\gamma P_0 L$. For all values of κ , an asymptotic behavior as a function of $\gamma P_0 L$ is observed. A physical insight may be given in the case with $\kappa = 0$, where the pulse shape is Gaussian [59]. In this case, the closed-form analytical formula of CF is [73]:

$$CF = \sqrt{\frac{1 + V^2}{1 + V^2 + C^2}} \quad (4.5)$$

where $C = -\frac{d^2\phi}{dt^2} \times T_0^2$ is defined as the chirp factor. Using Eq. 4.2, we derive the chirp factor as $C = -1$ in single-pump FOPA and $C = -3/2$ in dual-pump FOPA for any $\gamma P_0 L$. It can be shown that the behavior of V as a function of $\gamma P_0 L$ mainly depends on T_0 which tends to 0 as $\gamma P_0 L$ increases [52]. Hence, CF will asymptotically reach its minimum, $(1 + C^2)^{-1/2}$ with increase

4.2. Uniform Wavelength Conversion and Time Compression of WDM Channels

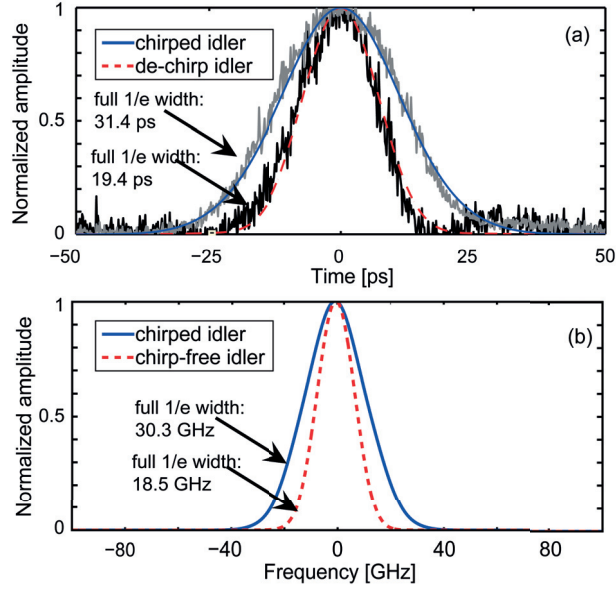


Figure 4.2 – (a) Experimental idler pulse shape at Gaussian condition before and after chirp compensation, (b) Calculated idler spectral envelope for chirped (solid line) and chirp-free (dashed line) pulses. The chirp-free idler is obtained by proper pre-chirping of the signal.

in pump power and/or fiber length and nonlinearity. The behavior of CF as a function of phase-matching (κ) is plotted in Fig. 4.1(b) for $\gamma P_0 L = 2$ and $\gamma P_0 L = 8$. It is noteworthy that the evolution of CF as a function of κ is inverse to that of T_0 in single and dual-pump FOPA [52, 59]. As a result, the chirp compensated pulse width T_1 (for a Gaussian chirped idler at 10 GHz), shown in Fig. 4.1(c) does not vary drastically as a function of κ . Transform-limited pulses are generated only after chirp compensation of Gaussian pulses that are obtained at $\kappa = 0$. Figure 4.1(d) shows the time-bandwidth (TB) product, defined at full-width half maximum (FWHM), before and after chirp compensation for $\kappa = 0$. Transform-limited form with FWHM temporal and spectral width product of $\Delta\nu \times \Delta\tau = 0.44$ is achieved near $\gamma P_0 L = 2$ (depicted by the cross).

To verify the theoretical results in Fig. 4.1 we performed an experiment using dual-pump FOPA where two pumps are intensity modulated by sinusoidal wave at $f_R = 10$ GHz. Pumps wavelength and power are selected to obtain $\kappa = 0$ and $\gamma P_0 L = 2$. This phase-matching condition corresponds to the Gaussian pulses [59]. Therefore after chirp compensation, transform-limited Gaussian pulse is generated. Thanks to the uniform phase-matching of dual-pump FOPA over a wide optical bandwidth, any pulse generated over that bandwidth will have similar characteristics. The experimental condition is reported in Fig. 4.1(a)-(d) by a cross sign. Figure 4.2(a) depicts an idler pulse (obtained by time-gating of a CW signal) before and after chirp compensation. CF is measured at approximately 0.62. To verify this result with theoretical value from Eq. 4.5, we need to calculate V and therefore δf . The linewidth broadening δf can be derived from Fig. 4.2(b) which depicts spectral envelope of the chirped and chirp-free pulse. These spectra are calculated by Fourier transform of Eq. 4.1.

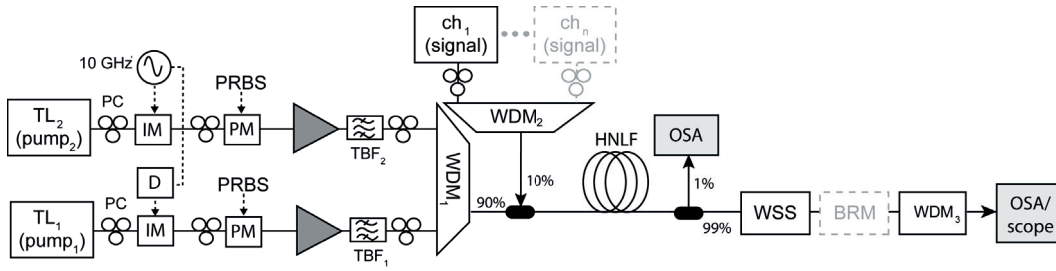


Figure 4.3 – Experimental setup for simultaneous wavelength conversion and time compression of WDM channels. TL: tunable laser; IM: intensity modulator; TBF: tunable bandpass filter; WDM: wavelength division multiplexer; OSA: optical spectrum analyzer; WSS: wavelength selective switch; BRM: bit rate multiplier [74].

The chirp-free spectrum is obtained by proper pre-chirping of the signal. Considering the half bandwidths at $1/e$, we obtain $\delta f = 5.9$ GHz. However, the actual δf in our experiment is $\delta f = 6.9$ GHz as phase modulation with effective half bandwidth of 1 GHz was applied on each pump to increase the Brillouin threshold. This leads to approximately $V = 0.68$, which together with $C = -3/2$ results in a theoretical CF of 0.63, in a very good agreement with the experiment.

Modifying FOPA Pumps Modulation

To enable further pulse compression, an extra adjustment can be made on FOPA pumps. In fact by setting the bias voltage of pumps intensity modulators, the initial sinusoidal modulation on each pump is modified by producing frequency sidebands which have equal amplitude with the DC component of the carrier. This is equivalent to modify the pump shape from $P(t) = P_0 \cos^2(2\pi f_R t)$ to $P(t) = P_0/9 \times \sin^2(3\pi f_R t) / \sin^2(\pi f_R t)$ leading to 60% decrease in FWHM of the pump pulse. Intuitively, the latter pump shape is the optimum shape in trade-off between pulse width and peak-to-first side lobe ratio, in such a way that the side lobes do not induce parametric gain. In the following experiment to achieve a high pulse compression, we first optimize the pumps modulation and then compensate the pulse chirp.

4.2.2 Experiment

To investigate uniform wavelength conversion and time compression of WDM channels, the experimental setup of a dual-pump FOPA shown in Fig. 4.3 is realized. Two tunable CW lasers (TL_1 and TL_2) are used as the two pumps. The pumps are intensity modulated by a 10 GHz sinusoidal wave. A tunable phase shifter is used to synchronize the peaks of the two pumps. Next the two waves are passed through a phase modulator driven by 2.5 GHz PRBS in order to suppress the SBS. The pumps are then amplified by EDFA and filtered by 1 nm filters to suppress the ASE. A WDM coupler combines the pumps and finally they are launched into a HNLF together with a tunable signal (TL_3) using a 90/10 coupler. The $L = 250$ m long

4.2. Uniform Wavelength Conversion and Time Compression of WDM Channels

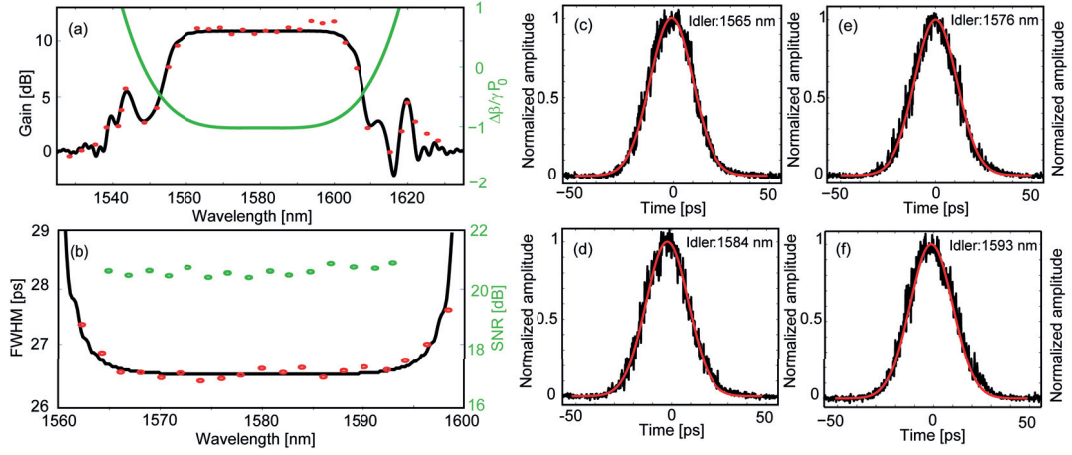


Figure 4.4 – (a) Experimental (dot) and theoretical (line) FOPA gain spectrum along with normalized phase-mismatch term $\Delta\beta_L/\gamma P_0$ (b) Experimental (dot) and theoretical (line) idler FWHM along with pulse SNR. (c)-(f) Experimental pulse shape (black) with theoretical Gaussian expression (red) [74].

HNLF has a nonlinear coefficient $\gamma = 12 \text{ W}^{-1}\text{km}^{-1}$ and zero dispersion wavelength (ZDW) $\lambda_0 = 1580.1 \text{ nm}$. The 3rd and 4th order dispersion parameters of the fiber are measured at $\beta_3 = 3 \times 10^{-41} \text{ s}^3\text{m}^{-1}$ and $\beta_4 = 3 \times 10^{-55} \text{ s}^4\text{m}^{-1}$ respectively. At the HNLF output a 99/01 tap is used to monitor the spectrum on an optical spectrum analyzer (OSA). Finally a WDM filter was used to separate the idler and monitor the temporal shape of the pulses on a 50 GHz oscilloscope. As mentioned in [59] with right settings for pump location and power, this device generates Gaussian pulses from a CW signal. This is equivalent to multiply the signal and idler by a Gaussian time window. Similar to the pulse generation, the time window has an inherent chirp which can be compensated by a tunable dispersive element leading to window compression. To investigate the WDM functionality of this device we coupled additional signals from a WDM bank to the setup. The time division multiplexing (TDM) functionality is then explored by using a bit rate multiplier (BRM) at the HNLF output. The BRM is in effect a time domain interleaver which splits the input stream into two legs. One leg is delayed relative to the second leg and then the two streams are recombined. The interleaved pulses therefore have an effective repetition rate multiplied by two times the input rate. By cascading several BRM stages, the rate can be further doubled.

4.2.3 Results and Discussions

For pumps located at $\lambda_1 = 1548.9 \text{ nm}$ and $\lambda_2 = 1612.7 \text{ nm}$ and $P_0 = 680 \text{ mW}$, the normalized phase-mismatch is bounded to $\Delta\beta_L/\gamma P_0 = -1$ over 32 nm, from 1564 nm to 1596 nm, with a uniform gain of 11 dB in good accordance with theory as shown in Fig. 4.4(a). The bias of the pumps modulators and the driving voltages were tuned so as to obtain high quality sinusoidal modulation with 170 mW average power on each pump ($= P_0/4$). The setup is first characterized for a single wavelength channel. The generated time window at different

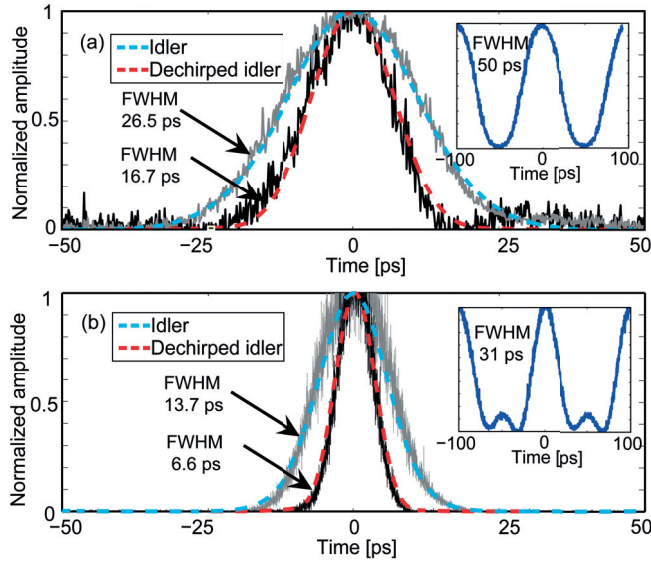


Figure 4.5 – (a) Pulse shape before and after chirp compensation with normal sinusoidal pump modulation, (b) Pulse shape before and after chirp compensation with equalized sideband pump modulation. The experimental data are fit with simulation results from SSF. The pump shape is shown in the inset for each plot [74].

wavelengths are depicted in Figs. 4.4(c)-(f). For all windows, an excellent match is obtained with Gaussian expression, showing that the time windows are identically Gaussian. Moreover, Fig. 4.4(b) shows that within the whole bounding region, the generated time window exhibits a FWHM of 26.6 ± 0.2 ps and SNR of 20.8 ± 0.3 dB, demonstrating the uniformity.

In order to compress the generated time window, a wavelength selective switch (WSS) device is used for chirp compensation. As mentioned in previous section the pulse chirp can be approximated linear with chirp factor $C = -3/2$, leading to 40% compression factor. Figure 4.5(a) shows the experimentally generated Gaussian window from sinusoidal pumps, before and after chirp compensation. Simulation results using SSF method are also included and show very good accordance with experiment. By modifying the bias voltage of the intensity modulators narrower pumps are produced which lead to 60% decrease in FWHM of the generated time window. Figure 4.5(b) shows that the window obtained in this case exhibits Gaussian shape with FWHM of 13.7 ps before chirp compensation and 6.6 ps after chirp compensation. The experimental shape and FWHM of pumps are shown in the inset. The FWHM TB product of the chirp compensated time window was verified to be 0.442 in both Figs. 4.5(a) and (b). Note that due to the FOPA uniform response, the Gaussian time window is multiplied to all CW signals similarly, generating identical Gaussian pulses at all converted wavelengths.

Owing to the high compression factor, the converted pulse sequence at FOPA output can be time multiplexed up to four times using a BRM. As a proof of concept an NRZ 10 Gb/s PRBS signal at 1595 nm is fed into the FOPA, with the pumps tuned as in Fig. 4.5(b). The generated idler at 1565 nm after chirp compensation is depicted in Fig. 4.6(a) showing a clear

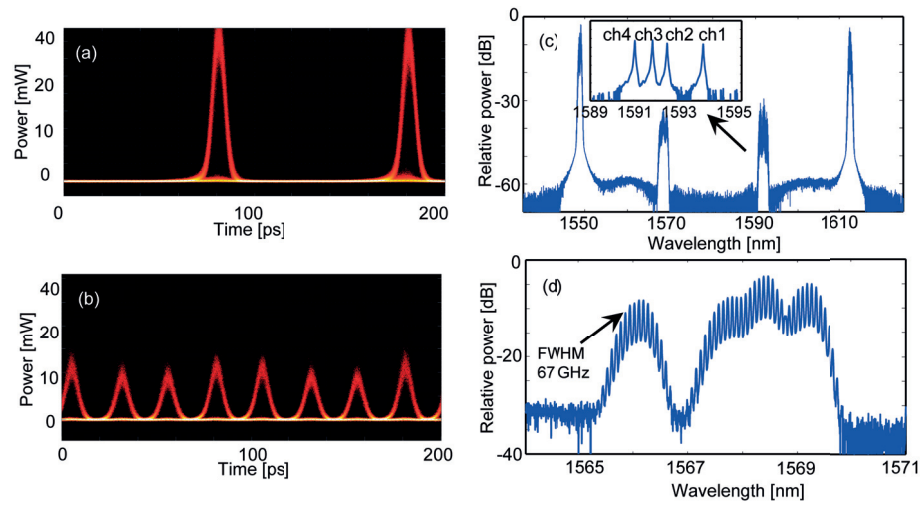


Figure 4.6 – (a) 10 Gb/s RZ trace of single wavelength signal after compression, (b) $\times 4$ multiplexed train of 10 Gb/s RZ pulses, (c) FOPA gain spectrum with modulated WDM band as input signal, (d) Magnified idler spectrum from the FOPA output spectrum [74].

open eye-diagram after compression. It is then multiplexed using the BRM by a factor of 4 to produce a 40 Gb/s signal which exhibits a clear open eye-diagram shown in Fig. 4.6(b). The traces in Fig. 4.6(a) and (b) are acquired using a C-band optical sampling oscilloscope with 500 GHz electrical bandwidth.

To investigate the uniform response of this device, a WDM laser bank with three channels at 100 GHz spacing and one at 200 GHz spacing was used as input signal. All channels were modulated by uncorrelated 10 Gb/s PRBS. The spectrum of the WDM signal is shown in the inset of Fig. 4.6(c). Figures. 4.6(c) and (d) show the FOPA output spectrum and the idler spectrum respectively after chirp compensation. The WDM signal is then multiplexed four times in time hence producing four WDM channels at 40 Gb/s bit rate. To check the performance of wavelength conversion and time compression, we filtered WDM channels using a 100 GHz (0.8 nm) bandpass filter. The eye-diagrams of each channel is shown in Figs. 4.7(a)-(d). Due to wavelength limitation of the optical sampling oscilloscope, the traces were acquired using the 50 GHz oscilloscope, which introduces some degradation to the observed eye-diagrams compared to Fig. 4.6(b). The slightly unequal amplitude of different TDM streams is due to the BRM response. The corresponding Q-factor of eye-diagrams in Fig. 4.7 is approximated 10 dB leading to error free operation of each 40 Gb/s RZ channel and as a result successful wavelength conversion and time compression of WDM channels.

4.3 3R Signal Regeneration

Regeneration of optical channels is an essential functionality in long haul links. As optical signals propagate in fiber, detrimental effects such as attenuation, dispersion, amplified spontaneous emission and nonlinearities degrade pulse quality. Consequently 3R regeneration

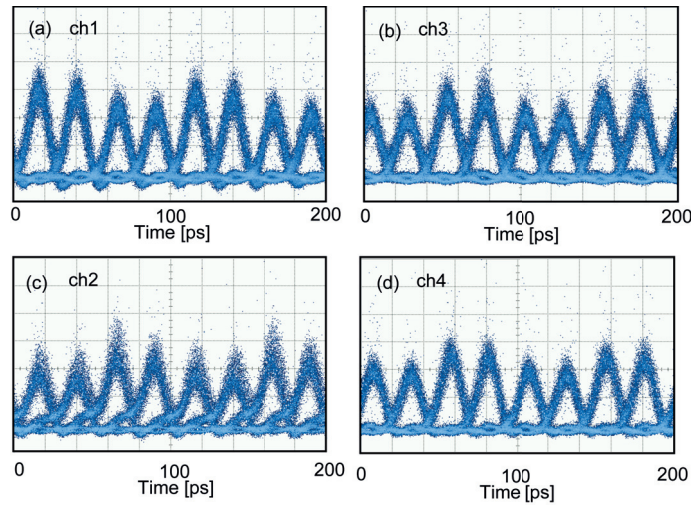


Figure 4.7 – (a)-(d) Eye-diagrams of frequency demultiplexed 40 Gb/s idler channels. The multiplexed channel is obtained by passing the compressed pulses through a bit rate multiplier (BRM) [74].

which consists of reamplification, reshaping and retiming is essential to retrieve the signal quality. Traditionally, 3R regeneration is performed by OEO conversion. This method takes advantage of forward error correction (FEC) coding to recover the corrupted data in digital domain. However, the limited speed of electronics and high cost of implementing OEO method for emerging multiplexing techniques, necessitate an all-optical solution.

Various all-optical regeneration methods have been studied such as SOA-based interferometers [75], EAM-based cross absorption modulators [76], injection locking laser diodes devices [77], four-wave mixing (FWM) [78] and optical parametric amplifiers (OPA) [79]. These techniques provide nonlinear transfer functions (TF) and synchronous pulse source to realize 3R regeneration. On the other hand, as the WDM technology is broadly used in current high speed systems and it represents the building blocks of future *flexi-grid* networks, WDM regeneration is of particular interest. However, the main challenges in WDM optical regeneration is to provide uniform performance in frequency and avoid crosstalk among channels.

To date, various techniques have been employed to implement WDM optical regeneration. One technique is to use space division multiplexing and then regenerate the channels that are separated in space [80]. This approach eliminates all interference effects but its complexity increases linearly with the number of channels. Another approach is to avoid inter-channel crosstalk by interleaving the WDM channels in time [81]. Therefore, during each specific time slot only one channel experiences regeneration which reduces the crosstalk. The precise time alignment in this scheme makes the number of channels limited by the duty-cycle of a single channel pulse. Another method is based on careful dispersion engineering which avoids inter-channel crosstalk through walk-off [82]. In this approach a high local average dispersion provides a fast walk-off between interacting WDM channels that substantially reduce the

crosstalk. However, a low overall dispersion value enables the basic nonlinear interaction that is required for regeneration. This scheme is hard to be scaled as the dispersion design depends on the number and wavelength of WDM channels. Bidirectional propagation and polarization multiplexing are two other methods used to reduce the inter-channel crosstalk [83]. However, scaling such systems to multiple WDM channels is highly challenging. To the best of our knowledge no simultaneous regeneration of more than four WDM channels has been demonstrated experimentally using the above mentioned techniques.

Among various regeneration methods, if the underlying nonlinear phenomenon is SPM such as for the Mamyshev regenerator [84], the technique is not applicable to any phase modulation format. As a result, techniques based on FWM are of particular interest because they preserve the phase information. Parametric regenerator based on saturation of parametric gain is one such attractive method as it can be applied to both intensity and phase modulated RZ signals [85, 86]. One technique for realizing a uniform WDM regeneration is to use dual-pump FOPA scheme. By setting the right dispersion parameters we have shown that this device provides a uniform phase-matching condition over a large bandwidth range between the two pumps which leads to a uniform flat gain in that range [59]. Therefore, operating in saturation regime enables a uniform 2R (reamplify and reshape) regeneration for WDM channels in FOPA operation range. In case the pumps are modulated in intensity, the FOPA gain is gated by a time window which has retiming property and provides a full 3R regeneration scheme [87].

In this section we show scalable optical 3R amplitude regeneration of WDM channels in dual-pump phase-insensitive (PI) FOPA with sinusoidal modulated pumps. Our proposed method can be employed in cascade with phase sensitive (PS) FOPA [88] to provide phase regeneration of quadrature modulation formats. We will show that this scheme is capable of simultaneous regeneration of five 10 Gb/s WDM channels, modulated with on-off keying (OOK) format. The number of channels was only limited by the available equipment and can in theory be increased.

Theory

As it was explained in chapter 2, in dual-pump FOPA if $\beta_2 \cdot \beta_4 < 0$ one can bound $\Delta\beta_L$ to a fixed value with low ripple over a wide wavelength range. This bounding is obtained by setting pump powers and wavelength for a given dispersive medium. Therefore, signals located within that bandwidth undergo uniform phase- matching and create idlers with similar characteristics in terms of phase and amplitude. When the pumps are intensity modulated, the FOPA gain is gated in time, creating a time window around signal and idler that is centered on the pumps peak. Because of the nonlinear properties of the medium, the time window is compressed compared to the pumps' repetition rate creating pulsed idlers and signals. In the previous chapter we showed that the shape and duty-cycle of the time window for synchronous and sinusoidal modulated pumps is uniform over the bounded phase-matching bandwidth and depends on normalized phase-mismatch term $\Delta\beta_L/\gamma P_0$ where P_0 is the total pumps peak power. In particular, when $\Delta\beta_L/\gamma P_0 = -1$, the idler power $P_I(t)$ for non-depleted pump regime

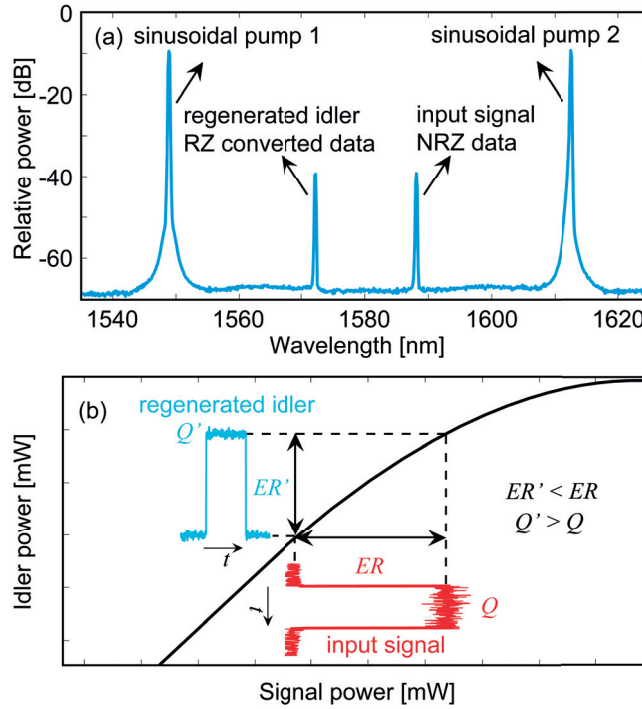


Figure 4.8 – (a) Typical experimental optical spectrum of dual-pump FOPA. FWM between two sinusoidal modulated pumps and the NRZ input signal, generates RZ idler data. (b) Illustration of a typical FOPA transfer function (TF). The saturation regime squeezes amplitude fluctuations and improves the pulse Q-factor.

is gated by a Gaussian time window given by [59]:

$$P_I(L, t) = \frac{1}{4} P_S(0, t) \exp(2\gamma P_0 L) \times \exp(-2\gamma P_0 L (\pi f_R t)^2) \quad (4.6)$$

where $P_S(t)$ is the idler power and f_R is the modulation frequency of the pumps.

Figure 4.8(a) shows the typical optical spectrum of dual-pump FOPA where the FWM between two sinusoidal modulated pumps and the NRZ input signal generates an RZ idler that is indeed the regenerated sample of the signal. Regenerative behavior of this scheme can be explained by the FOPA static TF. Figure 4.8(b) shows a FOPA typical TF which is an important criterion relating idler output power to the signal input power. For low signal power, the TF exhibits a linear behavior with the slope representing FOPA gain. By increasing signal power, pumps are depleted and therefore FOPA gain is reduced. This region is known as saturation regime and is used to squeeze the amplitude noise of the input signal [89]. The characteristics of TF together with the extinction ratio (ER) of the input signal, determine the operating range of the input to function in the saturation regime for regeneration purposes. For a fixed ER of the input signal, operating in saturation regime reduces the output ER. However, as illustrated in Fig. 4.8(b), saturation regime reduces the power fluctuations at mark's level, which enhances the Q-factor of regenerated data. This enhancement is shown to improve the bit-error rate (BER) of the

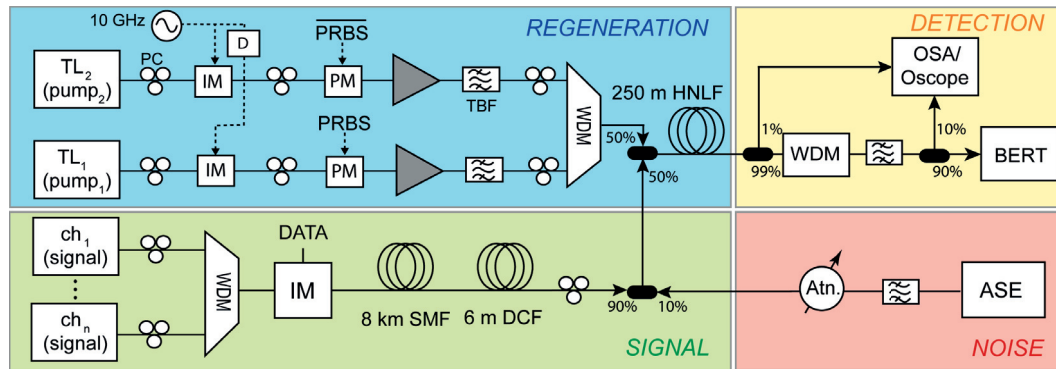


Figure 4.9 – Experimental setup for regeneration of WDM channels. TL: tunable laser; IM: intensity modulator; PM: phase modulator; PC: polarization controller; TBF: tunable bandpass filter; WDM: wavelength division multiplexer; Atn: attenuator; OSA: optical spectrum analyzer; BERT: bit-error rate tester.

input data for amplitude or phase modulated RZ signals [85, 86]. Additionally, with modulated pumps, data bits are re-aligned with the reference time window and hence the time jitter of the incoming sequence will be reduced to that of the time window. This provides the retiming property and fulfills the 3R regeneration functionality of dual-pump FOPA with sinusoidal modulated pumps. Thanks to the uniform phase-matching condition of the signal over a wide wavelength range, we demonstrate for the first time that this device can simultaneously regenerate several WDM channels. This effort can pave the way for scalable optical WDM regeneration by increasing channel count without changing the system complexity.

Experiment

Figure 4.9 represents the experimental setup for 3R optical regeneration which consists of four blocks. The signal block provides the WDM data channels. To characterize regeneration performance, the signal is intentionally degraded by noise. The combined signal and noise are then injected into the regeneration block. Finally the performance of regenerated channels is evaluated in detection block.

The regeneration block is in fact a dual-pump PI-FOPA with two tunable CW lasers (TL_1 and TL_2) that are modulated in intensity by a 10 GHz sinusoidal wave. The peaks of the pumps are synchronized using an electrical phase shifter. The pumps are then phase modulated by a 2.5 GHz PRBS to increase the SBS threshold. Later an EDFA and bandpass filter are used to amplify the pumps and eliminate the ASE. The pumps are then combined using a WDM coupler and launched into a HNLF together with signal using a 50/50 coupler. The fiber is characterized with the length $L = 250$ m, nonlinear coefficient $\gamma = 12 \text{ W}^{-1}\text{km}^{-1}$ and zero dispersion wavelength (ZDW) $\lambda_0 = 1580.1$ nm. The 3rd and 4th order dispersion parameters of the fiber are $\beta_3 = 3 \times 10^{-41} \text{ s}^3\text{m}^{-1}$ and $\beta_4 = 3^{-55} \text{ s}^4\text{m}^{-1}$ respectively. As mentioned in chapter 2, positive β_4 is the key to provide uniform time window over a wide wavelength range [59].

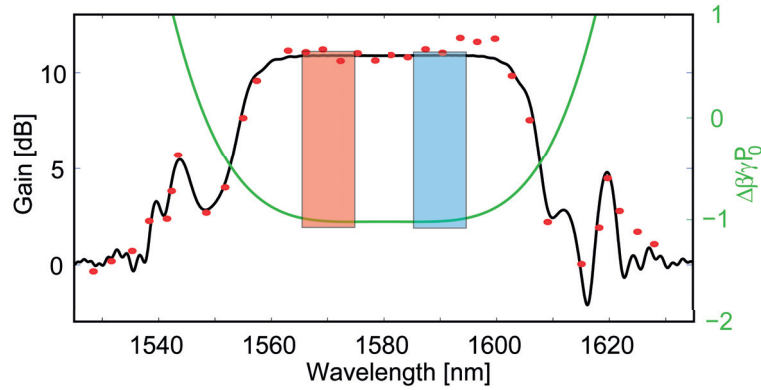


Figure 4.10 – (left axis) Experimental (red dot) and theoretical (black line) gain spectrum of dual-pump FOPA. (right axis) Theoretical normalized phase-mismatch term. Blue and red shaded wavelength spans represent signal and idler wavelength ranges, respectively.

The signal block is a L-band CW laser bank, with the lasers coupled through an arrayed waveguide grating (AWG). The combined channels are modulated by 10 Gb/s NRZ PRBS with $2^{31} - 1$ word length. An 8 km long SMF is used to decorrelate the data channels. An extra piece of dispersion compensated fiber (DCF) aligns the center of bit slots for all channels after SMF. This alignment is important for simultaneous regeneration of WDM channels and to evaluate the crosstalk effect among channels. Noise is combined with data using a 90/10 coupler. The noise block is an ASE source which leads to both amplitude and jitter noise. The OSNR of the degraded signal is adjusted by a tunable attenuator. A tunable bandpass filter is used to limit the noise bandwidth to only one channel. At the regenerator output the pumps are blocked by a WDM filter and the individual regenerated channels are selected by a 0.8 nm bandpass filter and detected by a 10 GHz detector. The performance of the regenerated channels is measured by a bit-error rate tester (BERT) device. The spectra and eye-diagrams of the detected signals are monitored on an oscilloscope and an OSA respectively.

4.3.1 Results and Discussions

Uniform Regeneration of Single Channel

We first adjust the FOPA parameters to obtain a wideband uniform gain which is essential for uniform operation of our device. The pumps wavelength are placed at $\lambda_1 = 1548.9$ nm and $\lambda_2 = 1612.7$ nm with total peak power of $P_0 = 680$ mW (170 mW of average power for each pump). Consequently the normalized phase-mismatch term is bounded to $\Delta\beta_L/\gamma P_0 = -1$ over 32 nm from 1564 nm to 1596 nm. As mentioned in chapter 2, this value of normalized phase-mismatch corresponds to the exponential gain regime which generates a time window with Gaussian intensity profile. Figure 4.10 shows the experimental gain spectrum (red dot) with 11 dB uniform gain in a good accordance with simulation results (black line). The normalized phase-mismatch derived from the simulation is also included in the plot. The WDM source we used in the experiment covers the blue shaded wavelength range within the phase-matching

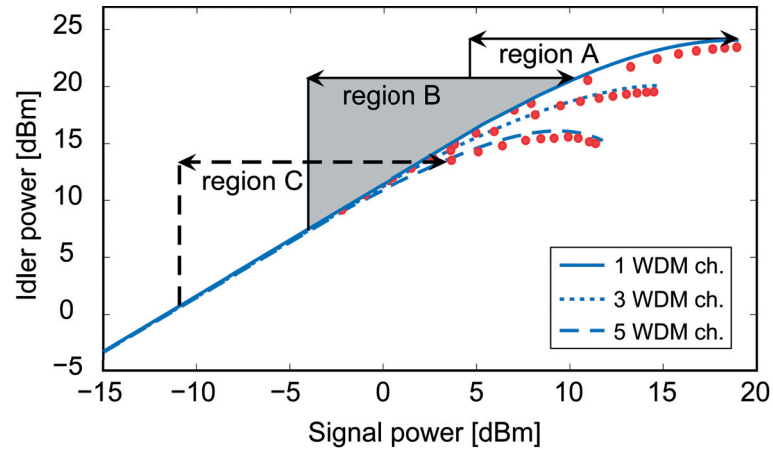


Figure 4.11 – Experimental (dot) and theoretical (line) transfer function (TF) of dual-pump FOPA when one, three, and five WDM channels present as the input signal.

interval with 300 GHz channel frequency spacing. Subsequently the corresponding idlers will be generated in the red shaded wavelength range. It is noteworthy that all simulation results are obtained by rigorous solution of the nonlinear Schrödinger equation (NLSE) using SSF method.

Figure 4.11 depicts the experimental and theoretical static TF in three different cases with one, three and five WDM channels present at the input of the regeneration block. The OOK modulator used in the experiment has a 14 dB ER, therefore the operating region of the regenerator can be shown by an arrow on the TF plot. In this subsection we investigate single-wavelength operation of the device thus we only discuss the single-channel TF by considering two different operating region. In region A, zero and mark levels are both placed in saturation regime which squeezes the noise for both levels. In region B, the zero level is located in linear gain regime while the mark level stays in saturated regime. Though squeezing the noise for both '0' and '1's seems to be more advantageous, it significantly reduces the ER from 14 dB to only 7 dB. Moreover, as operating in this regime requires higher average power the impact of the inter-channel crosstalk would be much higher in the forthcoming WDM operation (we will study the crosstalk in more detail in section 4.3.2). Given these conditions, operation in region B is preferred for the experimental demonstration.

To verify the regeneration property of the proposed device, BER measurements were performed for a single wavelength channel. The average power of input signal was set to 10 mW and its OSNR is degraded to three different values of 28 dB, 23 dB and 19 dB. The OSNR of non-degraded channel is better than 35 dB. Figure 4.12 shows the BER of a single-channel with respect to the average received power before and after regeneration. The back-to-back BERs before and after regeneration stage are also plotted in the same plot showing that the regenerator penalty is negligible. For all OSNR values the regenerated data have better BER compared to the degraded channels leading to 2 dB average gain in receiver sensitivity at 10^{-9} BER level.

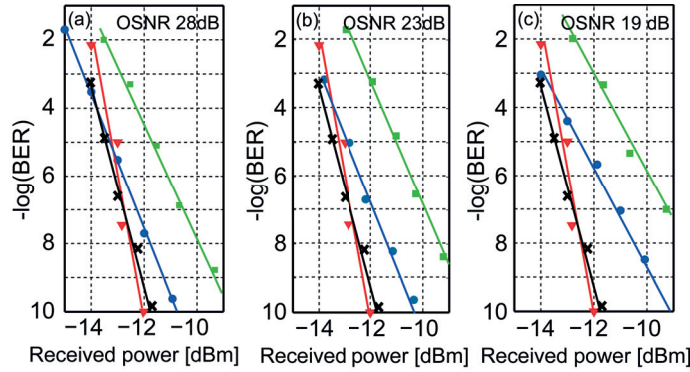


Figure 4.12 – BER measurement of single wavelength channel; back-to-back before regeneration stage (red triangle), back-to-back after regeneration stage (black cross), degraded (green square) and regenerated (blue circle) for three OSNR levels at (a) 28 dB, (b) 23 dB and (c) 19 dB.

Table 4.1 – RMS jitter of the optical eye-diagram before and after regeneration for three OSNR levels.

	SNR 28 dB	SNR 23 dB	SNR 19 dB
Before Reg.	3.6 ps	4.6 ps	9.1 ps
After Reg.	1.2 ps	1.4 ps	1.7 ps

Figure 4.13 depicts the optical (left column) and electrical (right column) eye-diagrams of the back-to-back channel (Fig. (a) and (b)), degraded channel with 23 dB OSNR (Fig. (c) and (d)) and regenerated channel (Fig. (e) and (f)). The ER of regenerated signal is reduced from 14 dB to 12 dB; yet the squeezed noise at mark's level enhances the BER. Note that with NRZ-OOK input signal, the regenerated channels turn into RZ-OOK pulses (FWHM of 26 ps) after regeneration.

Retiming capability of this block is verified by measuring the RMS jitter of the corresponding optical eye-diagram. Table 4.1 represents the RMS jitter of the pulses before and after regeneration for three different values of OSNR. It can be checked that while reducing OSNR degrades the pulse jitter, for regenerated signal the RMS jitter is fixed around 1.4 ps. This value mainly depends on the total jitter experienced by the generated time window which is governed by the jitter in RF signal used for pump modulation as well as the residual effects of pumps phase modulation.

Since the WDM source has five channels in the bounded phase-matching range 1587 nm-1596 nm with 300 GHz frequency spacing, the uniform operation of the regenerator is investigated by sweeping the wavelength of single channel over the entire range of interest. Figure 4.14 depicts the receiver sensitivity gain at 10^{-9} BER level after regeneration when the OSNR is degraded to 23 dB. It can be checked that sensitivity is improved over the measured range almost uniformly by 2 ± 0.3 dB. This uniform performance is expected over the entire range in which the normalized phase-mismatch is bounded to $\Delta\beta_L/\gamma P_0 = -1$.

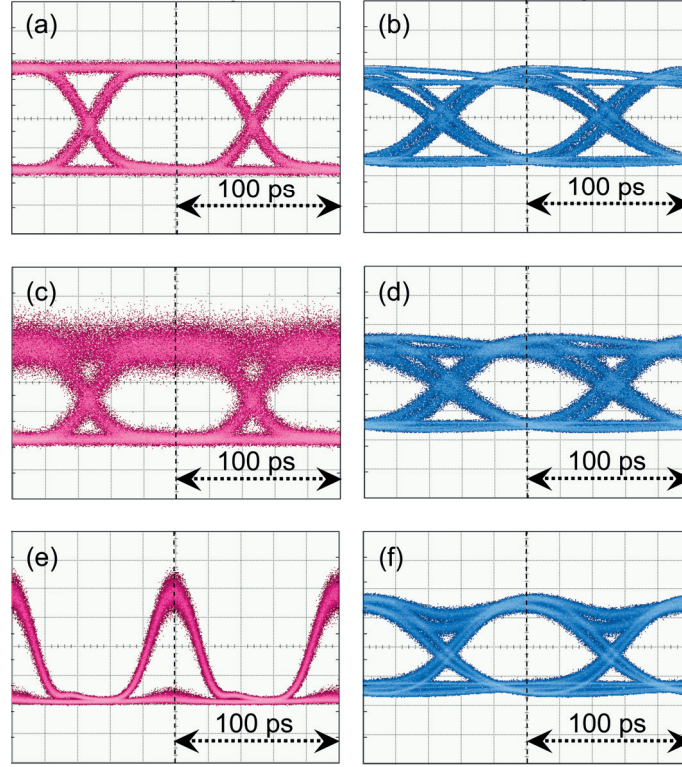


Figure 4.13 – Optical (left column) and electrical (right column) eye-diagrams of (a),(b) back-to-back channel, (c),(d) degraded channel with OSNR 23 dB and (e),(f) regenerated channel.

Simultaneous Regeneration of WDM Channels

A critical issue in moving from single-wavelength to multi-wavelength operation of regenerative devices is the inter-channel crosstalk. In principle, crosstalk originates from cross-gain modulation (XGM) and spurious FWM effect. XGM occurs for intensity modulated signals and leads to instantaneous change of pump power in the pump depletion regime depending on the number of signals that simultaneously transmit mark level. Spurious FWM is due to the interaction between any triplets of signal, idler and pump components. These interactions can become efficient and generate mixing products which fall on a channel or too close to it to be filtered out. Crosstalk effects are studied in section 4.3.2 but as a general rule the crosstalk power is proportional to the relative output signal power to the input pump power [42]. To obtain a better insight we quantified this ratio. Because of the energy conservation in parametric amplification, we can define the relative pump depletion (RPD) parameter as the sum of signals and idlers power over the pumps power as:

$$\text{RPD} = \frac{\sum_{m=1}^N (P_{S,m} + P_{I,m})}{P_0} \quad (4.7)$$

where $P_{S,m}$ and $P_{I,m}$ are the m th signal and idler power, respectively at the output of regeneration block and N is the number of signal channels. Using RPD one can approximate the ratio

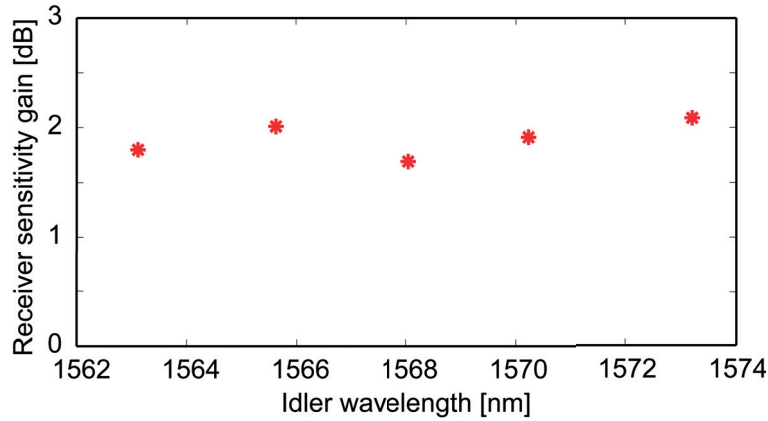


Figure 4.14 – Receiver sensitivity gain of individual channel after regeneration at BER level of 10^{-9} . The OSNR of each channel is degraded to 23 dB to check the regenerator performance.

of the pump photons that are converted to the signal and idler photons. Therefore, RPD can be employed to measure the pump depletion level [90]. To investigate simultaneous regeneration of multi-wavelength input, the corresponding TF should be exploited similar to the single-wavelength case to obtain the operating region of input signal power. Figure 4.11 illustrates that by increasing the number of input channels the required power for each channel to reach saturation regime is reduced. Our experiment was limited to maximum five WDM channels due to the limited equipments. Inspecting Eq. 4.7 shows that to maintain the same RPD value as in the single-wavelength case, the signal power should be reduced in the five WDM channel case. Assuming that close to the saturation regime, single and five input channels experience the same gain, it is required to reduce the power of signals by 7 dB. This operating region is marked with C on the five channel TF in Fig. 4.11. We checked the regeneration properties of this scheme by degrading the OSNR of the middle channel to 23 dB and measuring the BER of the regenerated middle channel in presence of all other channels in Fig. 4.15(a).

To illustrate the crosstalk effect, three different values of signal power, P_S are considered. For $P_S = 2$ mW which is 7 dB lower than the power in single channel case, the regenerated channel has a better performance compared to the degraded channel, showing successful regeneration. Increasing the signal average power to $P_S = 8$ mW and 20 mW degrades BER by introducing BER floors at 10^{-6} and 10^{-4} , respectively. Figures 4.15(b)-(d) show the corresponding optical eye-diagram of the regenerated channels. In Fig. 4.15(c), the increased noise at mark level is due to the spurious FWM whereas the multi-level eye-diagram in Fig. 4.15(d) reflects the XGM effect that imposes undesirable modulation on the detected signal.

Figure 4.16(a) shows the normalized idler spectrum for the mentioned cases. We switched off the middle channel to observe the amount of induced interference from FWM at this location. It can be seen that by increasing the input power, the interfering component grows rapidly. However, for the input power at $P_S = 2$ mW the spurious FWM/XGM is low enough to enable a successful regeneration of middle channel.

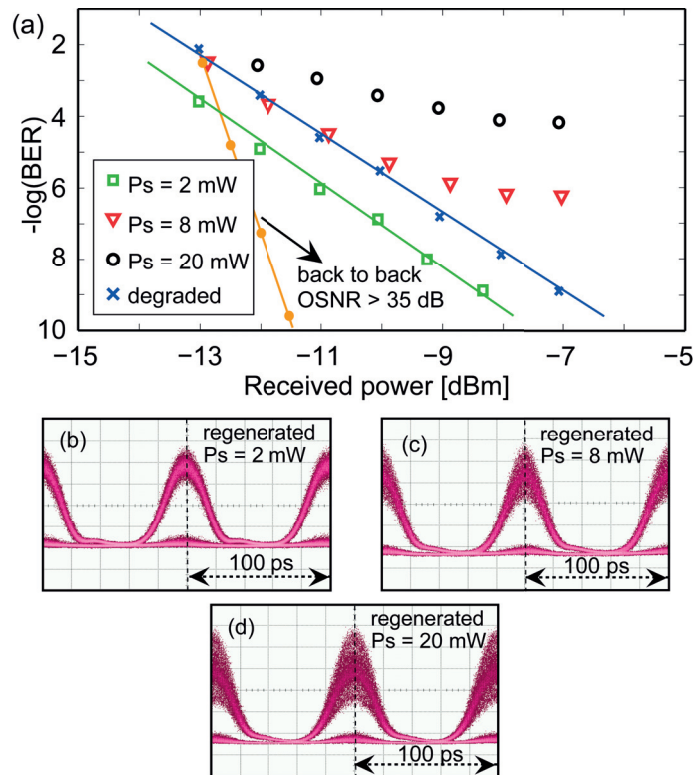


Figure 4.15 – (a) BER of the regenerated middle channel (in presence of other channels) at different values of input power when the OSNR is degraded to 23 dB. (b)-(e) Optical eye-diagram of regenerated middle channel with signal levels at 2 mW, 8 mW and 20 mW.

We measured the performance of simultaneous WDM regeneration in Fig. 4.17 by measuring the receiver sensitivity gain for each channel (in presence of other channels) at 10^{-9} BER level when the OSNR of the measured channel is degraded to 23 dB. For each channel the total enhancement level (blue bar) is split into two parts. The green bar represents the negative impact of inter-channel crosstalk. This value is obtained by subtracting the regenerated BER of single-wavelength and multi-wavelength input at OSNR level better than 35 dB. The red bar which shows the positive effect of the noise squeezing in regeneration block is measured by subtracting the blue and green bars. It can be checked that all channels experience gain sensitivity enhancement. Yet, it varies slightly across the channel number. In fact as the idler wavelength increases, the total BER enhancement is reduced. This reduction is mainly because of the growing inter-channel crosstalk which is higher for the wavelengths closer to the ZDW. This can be also seen in Fig. 4.16(b) which shows the optical spectrum after regeneration for $P_s = 2$ mW. Note that the red bars which only illustrate regeneration gain, have similar behavior as the one measured for single channel operation in Fig. 4.14.

An important requirement in simultaneous regeneration of WDM channels is the inline synchronization as employing a single time window mandates that all bits are synchronized with the inline modulation. This WDM synchronicity is obtained by proper delay lines within

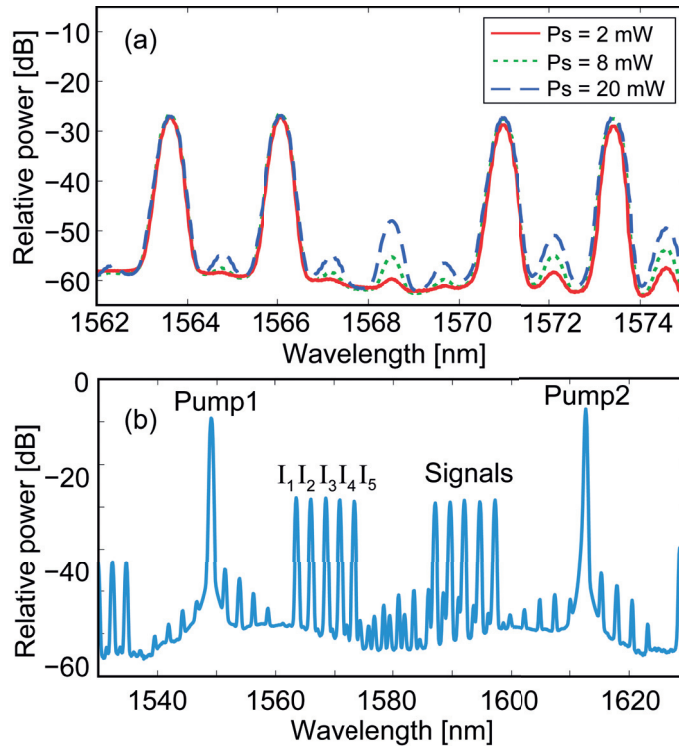


Figure 4.16 – (a) Normalized idler spectrum of three signal power levels. The middle channel is turned off to show the amount of spurious FWM. (b) Optical spectrum of dual-pump FOPA with five WDM channels as the input signal.

a demux/mux apparatus or by providing time-coincident WDM channels at specific location of the regenerator [81, 91]. In our experiment a 6 m long DCF was used before regeneration block to obtain bit synchronous operation. Figure 4.18 shows the regeneration sensitivity to this synchronicity by depicting BER versus time detuning between the NRZ data and the peak of the sampling window. We considered three cases, single and multi-wavelength operation with OSNR level better than 35 dB and multi-wavelength operation with 23 dB OSNR. In all cases the measured BER is constant over 60 ps detuning range, or 60% of the bit slot. This range corresponds to the duration of a mark level in the 10 Gb/s NRZ modulation, excluding the 40 ps rise/fall time. The time detuning of the five channels after DCF with respect to a fixed reference is limited to ± 8 ps. Therefore, in this experiment if the maximum detuning between any WDM channel is less than 44 ps, all WDM channels experience regeneration without penalty. Clearly as the data rate increases, simultaneous regeneration requires more precise synchronization.

4.3.2 Crosstalk Effects

In previous sections we successfully showed simultaneous 3R WDM regeneration. Here we elaborate the practical issues of this technique specially as the number of WDM channels

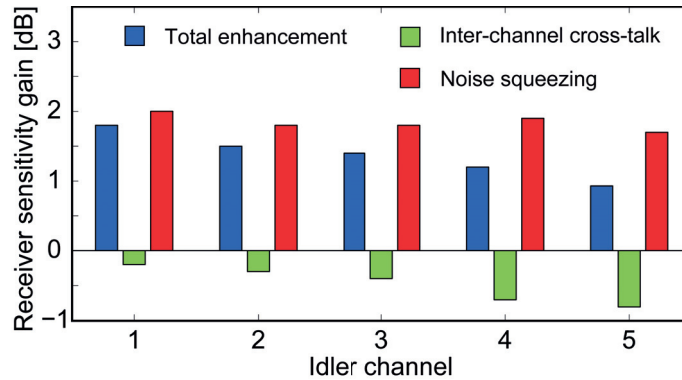


Figure 4.17 – Receiver sensitivity gain of each channel (in presence of other channels) at 10^{-9} BER level when the OSNR is degraded to 23 dB.

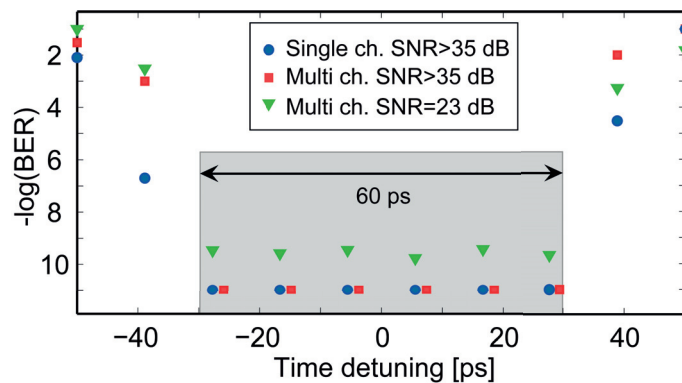


Figure 4.18 – BER versus time detuning of the regeneration time window. Three cases are considered; single (blue circle) and multi-channel (red square) operation with OSNR level better than 35 dB and multi-channel (green triangle) operation with 23 dB OSNR level.

increases. As mentioned before, there are two main sources of interference. The first is spurious FWM which is due to the interaction between signals, idlers and pumps. Among all possible combinations, pump-signal and signal-signal interaction are more probable to produce FWM components that interfere with the regenerated channel [90]. The pump-signal interference can be avoided by slight detuning of the pump wavelength such that the interfering components are generated between WDM channels and could in theory be filtered out. However, the interfering effect coming from signal-signal interaction can degrade the performance of regenerated channel in any WDM scheme with equally frequency-spaced channels. It is shown that an interference with even a few percent of channel power leads to 1 dB fluctuation in received power leading to non-negligible penalty [91].

It is known that the power ratio of the spurious component to the specific channel is proportional to ηP_R^2 where η is the efficiency of spurious FWM and P_R is the power of regenerated channel (assuming all channels have similar power) [45, 91]. The efficiency coefficient, η is essentially determined by the linear phase-mismatch term, $\Delta\beta_L$. As a result, once the channels

get closer to the ZDW or the channel frequency-spacing is reduced, spurious FWM components will become larger [92]. Also increasing the number of channels enhances η as new FWM terms are produced. However, the interference does not grow linearly with the channel count as efficient FWM takes place only over a limited bandwidth [45]. This bandwidth can be reduced to obtain a better performance by dispersion management techniques. In our method, the modulated pumps produce RZ pulses at the regeneration stage with either RZ or NRZ input data format. RZ pulses are resistive to the FWM interference as the interaction time between pulses is significantly reduced. Moreover, if the regeneration block induces enough walk-off between signals, the efficiency of FWM process will be further reduced.

On the other hand, by reducing P_R the spurious FWM power will be scaled down effectively. Yet, the regeneration technique requires a minimum signal peak power to maintain the operation in saturation regime. One way to reduce P_R without affecting saturation is to employ a dummy signal, for example at the center of the gain region to clamp the FOPA gain. This method which is widely studied in EDFA systems [93], reduces the saturation gain level so that signals undergo squeezing at lower input power. Note that P_R cannot be reduced arbitrary since the low input OSNR will not be improved by the regeneration block.

The second source of crosstalk is XGM. The time dependent gain induces a modulation on the regenerated channels which behaves as an interfering component. To estimate how system parameters affect XGM, we obtain an upper bound for the gain variations, ΔG . Starting with the exponential gain expression $|G| = \exp(2\gamma P_0 L)/4$, gain fluctuations in terms of pump power variations would be $|G| = \Delta P_0(\gamma LG)/2$. Maximum fluctuations of pump power corresponds to the condition where all signal channels convey zero level while in the next bit slot they convey mark level. Therefore, referring to Eq. 4.7, the upper bound on gain variations $|\Delta G_U|$ is obtained as:

$$|\Delta G_U| = \text{RPD} \frac{\gamma P_0 L G}{2} \quad (4.8)$$

Equation 4.8 shows that contrary to the spurious FWM, XGM is a function of FOPA gain. Moreover, it shows by increasing the number of channels for a fixed value of $\gamma P_0 L$, maximum gain fluctuations remain at the same level as long as we re-adjust the range of input signal power to maintain the RPD and gain level. One efficient way to confront XGM issue is to use differential phase shift keying (DPSK) modulation [94]. In this modulation format data are carried on the phase of optical signal leading to pulses with fixed intensity. Crosstalk reduction using DPSK has been shown to improve receiver sensitivity up to 2.4 dB compared to OOK modulation format [95].

4.4 Discussion and Conclusion

In section 4.2 we investigated simultaneous wavelength conversion and time compression of WDM channels. For that we studied pulse compression techniques in dual-pump FOPA.

One technique is based on modifying the pump modulation to achieve pumps with lower FWHM compared to the sinusoidal pumps. We next performed a detailed analysis of chirp compensation on the generated pulses and derived the maximum compression factor for arbitrary FOPA operating condition. In particular, we showed that the linewidth broadening due to the sinusoidal chirp term is a limiting factor in reaching high compression factors.

Combining the two mentioned methods, a total compression factor of 4.7 is obtained for the Gaussian pulses at FOPA output. Taking advantage of this factor and the uniform response of dual-pump FOPA over a wide wavelength range, we demonstrated simultaneous wavelength conversion and time compression of 10 Gb/s WDM channels. The high compression factor allowed for 4 time TDM of each WDM channel. This device can be utilized in multi-granular networks where transparent connection of dissimilar rate WDM networks is required.

In section 4.3 we exploited dual-pump FOPA for optical regeneration of WDM channels. We leveraged FOPA saturation regime where the noise squeezing property improves the Q-factor of noisy pulses which provides reshaping property. Moreover, by modulating the intensity of FOPA pumps the corresponding gain is gated by a time window which provides retiming property. With reamplifying, reshaping and retiming capability, this device can be used as 3R regenerator.

Taking advantage of the uniform response of dual-pump FOPA, regeneration of parallel WDM channels becomes possible. We present design rules to confront the crosstalk effect in multi-wavelength operation, most notably spurious four-wave mixing and cross gain modulation. We employed this device for regenerating five WDM channels which are modulated with 10 Gb/s NRZ data. Our technique improves the scalability of multi-wavelength regeneration by increasing channel count without changing the complexity of the device.

5 Generation of Nyquist Pulses and Detection of WDM-Nyquist Superchannels

In this chapter we study all-optical techniques for generating Nyquist pulses and therefore Nyquist superchannels. One technique is based on optical parametric amplification where by adjusting phase matching condition, near-sinc pulse shapes are produced. The other method is based on Mach-Zehnder modulator in which we generate high quality Nyquist pulses by direct synthesis of a rectangular frequency comb. Moreover, we present an all-optical demultiplexing technique for WDM-Nyquist superchannels by implementing the concept of matched filter receiver.

5.1 Introduction

In current high speed optical networks, WDM technology is widely employed to enhance the capacity of optical fibers. However, with the constant growth of data rates, new techniques need to be developed to provide the required bandwidth. These approaches are mostly focused on increasing the spectral efficiency of optical links. Exploiting multilevel modulation formats and polarization multiplexing can increase the spectral efficiency from 0.8 to several $\text{bits}^{-1}\text{Hz}^{-1}$ [4, 5]. However, these techniques drastically increase the complexity of electrical signal processing and have higher energy consumption.

Another possibility is to combine several low rate channels with high spectral efficiency into Tbit/s superchannels which can be routed as a single entity through optical networks. Such aggregation can be obtained both in frequency or time domain [6, 7]. In orthogonal frequency division multiplexing (OFDM), a superchannel is made of several subcarriers with sinc-shaped spectrum and can therefore be spaced at the baud rate without interchannel interference. By employing OFDM, a data rate of 26 Tbit/s and a total spectral efficiency of $5 \text{ bits}^{-1}\text{Hz}^{-1}$ has been demonstrated [96]. Similarly, in Nyquist transmission, data symbols are conveyed by Nyquist pulses [8] which overlap in time domain without inter-symbol interference (ISI). In a recent experiment a 32.5 Tbits/s WDM-Nyquist transmission with a net spectral efficiency

Chapter 5. Generation of Nyquist Pulses and Detection of WDM-Nyquist Superchannels

of $6.4 \text{ bits}^{-1}\text{Hz}^{-1}$ has been shown [9]. Compared to the OFDM, Nyquist superchannel has several unique benefits as it reduces the complexity of receiver [19, 97], it is more resistant to fiber nonlinearities [97], requires much lower receiver bandwidth [98] and leads to lower peak-to-average power ratios [18]

Nyquist channels can be multiplexed in time with overlap, referred to as *orthogonal time division multiplexing* (O-TDM) [20, 99]. In such systems the Nyquist pulse sequence is divided into N tributaries that are delayed and modulated to transfer the corresponding data. This scheme requires N modulators where N is the number of time-domain channels. Yet, compared to the direct modulation, the baud rate of each modulator is reduced N times. This considerably reduces the complexity of the modulators and the required electronics. Additionally, time-domain tributaries can be multiplexed at different wavelengths referred to as *WDM-Nyquist* transmission [6].

Nyquist pulses with high quality were initially produced using an arbitrary waveform generator that was offline programmed to create Nyquist filtering of the baseband signal [18]. The quality of such pulses tightly depends on the speed and resolution of digital-to-analog converters [7]. Therefore, with increased symbol rate beyond 40 Gbaud and the limited speed of electronics, the quality of Nyquist pulses generated by this method degrades significantly. Therefore, several all-optical Nyquist pulse generation techniques have been exploited. These techniques generally start from a mode-locked laser (MLL) and modify the spectrum by pulse shaping or filtering methods. In [20] a liquid crystal spatial light modulator is used to shape the Gaussian pulse train from MLL into raised-cosine Nyquist pulses. Optical parametric amplification with parabolic pumps is another technique for generating sinc-shaped Nyquist pulses [21]. Such techniques in general lead to a low quality Nyquist pulses while require complicated setups and costly equipment [19].

Through this chapter, in section 5.2 we study near-sinc Nyquist pulse generation by parametric amplification. In section 5.3 we present a different technique based on Mach-Zehnder modulator (MZM) to generate high quality Nyquist pulses. We will experimentally demonstrate that the latter method is very flexible in terms of adjusting pulse width and repetition rate. In section 5.4 we investigate a real-time demultiplexing scheme for WDM-Nyquist superchannels. This all-optical method is based on matched filter receiver and can perform simultaneous demultiplexing in frequency and time domain.

5.2 All-Optical Nyquist Pulse Generation by Parametric Amplification

Recent works [52, 57] have shown in theory and experiment that sinc-shaped Nyquist pulses can be produced by fiber optical parametric amplifiers (FOPA) in a cavity-less configuration. In this scheme an intensity-modulated pump which is coupled with a CW signal inside a HNLF, produces an idler pulse which is compressed compared to the pump and reshaped to a sinc

5.2. All-Optical Nyquist Pulse Generation by Parametric Amplification

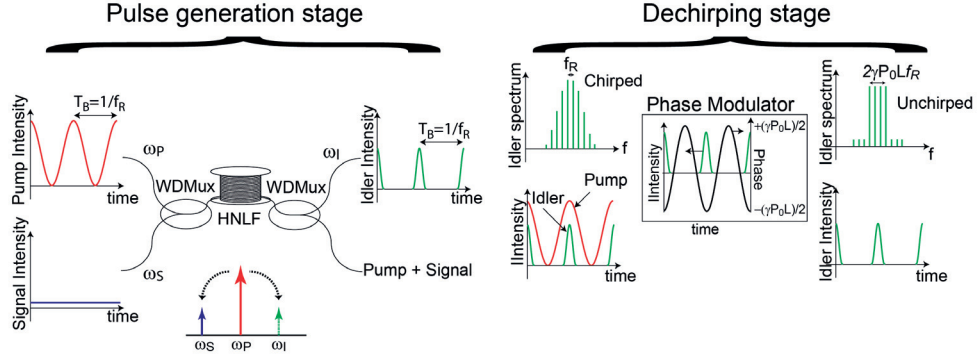


Figure 5.1 – Principle of generating near-sinc Nyquist pulses with single-pump FOPA and a subsequent phase modulator for chirp compensation. WDMux: wavelength division multiplexer [21].

function. However, during this process the pump induces a chirp to the idler which leads to spectral broadening and therefore a distortion. Since this chirp is not linear it cannot be compensated by passing through a dispersive medium; rather an active chirp compensation scheme is required.

In this section we study the theory of sinc-pulse generation and chirp compensation in single-pump FOPA. Accordingly, we present experimental results as a proof of concept.

5.2.1 Theory

Generation of Nyquist Pulses Using a Sinusoidal Pump

Figure 5.1 illustrates the principle of near-sinc Nyquist pulse generation in single-pump FOPA. A high power pump at angular frequency ω_P is coupled with a signal at ω_S and launched into a fiber. Through four-wave mixing (FWM) process, an idler wave is generated at ω_I that is symmetrical with respect to ω_P such that $\omega_S - \omega_P = \omega_P - \omega_I = \Delta\omega_S$. Assuming that the pump is intensity-modulated by a sinusoidal wave, pump field can be written as $A_P(0, t) = \sqrt{P_0} \cos(\pi f_R t)$, where P_0 is the pump peak power and f_R is the pump repetition rate. Due to the underlying Kerr effect, the generated idler is compressed compared to the pump modulation and the corresponding pulse shape and width would depend on the linear phase-mismatch, $\Delta\beta_L$ between the interacting waves. In particular when:

$$\Delta\beta_L = \beta_2 \Delta\omega_S^2 + \frac{\beta_4}{12} \Delta\omega_S^4 = -4\gamma P_0 \quad (5.1)$$

where β_2 and β_4 are the fiber dispersion and dispersion curvature, the idler amplitude, $A_I(\tau)$ at FOPA output would be [57]:

$$A_I(\tau) \approx i \left(\sqrt{P_0} \gamma P_0 L \right) \text{sinc}(2\pi\gamma P_0 L f_R \tau) \times e^{i \left(\gamma P_0 \cos^2(\pi f_R \tau) + \frac{\beta_3}{6} \Delta\omega_S^3 \right) L} \quad (5.2)$$

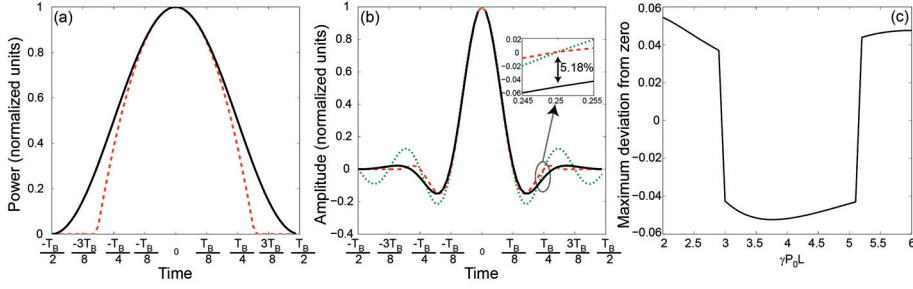


Figure 5.2 – (a) Sinusoidal pump (solid line) and parabolic pump (dashed line), (b) Generated idler by sinusoidal pump (solid line), by a parabolic pump (dashed line) and sinc-shaped pulse (dotted line). (c) Maximum amplitude of idler at Nyquist pulse zeros. T_B corresponds to one bit duration ($T_B = 1/f_R$) [21].

with γ being the nonlinear coefficient of the fiber and β_3 the fiber dispersion slope. Equation 5.2 reveals that the pump induces a chirp to the generated idler. This chirp spreads the pulse spectrum which affects the performance of WDM-Nyquist transmission. Note that as the chirp term can be expanded to $\cos^2(\pi f_R \tau) = (1 + \cos(2\pi f_R \tau))/2$, it can be compensated by a phase modulator driven by RF synthesizer at f_R . The principle of operation is depicted in Fig.5.1. Before the phase modulator, the generated idler at FOPA output is chirped and hence its spectrum is spread. Therefore, by driving the phase modulator with $\frac{\gamma P_0 L}{2} \cos(2\pi f_R t)$, the pump induced chirp can be suppressed completely by aligning the pulse peak with that of the driving sinusoidal wave. For the ideal chirp compensation the idler spectrum should be a rectangle of $2\gamma P_0 L f_R$ width.

Comparison Between Sinusoidal and Parabolic Pumping

In deriving Eq. 5.2, it was assumed that $P_P(0, t) \approx P_0 (1 - (\pi f_R t)^2)$ in the vicinity of the pump peak power [57]. We discuss the validity of this approximation in the following and show that using a parabolic pump the approximation becomes accurate. The parabolic pulse which have been demonstrated recently [100] can be written as:

$$P_P(0, t) = \begin{cases} P_0 (1 - (\pi f_R (t - N))^2) & t \in [-1/(\pi f_R), 1/(\pi f_R)] + N/(\pi f_R) \\ 0 & t \notin [-1/(\pi f_R), 1/(\pi f_R)] + N/(\pi f_R) \end{cases} \quad N \in \mathbb{Z} \quad (5.3)$$

Figure 5.2(a) illustrates the parabolic pump shape as well as the corresponding sinusoidal pump. Using Eq. 5.3 the idler expression can be written without approximation as:

$$A_i(\tau) = \begin{cases} i\sqrt{P_S}\gamma P_0 L (1 - (\pi f_R t)^2) \text{sinc}(2\pi\gamma P_0 L f_R \tau) \times e^{i(\gamma P_0 (1 - (\pi f_R t)^2) + \frac{\beta_3}{6} \Delta\omega_S)L} & t \in [-1/(\pi f_R), 1/(\pi f_R)] \\ 0 & t \notin [-1/(\pi f_R), 1/(\pi f_R)] \end{cases} \quad (5.4)$$

5.2. All-Optical Nyquist Pulse Generation by Parametric Amplification

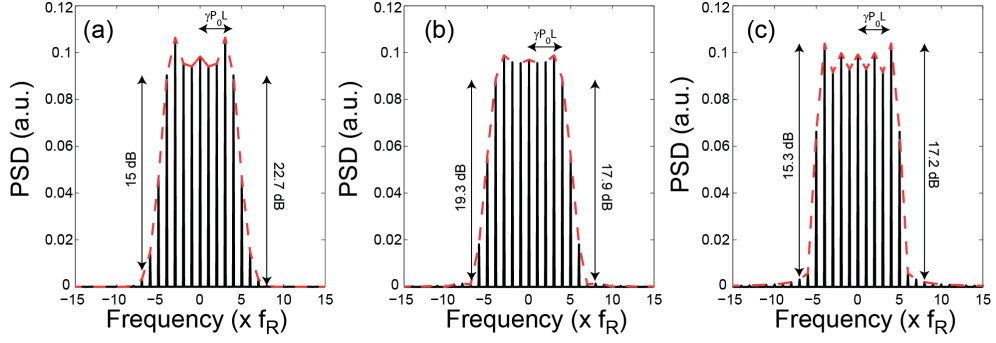


Figure 5.3 – Optical spectrum of the generated idler at $\gamma P_0 L = 4$ by (a) sinusoidal pump, (b) parabolic pump (c) sinc pulse [21].

Equation 5.4 is confined to the time interval $[-1/f_R, 1/f_R]$ without loss of generality. This equation clearly shows that although the generated idler by parabolic pump is not a perfect sinc, it remains a Nyquist pulse in the time domain. In [52] it was shown that for $\gamma P_0 L > 2$, the sinc function is a good approximation of the pulse shape. The idler pulse shape for sinusoidal (solid line) and parabolic pumping (dashed line) are depicted in Fig. 5.2(b) for $\gamma P_0 L = 4$ which corresponds to a peak gain of 12.3 dB at signal location. The theoretical sinc pulse (dotted line) is plotted as well for comparison. In all three envelopes the main lobes fit well with each other. In particular, the position of nearest zeros to the pulses peak are similar (at $t = \pm T_B/8$). However, the pulse generated by sinusoidal pump does not cross the zero ordinate at $t = \pm T_B/4$ and $t = \pm 3T_B/8$ which are zero positions of a Nyquist pulse. The maximum deviation from zero at these points is less than 5.2% which leads to an inter-symbol crosstalk lower than -12.8 dB for O-TDM scheme. Figure 5.2(c) shows the maximum deviation at Nyquist pulse zero positions as a function of $\gamma P_0 L$ for a pulse generated by sinusoidal pump. We measured the maximum inter-symbol crosstalk below -12.6 dB (5.45%).

Equation 5.4 also shows that a gating occurs in the time domain for generated pulses with parabolic pump. This leads, after chirp compensation, to an aliasing of the spectrum in frequency domain. To investigate the aliasing on the chirp compensated spectrum, we calculated the spectra of the chirp compensated pulses for sinusoidal and parabolic pumps at $\gamma P_0 L = 4$. The results are shown in Figs. 5.3(a) and (b). The spectrum of the theoretical sinc pulse is also shown in Fig. 5.3(c) for comparison. It can be seen that after chirp compensation, all spectra become contained to a bandwidth close to $2f_R\gamma P_0 L$. For Nyquist pulses, this bandwidth corresponds to two times of the Nyquist frequency. However, the power distribution of the spectral components are not equal. Moreover, the spectral component which remain out of the theoretical Nyquist pulse bandwidth can lead to interference in WDM-Nyquist transmission systems. This property exists due to the fact that pulses are generated over a finite time that is inferior or equal to bit duration. To show this aliasing effect, the spectrum of one pulse which is obtained by gating one pulse bit duration is depicted by dashed line in Fig. 5.3. These spectra are in fact the envelopes of the pulse train spectra which clearly demonstrate the aliasing effect. Therefore, WDM guard-band is required to avoid inter-channel cross talk in WDM-Nyquist

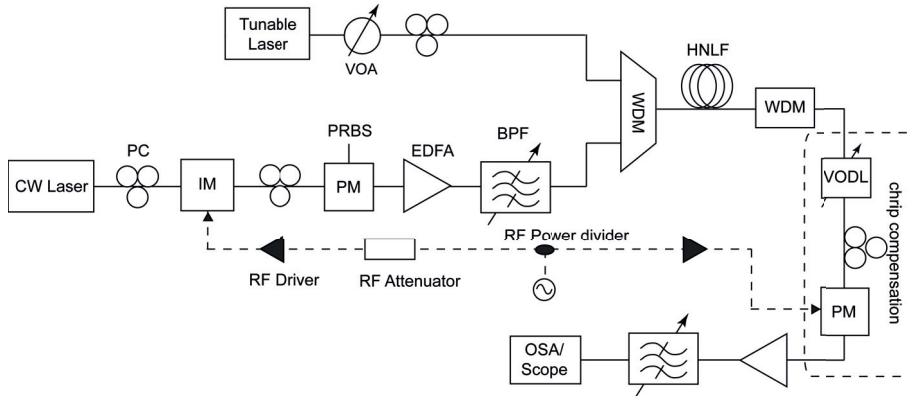


Figure 5.4 – Experimental setup for chirp compensation of near-sinc pulses. PC: polarization controller; EDFA: Erbium doped fiber amplifier; BPF: bandpass filter; PM: phase modulator; IM: intensity modulator; OSA: optical spectrum analyzer [21].

systems. For example Fig. 5.3 shows that for $\gamma P_0 L = 4$, the inter-channel crosstalk remains below -17 dB if the channels have a guard-band of $f_R \gamma P_0 L$, which corresponds to the Nyquist frequency. Note that pulses that are produced by sinusoidal pump, exhibit a lower crosstalk, below -22 dB. The crosstalk remains below -15 dB for a guard-band of $f_R (\gamma P_0 L - 1)$.

For sinc pulses generated in the electrical domain, the aliasing effect can be suppressed by extensive digital signal processing [7]. Yet, the pulses are limited by the electrical bandwidth.

5.2.2 Experiment

Figure 5.4 shows the experimental setup for generating near-sinc pulses in a single-pump FOPA. A CW laser is used as the pump which is intensity modulated by a 10 GHz sinusoidal wave and subsequently phase modulated by a 10 GHz PRBS to suppress the stimulated Brillouin backscattering. The pump is then amplified by an EDFA and passed through a 2 nm width filter to suppress the ASE. A tunable external cavity laser is used as the signal which power can be tuned by a variable optical attenuator. Pump and signal are coupled by a WDM and injected into a 500 m long HNLF. At the fiber output the generated idler is separated by a WDM filter and subsequently phase modulated by the same sinusoidal wave used to drive the intensity modulator. RF attenuators are employed to adjust the peak-to-peak voltages of the driving signals to guarantee that the pump intensity modulation is in the linear regime while the idler phase swings between $\pm \gamma P_0 L / 2$. A tunable optical delay line aligns the idler pulses with the peak of sinusoidal wave.

Before acquiring the pulse shape, the idler is amplified with an EDFA and filtered in order to reach the power threshold of the 500 GHz optical sampling scope. The spectrum is also monitored by an OSA with 0.02 nm resolution. This corresponds to 2.5 GHz resolution which is sufficient to observe the 10 GHz spaced spectral components.

5.2. All-Optical Nyquist Pulse Generation by Parametric Amplification

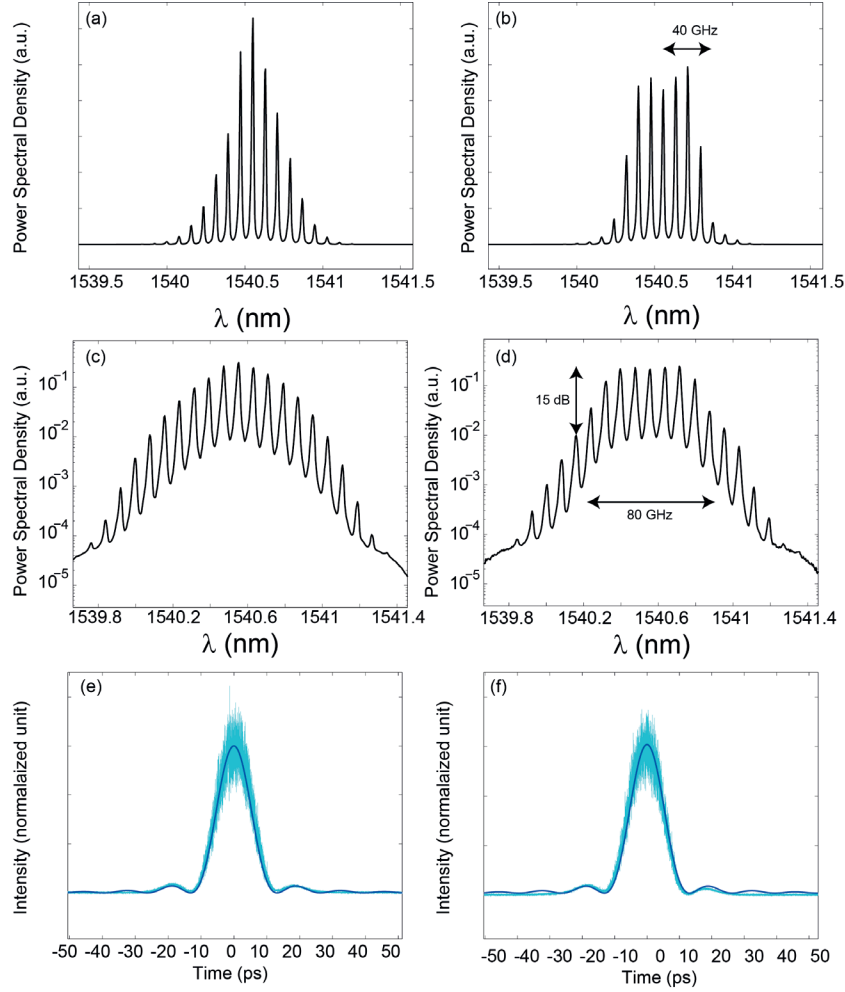


Figure 5.5 – Idler spectrum (a) before chirp compensation, (b) after chirp compensation, (c) before chirp compensation (dB scale), (d) after chirp compensation (dB scale). Idler pulse trace (e) before chirp compensation and (f) after chirp compensation [21].

5.2.3 Results and Discussions

The pump wavelength in the experiment is set to $\lambda_P = 1556.1$ nm. The HNLFF is characterized by nonlinear coefficient $\gamma = 12 \text{ W}^{-1}\text{km}^{-1}$, zero dispersion wavelength (ZDW) $\lambda_0 = 1551$ nm and absorption coefficient of $\alpha_{\text{dB}} = 0.85$ dB/km. We set the pump peak power to $P_0 = 700$ mW to obtain $\gamma P_0 L_{\text{eff}} = 4$ where L_{eff} is the fiber effective length. The signal was located at $\lambda_S = 1571.8$ nm, corresponding to the edge of FOPA gain spectrum.

Figures 5.5(a)-(d) show that the spectrum becomes square-shaped after chirp compensation where most of the energy is contained in an 80 GHz bandwidth, corresponding to two times of Nyquist frequency. We also measured the crosstalk of adjacent channel is less than -15 dB. Referring to Eq. 5.2, we expect a near-sinc pulse of 25 ps where the width is defined as the distance between two first zeros. Note that this corresponds to a FWHM of 14 ps. Figures 5.5(e)

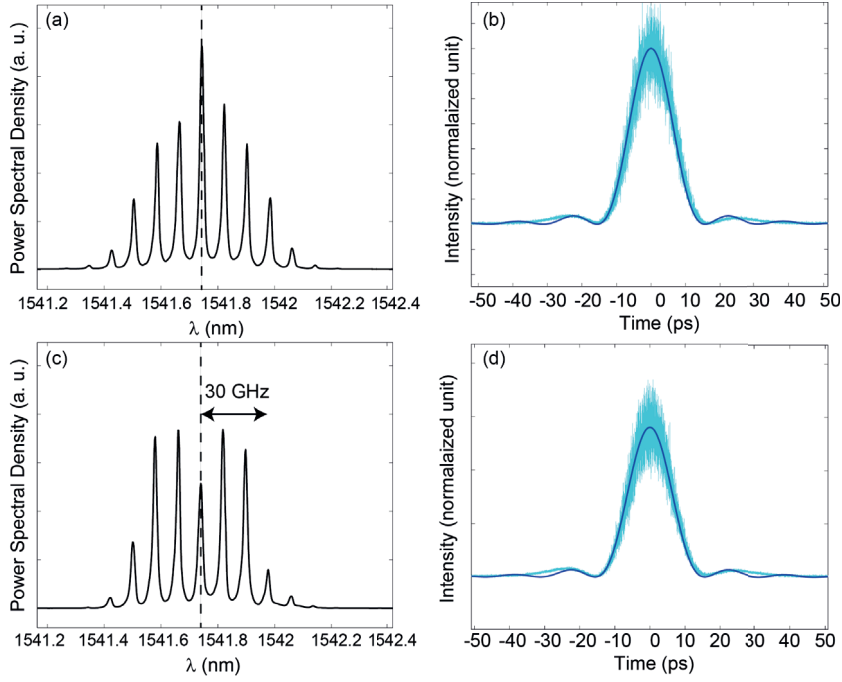


Figure 5.6 – Idler spectrum (a) before chirp compensation, (c) after chirp compensation. Idler pulse trace (b) before chirp compensation, (d) after chirp compensation. In all figures we have $\gamma P_0 L = 3$ [21].

and (f) show that the idler temporal profiles are similar before and after chirp compensation as expected. A very good fit is obtained between experimental results and the one obtained from Eq. 5.2. We also observe that the theoretical pulse shape in Fig. 5.2(b) is in a very good agreement with all measured experimental data. Note that the generated pulses in both cases exhibit an electrical SNR better than 21.5 dB.

As depicted in Fig. 5.5, the spectrum of the chirp compensated pulses is not exactly the same as the spectrum illustrated in Fig. 5.3(a). This discrepancy is due to the saturation of the RF driver and/or the phase modulator used for chirp compensation. In fact the peak-to-peak voltage at the input of phase modulator must be equal to $\gamma P_0 L V_\pi / \pi$, where V_π is the required voltage to reach a phase shift of π at modulator output. At this value the RF driver and the phase modulator did not operate in the linear regime and therefore an ideal chirp compensation is not obtained. This limitation can be eliminated by performing the phase modulation in two sunsequent stages i.e. each phase modulator is driven by the half voltage, remaining in the linear regime.

To verify the effect of phase modulator and the nonlinearities of RF driver, we demonstrate the experimental results for $\gamma P_0 L = 3$, where a lower peak-to-peak voltage is needed to compensate the pump induced chirp. We set the pump peak power to $P_0 = 520$ mW and adjusted the signal wavelength at $\lambda_S = 1570.5$ nm. Figures 5.6(a) and (c) depict the idler spectra on the OSA before and after chirp compensation. It is shown that the spectral power distribution after

5.3. All-Optical Nyquist Pulse Generation by Intensity Modulator

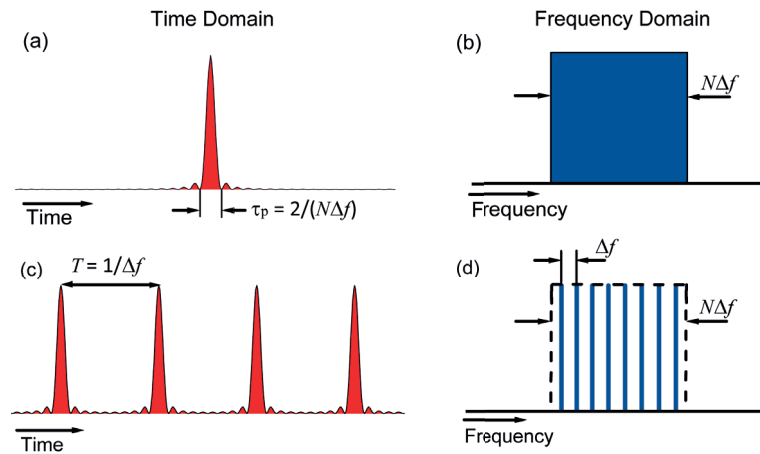


Figure 5.7 – Time (left) and frequency (right) representation of a single sinc pulse (top) and a sinc-pulse sequence (bottom). The Fourier representation of an unlimited sinc-pulse sequence is a rectangular while the spectrum of an unlimited sinc-pulse train is a frequency comb with uniform phase and an rectangular envelop [101].

chirp compensation is closer to a square shaped spectrum as the driver nonlinearities do not contribute. Likewise the case in Fig.5.5, the time trace after chirp compensation (Fig. 5.6(d)) does not exhibit any phase distortion compared to the chirped pulses (Fig. 5.6(b)).

5.3 All-Optical Nyquist Pulse Generation by Intensity Modulator

In this section we present a method to generate high quality Nyquist pulses with an almost ideal rectangular spectrum. The proposed method is based on direct synthetization of a flat phase-locked frequency comb with high suppression of out-of-band components. We will demonstrate theoretically and confirm experimentally that the produced comb corresponds to a periodic sequence of time-unlimited sinc pulses. We also show the wide tunability of the method over four frequency decades.

5.3.1 Theory

Due to the physical limitations, the ideal sinc pulse with perfect rectangular spectrum has not been demonstrated so far. Yet, we proposed a different approach to generate sinc-shaped Nyquist pulses in optical domain, overcoming the limitations imposed by the electronics speed. Basically, the method is based on the time-frequency duality, described by Fourier analysis as illustrated in Fig. 5.7. It is widely known that a single sinc pulse is represented by a rectangular spectrum in the Fourier domain, while the frequency content of an unlimited sinc pulse train is associated with flat frequency comb which components are equally spaced within the bandwidth defined by the single pulse spectrum. Therefore, our approach is based on producing a sequence of sinc pulses by creating an optical frequency comb with uniformly

Chapter 5. Generation of Nyquist Pulses and Detection of WDM-Nyquist Superchannels

spaced narrow-linewidth components having equal amplitude, linear-locked phase and strong out-of-band suppression [102]. A general expression of Nyquist pulses in time domain is:

$$r(t) = \frac{\sin\left(\frac{2\pi t}{\tau_p}\right) \cos\left(\frac{2\beta\pi t}{\tau_p}\right)}{\frac{2\pi t}{\tau_p} \left[1 - \left(\frac{4\beta t}{\tau_p}\right)\right]} \quad (5.5)$$

where τ_p is the duration between two zero crossings of the pulse and β is known as the roll-off factor which is in the range $0 \leq \beta \leq 1$. Among the class of Nyquist pulses, the sinc-shaped pulse is of particular interest owing to its rectangular spectrum [17] and zero roll-off factor.

The Nyquist criterion for a pulse $y(t)$ satisfying zero ISI condition requires that for a particular sampling period, τ_p we have $y(n\tau) = 0$ for any non-zero integer n , where $\tau = \tau_p/2$, while $y(0) \neq 0$. This implies that when the signal is periodically sampled with a period τ , a non-zero value is obtained only at the origin [8]. For instance, the sinc function defined as $\text{sinc}(t) = \frac{\sin(\pi t)}{\pi t}$ is a Nyquist pulse with a rectangular spectrum and is unlimited in time. However, being limited by the causality, the sinc function is only a theoretical construct [103]. Here, instead of generating a single time-unlimited sinc pulse, we proposed a method based on generating a flat frequency comb close to an ideal rectangle. It is shown that the time domain representation of this comb corresponds to an unlimited ISI-free summation of single sinc pulses [101]. For a frequency comb with N lines having equal amplitude of E_0/N and frequency spacing Δf , the equivalent optical field is proportional to $x(t) = \frac{\sin(\pi N \Delta f t)}{N \sin(\pi \Delta f t)}$. For odd N , all sinc pulse peaks have the same phase, so that $x(t_s) = 1$ at every sampling instant $t_s = \frac{n}{\Delta f}$ for all integers n . For even N , $x(t_s) = (-1)^n$, i.e. each pulse peak is of opposite sign with its neighbor pulses. Therefore, considering that the pulse repetition period, $T = \frac{1}{\Delta f}$ is a multiple of the time interval $\tau = \frac{1}{N\Delta f}$, the generated time domain envelop $x(t)$ satisfies the following condition for any integer m :

$$x(m\tau) = \begin{cases} (-1)^{(N-1)m/N} & m = \dots, -2N, -N, 0, N, 2N, \dots \\ 0 & \text{otherwise} \end{cases} \quad (5.6)$$

Accordingly, the sequence of sinc pulses resulting from a locked phase, rectangular frequency comb satisfies the Nyquist criterion i.e. providing free ISI within every pulse repetition period T . Note that for both odd and even N the intensity profile is given by:

$$I(t) = |E(t)|^2 = E_0^2 \frac{\sin^2(\pi N \Delta f t)}{N^2 \sin^2(\pi \Delta f t)} \quad (5.7)$$

There are various approaches for generating an optical frequency comb, such as Er-fiber [104], mode-locked laser [105], combination of strong intensity and phase modulation [106, 107] or highly nonlinear fibers [108, 109]. These frequency combs do not necessarily result in a sequence of Nyquist pulses as the specific conditions; equal line amplitude, linear phase dependence and strong out of band suppression have to be satisfied. As a result, spectral line-

by-line manipulation of the optical Fourier components is necessary to provide the required condition. Generally, the complexity of this kind of pulse shaping increases significantly with the number of spectral lines. Moreover, such pulse shapers cannot process a frequency comb with spectrally spaced lines below 1 GHz [110, 111]. In the following, we present a method for generating the frequency combs using a simple practical method.

5.3.2 Experiment

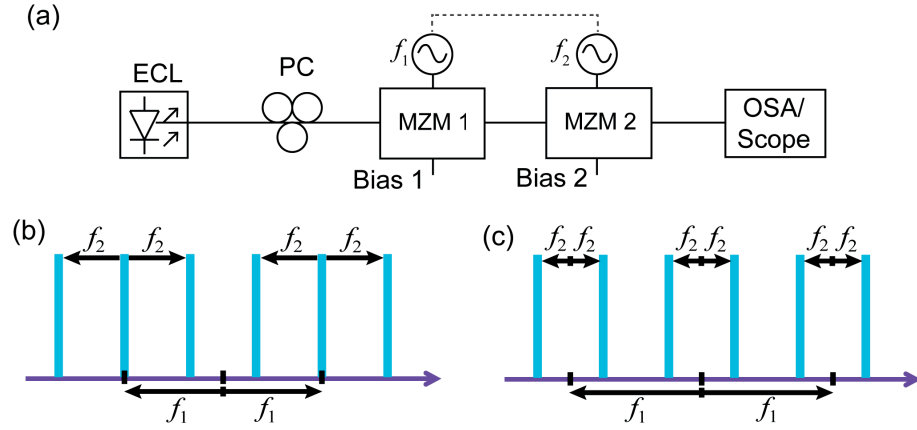


Figure 5.8 – Experimental setup for generating sinc-shaped Nyquist pulses. ECL: external cavity laser; MZM: Mach-Zehnder modulator [101].

Figure 5.8(a) illustrates the experimental setup for generating sinc-shaped Nyquist pulses. The proposed scheme consists of two cascaded lithium niobate MZMs with a specific adjustment of bias and modulation voltages. We used an OSA with a spectral resolution of 0.01 nm to measure the generated frequency combs, while a 500 GHz optical sampling scope is employed to measure the time domain pulse trains. The first modulator is driven by an RF signal at frequency f_1 which generates three seeding spectral components. Subsequently the second MZM re-modulates those lines using an RF signal at frequency f_2 . For instance to produce a frequency comb with $N = 9$ spectral lines, the condition $f_1 = 3f_2$ or $f_2 = 3f_1$ needs to be satisfied without carrier suppression resulting in a frequency spacing of $\Delta f = \min(f_1, f_2)$ between the lines. However, to generate a comb with $N = 6$ lines, the carrier of one of the modulators should be suppressed leading to two different configurations as depicted in Fig. 5.8(b) and (c). In case the optical carrier is suppressed in the first modulator (see Fig. 5.8(b)), the RF frequencies must satisfy the condition $2f_1 = 3f_2$, leading to a line spacing of $\Delta f = f_2$. In the other case, if the carrier is suppressed in the second modulator (see Fig. 5.8(c)), the relation between modulating frequencies must be $f_1 = 4f_2$, resulting in a frequency spacing of $\Delta f = 2f_2$.

To obtain a high quality rectangular-shaped frequency comb we need to tune the DC bias, V_B and the RF voltage amplitude, v_s for each modulator. To make sure that the three generated components by each modulator are in phase, V_B and v_s might take either positive or negative

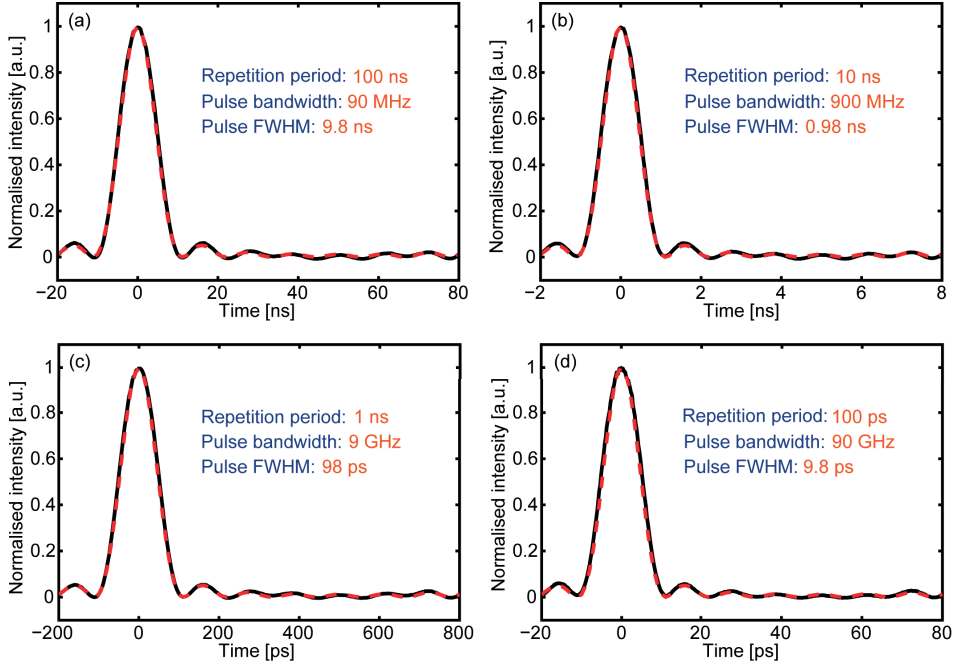


Figure 5.9 – Tunability of sinc-shaped Nyquist pulses from 9 spectral lines. The experimental results (black solid line) are compared with theoretical waveform (red dashed line) over 4 frequency decades. (a) $f_1 = 30$ MHz and $f_2 = \Delta f = 10$ MHz, (b) $f_1 = 300$ MHz and $f_2 = \Delta f = 100$ MHz, (c) $f_1 = 3$ GHz and $f_2 = \Delta f = 1$ GHz and (d) $f_1 = 30$ GHz and $f_2 = \Delta f = 10$ GHz [101].

value [101]. Moreover, to have spectral lines with similar phase using two cascaded MZMs, the phase difference between the modulating RF signals have to be finely adjusted to compensate propagation delays in optical and electrical connections, leading to an almost perfectly shaped symmetric pulses. Note that to confine the sinc-pulse sequence into the Nyquist bandwidth, a low modulating voltage v_s should be employed to strongly suppress the out-of-band components. Particularly, the driving RF voltage v_s of both modulators is remained below $0.36V_\pi$ (where V_π is the half-wave voltage of the MZM), ensuring a suppression more than 27 dB for out-of-band components. This confinement is possible thanks to the two degree of freedom provided by intensity modulators as both operating bias point and modulating voltages can be adjusted.

5.3.3 Results and Discussions

We have experimentally verified the pulse quality and its flexibility by changing the modulating frequencies f_1 and f_2 in a wide spectral range and compare measurements with theoretical results. We have shown frequency comb generation with $N = 9$ within a frequency spanning Δf , spanning over many decades (between 10 MHz and 10 GHz). Figure 5.9 depicts the experimental pulses (black solid line) compared to the theoretical one (red dashed line) described in Eq. 5.7. Measured and theoretical curves are normalized in all figures. Figure 5.9(a) shows the case of modulating frequencies $f_1 = 30$ MHz and $f_2 = \Delta f = 10$ MHz, leads to to a

5.3. All-Optical Nyquist Pulse Generation by Intensity Modulator

sinc-shaped Nyquist pulse with zero crossing pulse duration of $\tau_p = 22.22$ ns, full width half maximum (FWHM) duration of 9.8 ns and repetition period of $T = 100$ ns. In Figs. 5.9(b)-(d), the modulating frequencies have been sequentially increased by one order of magnitude. It can be checked that the spectrum of all these cases result in a spectra close to ideal rectangle with an RMS error below 1%.

The shaded box in Fig. 5.10(a) represents an ideal rectangular spectrum, corresponding to a single sinc pulse with a FWHM duration of 9.8 ps similar to the one reported in Fig. 5.9(d). The red curve which is the experimental flat phase-locked comb exhibits more than 27 dB suppression of the higher order sidebands and a power variation between components lower than 0.2 dB. Clearly the pulse repetition period is $T = 100$ ps.

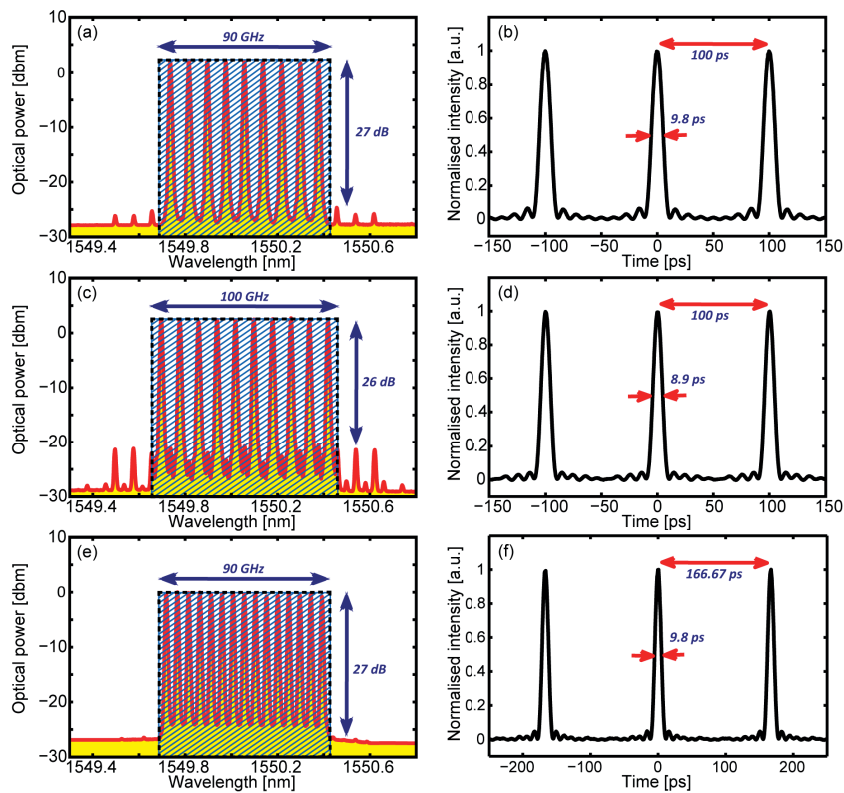


Figure 5.10 – Frequency and time domain representation of the generated sinc-shaped Nyquist pulses. Left column shows the measured spectrum and right column represents time domain waveform for (a),(b) $N = 9$ spectral components separated by $\Delta f = 10$ GHz, expanding over 90 GHz bandwidth, (c),(d) $N = 10$, $\Delta f = 10$ GHz and bandwidth of 100 GHz, (e),(f) $N = 15$, $\Delta f = 6$ GHz, and bandwidth of 90 GHz [101].

The pulse duration and repetition rate can be easily modified by changing the spectral characteristics of the generated combs. For instance, in case the second modulator is driven by two RF signals that are combined in electrical domain, each of the three frequency lines resulting from the first MZM are modulated to produce five spectral components (four sidebands and one carrier). Therefore, $N = 10$ spectral lines separated by $\Delta f = 10$ GHz are generated by

Chapter 5. Generation of Nyquist Pulses and Detection of WDM-Nyquist Superchannels

modulating the first MZM at $f_1 = 25$ GHz in carrier suppression mode and by driving the second MZM with two RF signals at $f_{21} = 10$ GHz and $f_{22} = 20$ GHz. The measured optical spectrum exhibits a bandwidth of 100 GHz and out-of-band components suppression by more than 26 dB as depicted in Fig. 5.10(c). In this case as the first modulator is operating at frequency suppression mode, the main spurious lines observed in the final spectrum are due to the limited extinction ratio of the modulators (here 40 GHz modulator with typical extinction ratio of 23 dB-25 dB). A better suppression ratio and therefore pulse quality can be obtained by employing modulators with better extinction ratio (commercial MZM with 40 dB extinction ratio are available). As the frequency spacing between spectral components is the same as in the previous case, (i.e. $\Delta f = 10$ GHz), the pulse repetition period remains $T = 100$ ps. However, the zero crossing pulse duration is reduced down to $\tau_p = 20$ ps (FWHM duration to 8.9 ps) as illustrated in Fig. 5.10(d).

By rearranging the modulating frequencies to $f_1 = 30$ GHz, $f_{21} = 6$ GHz and $f_{22} = 12$ GHz, and by adjusting the bias point of the first modulator so that the carrier is not suppressed in this case, a frequency comb is obtained which expands over 90 GHz bandwidth with $N = 15$ spectral components, a frequency spacing $\Delta f = 6$ GHz and a suppression factor better than 27 dB for higher order sidebands as depicted in Fig. 5.10(e). The zero crossing duration of the sinc pulse is measured $\tau_p = 22$ ps (FWHM duration of 9.8 ps) and a repetition period of $T = 166.67$ ps as shown in Fig. 5.10(f).

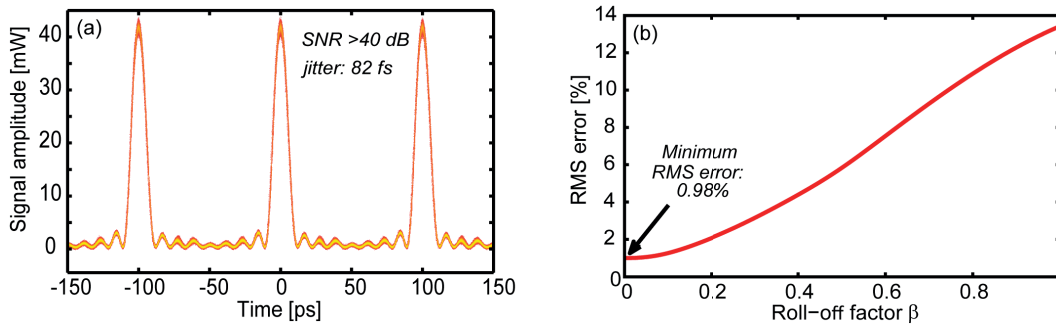


Figure 5.11 – Measured stability and quality of periodic sinc pulses. (a) Color grade of one measured sinc pulse sequence corresponding to the case depicted in Figs. 5.10(a) and (b). Measurements indicate a SNR > 40 dB and a timing jitter of 82 fs. (b) RMS error between the measured pulses and the theoretical sinc pulse intensity, derived from Eq. 5.7 as a function of the roll-off factor, β . The RMS error is minimized for $\beta = 0$ [101].

Figure 5.11(a) shows the color grade of the measured Nyquist pulses for the case presented in Figs. 5.10(a) and (b), demonstrating very stable and high quality sinc-shaped pulse sequence. We measured a very low jitter of 82 ps (equivalent to 0.82% of the FWHM) and very high SNR > 40 dB (above the oscilloscope measurement capability). The corresponding jitter and SNR for all other measured conditions exhibit a similar behavior. The quality of the measured pulses is also estimated by comparing them with the expression obtained from Eq. 5.7. Figure 5.11(b) shows the RMS error between the measured pulses and the theoretical expression as the roll-off factor ranges between 0 and 1. It can be observed that the RMS

5.3. All-Optical Nyquist Pulse Generation by Intensity Modulator

error is minimized for $\beta = 0$, showing that the experimental results fit very well with sinc-shaped Nyquist pulses with an RMS error of 0.98%. Comparing this roll-off factor with the one obtained from other pulse-shaping methods [9, 20, 21, 99], a significant improvement in the pulse quality can be observed.

In optical communication context, the sequence of sinc-shaped pulses can be multiplexed either in time or frequency domain, following the standard approaches for O-TDM and WDM-Nyquist transmission schemes. For an ideal Nyquist transmission system, modulated channels should satisfy the zero-ISI criterion as well. However, in case of data modulated pulses the resulting spectrum is no longer nearly ideal rectangular shape, as reported in Fig. 5.10. In fact modulating the pulses in time domain corresponds to a frequency convolution; the spectrum of modulated sinc-shaped pulses is given by the convolution of the frequency comb and the frequency response of the modulating data. Assuming an ideal rectangular modulation window equal to the pulse repetition period $T = 1/\Delta f$, the frequency comb will be convolved with a sinc function in frequency domain which has zero crossings at $n.1/T = n.\Delta f$ with n being a non-zero integer number. Therefore, the comb frequency lines coincide with the zero crossings of the modulating signal, which also holds true for neighboring WDM channels (assuming zero guard-band).

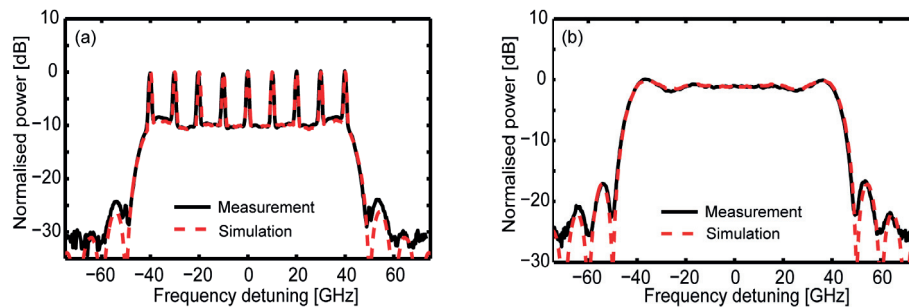


Figure 5.12 – Spectrum of modulated sinc pulses. Measured spectra of modulated sinc pulses (black solid line) with (a) OOK and (b) BPSK modulation format. The simulated results (red dashed line) are obtained by including OSA finite spectral bandwidth (0.01 nm) [101].

Figures 5.12(a) and (b) depict the measured spectra respectively for OOK and BPSK modulation format. To provide a more accurate comparison, the simulation results obtained by including the spectral response of the OSA (a resolution filter with 0.01 nm bandwidth) are shown as well. A very good agreement can be observed between simulated (red dashed line) and experimental (black solid line) results in terms of spectral broadening. The slight difference can be justified by the non-ideal rectangular modulation window as well as additional convolutions between the small out-of-band comb lines and the modulation spectrum. The experimental and simulation results show that a spectral broadening, termed *excess bandwidth* [103], of about 11% results from modulating the generated pulses (assuming only the power within the main spectral lobe, confining about 99% of the power). It is worth noting that the excess bandwidth, defined as a percentage of the Nyquist frequency, does not depend on the roll-off factor of unmodulated pulses as this factor is practically zero in our case. Therefore, the broadening

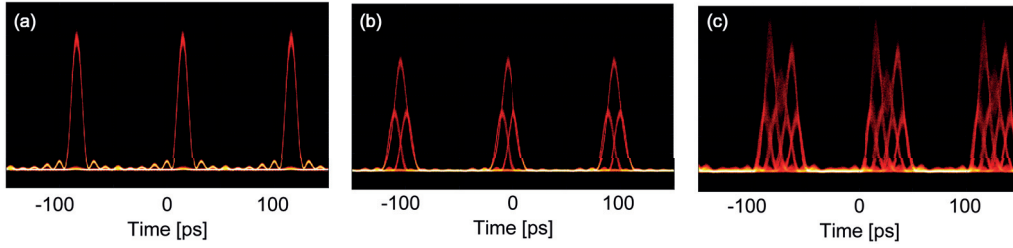


Figure 5.13 – Eye-diagram of intensity modulated sinc pulses, (a) initial modulated pulse train, (b) two times O-TDM pulse train, (c) four times O-TDM pulse train.

here is only determined by the ratio between the pulse repetition rate (defining the modulating window) and the pulse width (defining the Nyquist bandwidth), being proportional to $\Delta f / (N\Delta f) = 1/N$ (where N is the number of lines in the comb). It is therefore noticeable that even with $N = 9$ spectral lines, the resulting excess bandwidth from modulation would be $1/N = 0.11$ which is much lower than the values obtained from other optical pulse shaping methods for generation Nyquist pulses. Such methods lead to a roll-off factor between $\beta = 0.4$ [99] and $\beta = 0.5$ [19, 20] before any modulation which is already much higher than 0.11 that we obtained after modulation. More importantly, due to the fixed relation between the symbol duration of the modulated data and the pulse width, this broadening does not necessitates guard-bands between WDM channels as discussed before.

Figure 5.13(a) depicts the eye-diagram of a intensity modulated sinc pulse for the case $f_1 = 30$ GHz and $f_2 = 10$ GHz. The orthogonality property is verified in Figs. 5.13(b) and (c) which demonstrate respectively two and four times O-TDM of the initial pulse train. The open eye-diagrams clearly show the ISI-free operation of this scheme.

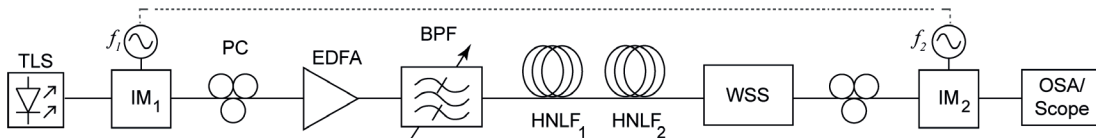


Figure 5.14 – Sinc-shaped Nyquist pulse generation using a nonlinear stage between two intensity modulators. TLS: tunable laser source; IM: intensity modulator; PC: polarization controller; BPF: bandpass filter; WSS: wavelength selective switch.

Bandwidth Extension of Nyquist Pulses by FWM

Though the proposed method in this section is a simple and cost-effective technique for generating Nyquist pulses, the resulting bandwidth remains limited to three times the electrical bandwidth of the modulators. To overcome this bandwidth limitation, we employ a nonlinear stage based on FWM in an HNLF to further expand the comb bandwidth while maintaining the high flexibility and reconfigurability of the original technique. Figure 5.14 illustrates the principle of generating sinc-shaped pulses with extended bandwidth. We can recognize three

5.3. All-Optical Nyquist Pulse Generation by Intensity Modulator

stages in this sketch to obtain a Nyquist sinc pulse train from an initial CW laser. The first and third stages operate based on intensity modulation while the second stage is based on FWM process [101, 112], combined with wavelength selective switch (WSS) device [113].

At the first stage, the CW input is intensity modulated via (IM_1), with a sinusoidal wave. Assuming the repetition rate of final desired pulse to be f_R , the modulation frequency of this stage should be set to $N \times f_R$, where N is the number of optical tones generated at the third stage for a single optical carrier at its input. By adjusting the bias voltage and driving amplitude of IM_1 , the amplitude of the carrier and first-order tones are equalized while higher order tones are strongly attenuated.

The modulated signal is next amplified by an EDFA and launched into a cascade of HNLF spools. Through FWM process, energy is transferred from the three initial frequency lines to generate new spectral lines at a multiple of $N \times f_R$. The number of spectral lines at the output of 2nd stage would depend on the power spectral density (PSD) of the three initial lines, the inject power into HNLFs, as well as dispersion properties of the fiber ensemble. Therefore, by setting the EDFA output power and dispersion management of the fiber span, the number of lines with minimized PSD variations can be optimized. Note that the maximum power launched into the fiber for each spectral component is limited by the SBS threshold. Using several spans of HNLF with different ZDWs, would improve FWM bandwidth while enhancing the Brillouin threshold. A WSS is then used to select K spectral components from this stage. The filter is programmed to equalize the amplitudes and adjust the phases of the selected components. This leads to the generation of a flat comb of K equally spaced in-phase lines with $N \times f_R$ frequency spacing.

Finally, the 3rd stage re-modulates the optical frequency comb by an intensity modulator (IM_2). In case IM_2 is driven by a single RF tone, each component of the comb will generate two first-order sidebands; therefore increasing the number of lines within the comb. Further scaling can be obtained by multiplexing RF tones in the electrical domain. Similar to the 1st stage, by adjusting the bias voltage and RF power, a flat comb with minimized out-of-band components can be obtained. Consequently, the 3rd stage allows to down rate the repetition frequency of the sinc-shaped pulse train to the frequency f_R while maintaining the rectangular shape of the optical comb.

To experimentally verify the flexibility of the proposed scheme in terms of pulse duration and repetition rate, we investigated two different cases. For both cases, the electrical bandwidth of the IMs is 40 GHz and the FWM process is optimized to provide an efficient bandwidth expansion. For that, the 2nd stage comprises two HNLFs; $HNLF_1$ is 350 m long with ZDW at 1569 nm and $HNLF_2$ is 500 m long with ZDW at 1553 nm. We set the wavelength of initial CW laser at 1557 nm to be close to both ZDW of HNLFs.

In the first experiment we realized a sinc-shaped Nyquist pulse train with 10 GHz repetition rate. At the 1st stage, IM_1 is driven by a 30 GHz clock in order to provide three spectral lines separated by 3 times the desired f_R , see Fig. 5.15(a). By optimizing the parameters, 9

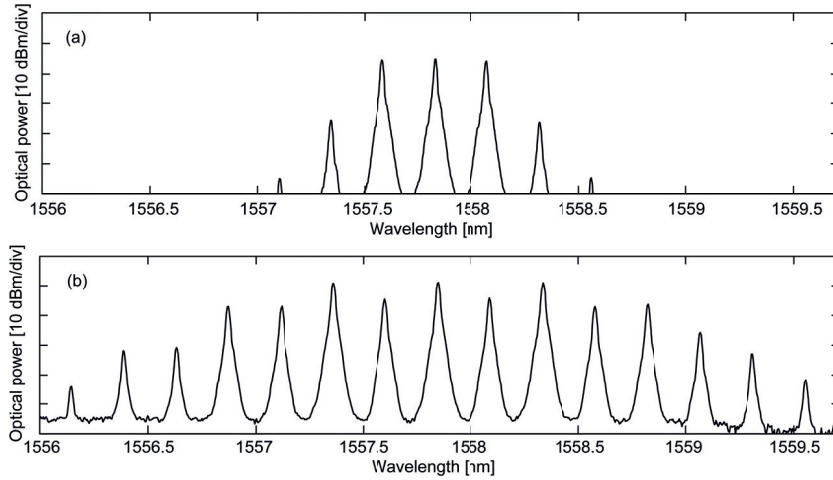


Figure 5.15 – Measured spectra after the (a) 1st stage, (b) HNLFs at the 2nd stage for generating sinc-shaped Nyquist pulse train at 30 GHz repetition rate [114].

equally spaced components are produced at the HNLF₂ output, within a 6 dB PSD variations (Fig. 5.15(b)). The injected power to the input of HNLF₁ was measured at 22.5 dBm. Employing the WSS, we selected $K = 9$ spectral lines, equalized their amplitude and made the components in phase. Figure 5.16(a) shows the resulting spectrum with the bandwidth of 270 GHz. The corresponding temporal profile is depicted in Fig. 5.16(b). We measured an out-of-band rejection of spectral components better than 40 dB, restricted by the OSA sensitivity. The temporal waveforms recorded by the optical sampling oscilloscope exhibit a peak-to-first-zero crossing of 3.7 ps. We sent the 30 GHz repetition rate pulse train to the last stage where IM₂ is driven by a 10 GHz clock. By optimizing the bias and amplitude voltage, 3 equal amplitude components with 10 GHz spacing are generated from each initial spectral line. We obtained rectangular frequency combs spanning 270 GHz but with an increased number of spectral lines to 27 as depicted in Fig. 5.16(c). We measured an out-of-band rejection better than 32.5 dB. The corresponding temporal profile (Fig. 5.16(d)) is sinc-shaped pulses at 10 GHz repetition rate. The pulse width in this case are similar to that of 30 GHz pulses as the spectral bandwidth is remained identical.

In another experiment, a 5 GHz repetition rate sinc-shaped Nyquist pulse train is implemented. We drive the intensity modulator of the 3rd stage, IM₂ by two RF clock generators at 5 GHz and 10 GHz, such that the frequency spacing equals to the desired repetition rate, $f_R = 5$ GHz. Therefore, to generate a comb with a spectral spacing 5 times f_R at the 1st stage, a 25 GHz clock was applied to IM₁. At the 2nd stage we selected a rectangular comb with $K = 9$ spectral lines. The 3rd stage then generates 5 tones from each initial line, optimized to maintain the rectangular spectral shape. Figure 5.17(a) illustrates the measured spectrum of 45 line frequency comb covering a 225 GHz bandwidth. The corresponding temporal profile is depicted in Fig. 5.17(b). The rejection of out-of-band frequency components is measured better than 28 dB. The temporal recorded pulse train at 5 GHz repetition rate has 4.4 ps peak-to-zero width at FWHM in agreement with the theory. The small residual peaks are due to

5.4. All-optical Detection of WDM-Nyquist Superchannels

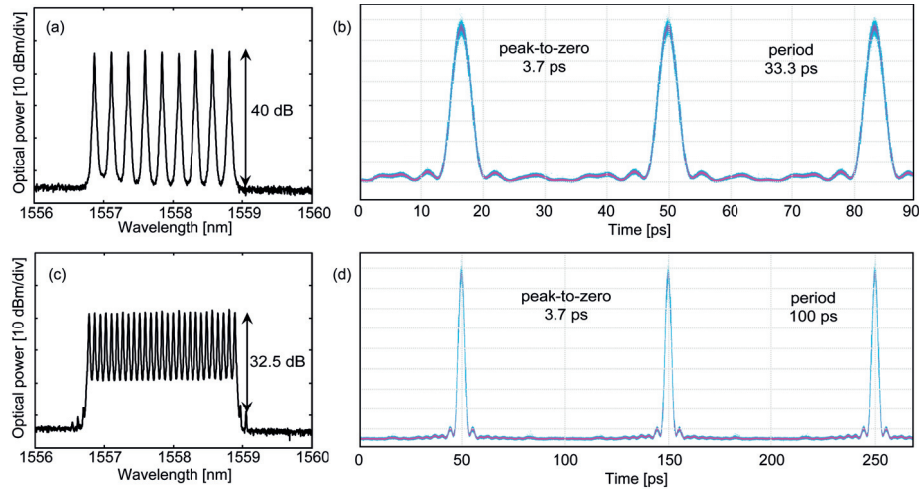


Figure 5.16 – Sinc-shaped Nyquist pulse train at 30 GHz repetition rate (with $N = 1$). (a) Measured spectrum from a bandwidth of 270 GHz. (b) The corresponding temporal profile. Sinc-shaped Nyquist pulse train at 10 GHz repetition rate (with $N = 3$). (c) Measured spectrum for a bandwidth of 270 GHz. (d) the corresponding temporal profile [114].

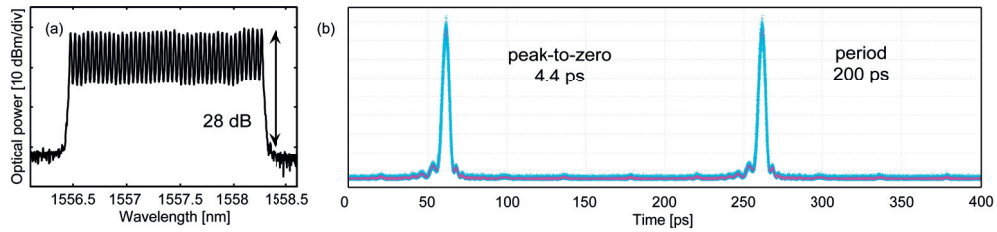


Figure 5.17 – Sinc-shaped Nyquist pulse train at 25 GHz repetition rate (with $N = 5$) (a) Measured spectrum of the 255 GHz rectangular frequency comb, (b) the corresponding temporal profile [114].

slight phase mismatch and unequal level of the resulting 45 spectral lines.

We verified the quality of sinc-shaped Nyquist pulses by comparing them with the theoretical expression given by Eq. 5.7 as a function of the roll-off factor β . The minimum RMS error is achieved for all cases when $\beta = 0$. Such good agreement was expected from the flatness (< 1 dB power variations) of the frequency comb and the out-of-band rejection ratio (at least 28 dB). However, for the comb with 225 GHz bandwidth the RMS error increases up to 6%. This deviation comes from variations in the phase locking of the spectral lines as well as the limitation imposed by the 500 GHz scope.

5.4 All-optical Detection of WDM-Nyquist Superchannels

As discussed in previous section Nyquist pulses enable multiplexing of high spectral efficiency channels in the time domain without ISI as well as guard-band free frequency multiplexing.

Chapter 5. Generation of Nyquist Pulses and Detection of WDM-Nyquist Superchannels

However, one major challenge regarding these pulses is developing an efficient demultiplexing technique for the corresponding superchannels. ISI-free detection of O-TDM Nyquist pulses is obtained by conventional sampling schemes. For high symbol rates such as beyond 40 Gbaud, optical sampling techniques are essential due to limited electrical bandwidth. Optical samplers are generally based on creating a short time window and sampling the exact channel pulse time location. However, in practice these methods are energy inefficient as they only collect small portion of pulse energy. Moreover, the corresponding experimental setups are complex and expensive and require many electrical and optical apparatus to maintain a low duty cycle and high repetition rate time windows [22, 23].

An alternative method to implement such demultiplexing is the inner product of the incoming data and the train of Nyquist pulses aligned with the desired channel. This approach has been verified using balanced detection, where it needs a local optical Nyquist pulse generator, as well as some digital signal processing after photo detection to minimize the phase error [115].

In this section we investigate an all-optical method to demultiplex WDM-Nyquist superchannels. We first present the principle of this technique which is based on matched filter receiver. The experimental setup and the corresponding results will then be described; showing real-time demultiplexing of WDM-Nyquist superchannels with a simple all-optical method.

5.4.1 Principle of Operation

Figure 5.18 demonstrates the principle of demultiplexing WDM-Nyquist superchannel. A train of optical sinc-shaped pulses, $S(t)$ generated from a flat rectangular comb is given by:

$$S(t) = \frac{E_{D_0}}{N} \frac{\sin(\pi N f_R t)}{\sin(\pi f_R t)} e^{2i\pi f_0 t} \quad (5.8)$$

where f_R is the repetition rate, N is the number of spectral lines, E_{D_0} is the pulse peak amplitude and f_0 is the carrier frequency. Passing through the delay line, the incoming sequence goes through a Nyquist pulse carver. The carver is based on the Nyquist sinc-pulse generation method explained in section 5.3. The corresponding bias and amplitude voltages are set as in [102] to provide a sinc-shaped time window. Once the incoming sequence passes through the carver and is next filtered with an optical bandpass filter centered at f_0 , the resulting output signal would become:

$$E_0(t', \tau) = \int_{-\infty}^{+\infty} S(t - \tau) \frac{V_c \sin(\pi N f_R t)}{\sin(\pi f_R t)} h(t - t') dt \times e^{2i\pi f_0 t'} \quad (5.9)$$

where τ is the delay between the peaks of $S(t)$ and the phase-locked RF tones, V_c is proportional to the amplitude voltages and $h(t)$ is the optical filter impulse response. When $h(t)$ has a rectangular shape of width $1/f_0 = T_S$, Eq. 5.9 represents the inner product between two repeating sinc-shaped functions over one symbol length, where $E_0(t', 0) = V_{CO} E_{D_0} / N^2$. The integration in Eq. 5.9 reveals that $E_0(t', k/(N f_R)) = 0$ for all non-zero integer, k . Considering

5.4. All-optical Detection of WDM-Nyquist Superchannels

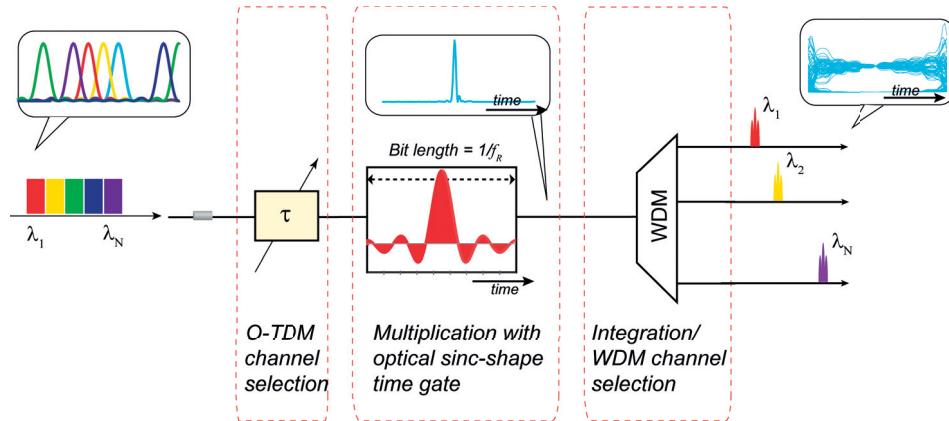


Figure 5.18 – Principle of demultiplexing WDM-Nyquist superchannel. The incoming sequence undergoes an inner product with Nyquist carrier. A bandpass filter then integrates the product and selects the WDM channels. The ISI collected from adjacent channels in this technique is ideally zero [116].

a Nyquist superchannel consisting of N tributaries, any channel can be demultiplexed by aligning it with the sinc pulse carrier using the delay line. Note that in case of WDM-Nyquist superchannel, the desired WDM channel can be selected by tuning the central frequency of the filter.

5.4.2 Experiment

To verify the proposed demultiplexing method we conducted an experiment using the setup illustrated in Fig. 5.19. The setup consists of multiplexing and demultiplexing blocks. To generate a WDM-Nyquist superchannel, three tunable lasers are first multiplexed in wavelength using a WDM filter. The combined waves are then modulated by a 10 Gb/s NRZ $2^7 - 1$ PRBS. A spool of 10 km long SMF is used to decorrelate the NRZ WDM channels so that the data in adjacent wavelength channels become independent. The sinc-shaped Nyquist pulses are generated by the method described in section 5.3 leading to high quality pulses. The two modulators used for pulse generation are driven with sinusoidal waves at frequencies $f_1 = 30$ GHz and $f_2 = 10$ GHz on all WDM channels. A bit rate multiplier (BRM) is then used to produce 8 Nyquist tributaries at each wavelength and multiplex them in time. This results in a WDM-Nyquist superchannel with 240 Gb/s aggregate data rate. Careful tuning of the variable delay at each multiplication stage is essential to ensure that the delay between two adjacent channels is equal to $1/(Nf_R)$ to achieve orthogonal multiplexing. We used a low-noise EDFA before the BRM to optimize the noise figure of the generated signal.

At the demultiplexing stage, a sinc-shaped Nyquist carrier similar to the one used for generating the superchannel is made with two IMs driven at 10 GHz and 30 GHz, resulting in an almost ideal sinc-shaped Nyquist time window which carves the incoming Nyquist superchannel. A variable optical delay line (VODL) is placed before the demultiplexer to select the specific

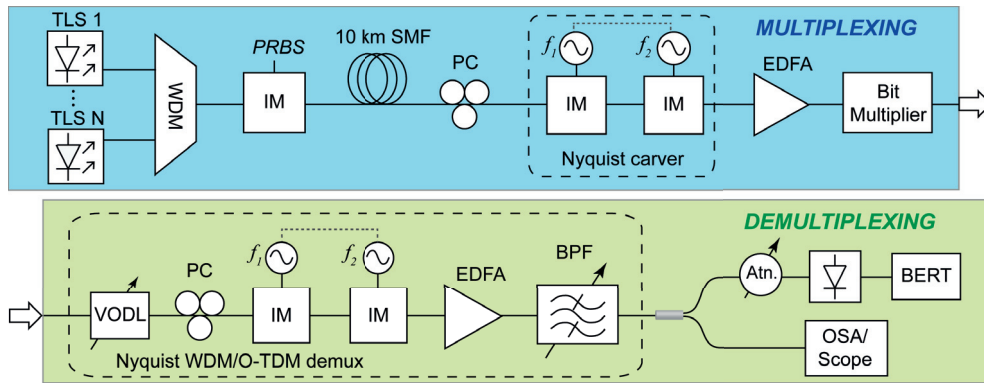


Figure 5.19 – Experimental setup for real-time demultiplexing of WDM-Nyquist superchannels. TLS: tunable laser source; WDM: wavelength division multiplexer, IM: intensity modulator; PC: polarization controller; BRM: bit rate multiplier; VODL: variable optical delay line; BPF: bandpass filter, Atn: attenuator; BERT: bit-error rate tester [116].

time tributary. The carved signal is finally amplified and passed through a Gaussian filter with 24 GHz FWHM to emulate time integration of the optical fields. Note that the filter acts as a WDM demultiplexer as well. Finally we acquire the signal after a variable attenuator through a 10 Gb/s digital photodetector. An oscilloscope and a bit-error rate tester (BERT) are used to measure the quality of demultiplexed signal.

5.4.3 Results and Discussions

Figure 5.20(a) depicts the eye-diagram of a Nyquist superchannel which is made of 8 O-TDM tributaries of Nyquist pulses (the pulse width and period can provide maximum 9 O-TDM tributaries). The measured data are obtained by a 500 GHz optical sampling scope. The optical spectrum of the three WDM-Nyquist superchannels is also shown in Fig. 5.20(b). We chose the central wavelength at 1539.9 nm while the two other WDM channels were placed at ± 90 GHz from the central channel, therefore realizing guard-band free WDM scheme. Note that though total spectrum is spread over 270 GHz bandwidth, thanks to the negligible variation in the response of intensity modulators, simultaneous Nyquist pulse carving is possible. Figure 5.21(a) shows the BER of all 8 demultiplexed tributaries when only one WDM channel is present. We observe that the performance of all channels is similar as a function of received power. The variations that is observed is due to the laser phase noise which prevents perfect O-TDM through the BRM. The BER of all tributaries of the central WDM channel when the three channels are present is shown in Fig. 5.21(b) showing that the BER is degraded in case of WDM operation.

To have a better insight on the experimental results, we carried out a numerical simulation taking into account the experimental condition. Figures 5.22(a)-(c) show the simulated electrical eye-diagrams of a demultiplexed tributary for the case of one WDM channel (Fig. 5.22(a)) and 3 WDM channels (Fig. 5.22(b)). The case of an edge WDM channel is also depicted in

5.4. All-optical Detection of WDM-Nyquist Superchannels

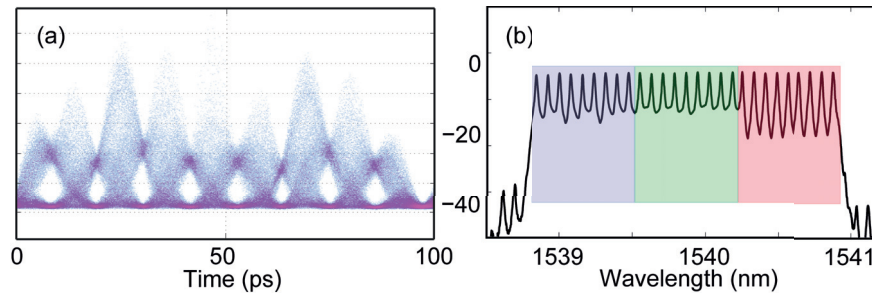


Figure 5.20 – Spectral and temporal representation of WDM-Nyquist superchannel. (a) Eye-diagram of O-TDM tributaries for a single wavelength. (b) Optical spectrum of three guard-band free WDM-Nyquist channels [116].

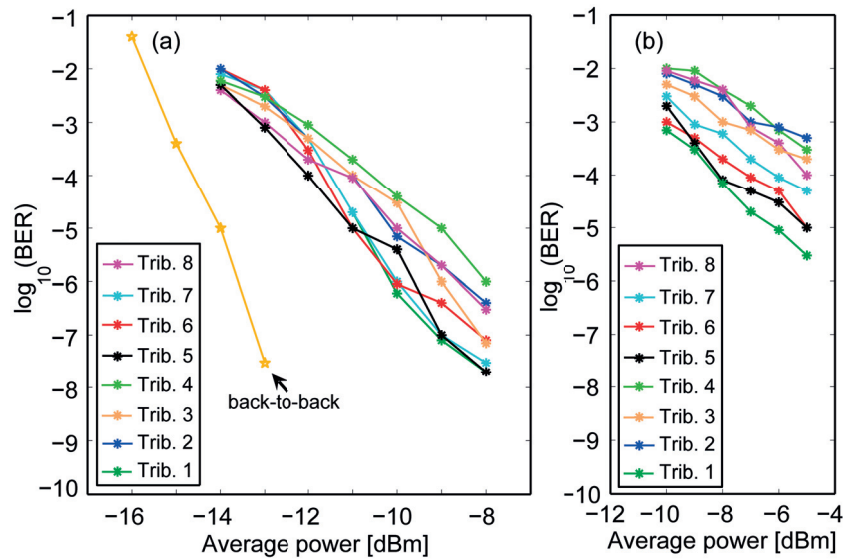


Figure 5.21 – Experimental BER of demultiplexed tributaries of a WDM-Nyquist superchannel for (a) single wavelength (b) middle wavelength of three WDM-Nyquist superchannels [116].

Fig. 5.22(c). We used a Butterworth digital filter to simulate digital photodetector. The corresponding experimental eye-diagrams are shown respectively in Figs. 5.22(d)-(f). The extracted Q-factors from the simulated results are in a good agreement with BER measurements shown in Fig. 5.20. We did not include the noise in simulation; therefore the degradation of Q factor is only from ISI between the O-TDM tributaries and crosstalk from WDM channels.

One of the factors which introduces error to the experiment is that we used a filter with a Gaussian rather than the required rectangular function. Numerical simulations were done using a sinc-shaped filter in frequency domain to verify this effect. Note that such filters can be realized using fiber Bragg gratings [117]. Figures 5.23 (a) and (b) show the optical eye-diagram after optical filtering with a Gaussian and sinc-shaped filter, respectively. As expected, a Gaussian impulse response filter generates optical Gaussian symbol pulses of the demultiplexed channel, while the sinc-shaped filter leads to an NRZ stream. We observe that

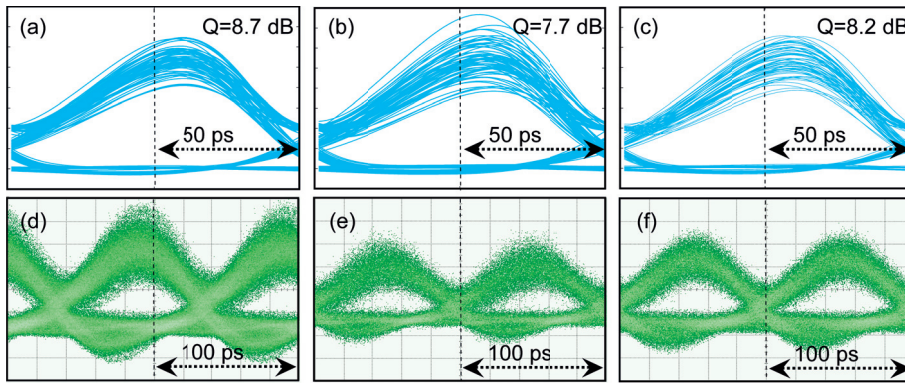


Figure 5.22 – Simulation and experimental eye-diagrams of demultiplexed tributaries for 8 O-TDM, 3 WDM Nyquist superchannels (a,b) single wavelength, (b,e) middle wavelength in 3 WDM channel scheme, (c,f) edge channel in 3 WDM channels scheme [116].

the sinc-shaped filter enhances the optical Q-factor while some imperfection is still present in the eye-diagram. The remained interference is attributed to the fact that each tributary symbol pulse is placed at center of its bit slot where the integration is performed. As a result, the bit location of the O-TDM tributaries do not coincide. Therefore, when a tributary is demultiplexed, symbol switches from other tributaries lead to a non-zero ISI. Note that this effect is present in any demultiplexing scheme based on integration. One way to confront this limitation is to coincide the bit slots of all tributaries [118]. This modification can be achieved changing the positions of the modulators and delays at the transmitter. In fact in our experiment the identical sinc pulse tributaries are first modulated by data and the delayed to make an orthogonal superchannel; referred to as "bit non-assigned" case. However, in the modified scheme that is called "bit assigned" format, we first apply incremental time delays to identical sin pulse tributaries and then apply synchronized modulation. By maintaining synchronization between the wavelength channels it is possible to apply techniques to orthogonally separate data channels. The difference between the bit non-assigned and bit assigned cases is depicted in Figs. 5.23(b) and (c). Figure 5.23(c) shows that operating in bit-assigned scheme leads to infinite optical Q-factor compared to the bit non-assigned scheme depicted in Fig. 5.23(b). However, in practice the limited rise/fall time of NRZ modulators can degrade the quality of demultiplexed signals. Indeed for the tributaries that are located at the edge of the bit slots, the eye-diagram of modulated signal would suffer from intense shaping by the modulator rise/fall time. The eye-diagram of one such channel for a 10 ps rise/fall time is depicted in Fig. 5.23(d) showing a strong degradation of the Q-factor.

5.5 Discussion and Conclusion

Section 5.2 presents a technique based on parametric amplification to produce sinc-shaped Nyquist pulses. We used active chirp compensation scheme to cancel the pump induced frequency broadening of the pulses. In section 5.3 we introduced another method to generate

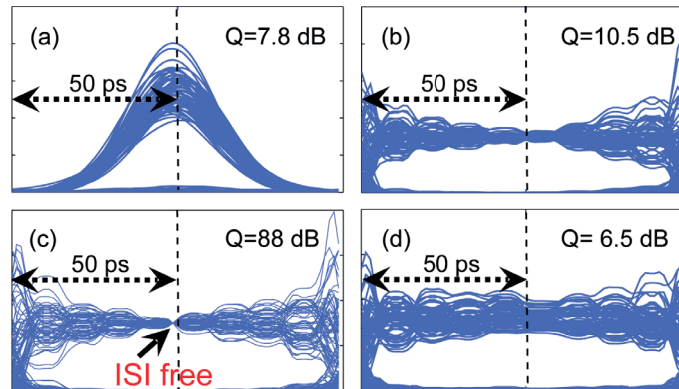


Figure 5.23 – Simulated optical demultiplexed eye-diagrams of a tributary in a WDM-Nyquist superchannel with 8 orthogonal TDM tributary and 3 WDM channels for (a) Gaussian filter, bit non-assigned, (b) Nyquist filter, bit non-assigned, (c) Nyquist filter, bit assigned, (d) Nyquist filter, bit assigned including rise/fall time a tributary at the edge of bit slot [116].

a sequence of very high quality sinc-shaped Nyquist pulses with an almost ideal rectangular spectrum and verified it by experiment. The method is based on the direct synthesis of a flat phase-locked frequency comb with high suppression of out-of-band components. The results show that this comb corresponds to a periodic sequence of time-unlimited sinc pulses. The wide tunability of the proposed technique based on two cascaded MZMs is demonstrated over 4 frequency decades. Experimental results confirm the remarkable quality of generated pulses, which exhibit zero roll-off factor, minimum spectral broadening when modulated and less than 1% deviations with respect to the ideal sinc-shaped pulses. The generated pulses simultaneously show a minimum ISI and maximum spectral efficiency, making them an attractive solution for high-capacity WDM-TDM systems.

We also proposed an extension to the mentioned scheme by inserting a nonlinear stage between the two MZMs. This stage when combined with a WSS can generate equalized in-phase spectral lines beyond the electronic bandwidth limits. This is key to generate all-optical Nyquist pulses with duration divided by up to 3 times at any repetition rate. Additionally, the method allows for full tunability of the repetition rate, in the limit of the electrical bandwidth of the intensity modulators. The presented scheme can be used to control the way that total bandwidth is shared between users in granularity flexible WDM-Nyquist superchannels.

In section 5.4 we introduced a flexible method to demultiplex WDM-Nyquist superchannels simultaneously in time and frequency. This all-optical method is based on matched filter receiver and is implemented using intensity modulators, pulse positioning and filtering. Taking advantage of this method we performed real-time demultiplexing of 240 Gb/s WDM-Nyquist superchannel. The proposed method does not need any coherent scheme while it is format transparent and compatible to WDM networks. Simulations show that the performance can be improved by using sinc-shaped optical filters.

6 Conclusion and Perspective

The first objective of the thesis was to explore techniques and methods to enhance the functionality of high speed wavelength division multiplexed (WDM) networks and enable new signal processing schemes. The second objective was to present a simple all-optical technique for generation and detection of WDM-Nyquist superchannels which are known for their high spectral efficiency. In this respect, the following four main problems have been studied in this thesis.

1. Simultaneous wavelength conversion and time compression of WDM channels for transparent connection of dissimilar rate WDM networks.
2. 3R (reampification, reshaping, retiming) optical amplitude regeneration of WDM channels in a scheme with scalability property.
3. Optical generation of sinc-shaped Nyquist pulses for producing high quality WDM-Nyquist superchannels.
4. Real-time optical demultiplexing of WDM-Nyquist superchannels simultaneously in time and frequency using a simple scheme.

Next, in this closing chapter, a summary and a list of relevant conclusions drawn from the thesis studies are presented. Finally, in contribution of this work, some directions and topics are suggested for future possible research.

6.1 Summary and Conclusion

Simultaneous wavelength conversion and time compression of WDM channels for transparent connection of dissimilar rate WDM networks

In this study we investigated dual-pump fiber optical parametric amplifier (FOPA) as a signal processing device, used for simultaneous wavelength conversion and time compression of

WDM channels. We showed by operating in pulsed pump regime, the parametric gain is gated by a time window that is multiplied by the signal and idler. Owing to the properties of dual-pump FOPA this window can be uniformly generated over a wide wavelength range. We showed in theory and experiment that by compensating the inherent chirp of the window as well as modifying the modulation of the pumps, one can compress the time window by more than 4.7 times. This high compression factor together with the uniform wavelength response of the time window allowed for simultaneous wavelength conversion and time compression of WDM channels.

3R (reamplification, reshaping, retiming) optical amplitude regeneration of WDM channels in a scheme with scalability property

This study was focused on enabling a signal processing device which can perform 3R regeneration for WDM channels. Taking advantage of dual-pump FOPA, we showed that operating in saturation regime provides 2R (reamplify, reshape) functionalities. Moreover, once the pumps are modulated in intensity, the created time window enables retiming property and therefore a full 3R scheme is realized. We showed that by setting the right dispersion parameters this device can operate uniformly for several WDM channels. In addition, the inter-channel crosstalk effects can be controlled by proper design of FOPA parameters. We successfully demonstrated 3R regeneration for five WDM channels modulated with 10 Gb/s NRZ-OOK data leading to an average 1.5 dB improvement in receiver sensitivity. This scheme can be scaled up to regenerate more channels without any need to increase the complexity.

Optical generation of sinc-shaped Nyquist pulses for producing high quality WDM-Nyquist superchannels

In this study we investigated generation of Nyquist pulses by direct synthesis of flat, phase-locked optical frequency comb. We used a simple experimental setup to generate these pulses based on cascaded Mach-Zehnder modulators driven by proper RF frequencies. The results show that pulses have exceptional quality, close to perfect sinc-shaped Nyquist pulses. We checked the flexibility of this method by generating pulses at various pulse width and repetition rate in four frequency decades. We also studied the spectrum of the pulses with phase and intensity modulation, showing an excellent agreement with simulation results. Furthermore, by introducing a nonlinear stage in this scheme, we demonstrated the extension of pulse bandwidth, leading to shorter Nyquist pulses. These pulses can be used to generate high quality WDM-Nyquist superchannel for high speed optical communication links.

Real-time optical demultiplexing of WDM-Nyquist superchannels simultaneously in time and frequency

This study was aimed to implement an in-line technique for demultiplexing WDM-Nyquist superchannels. We realized a simple method based on matched filter receiver concept where the inner product of incoming sequence and a Nyquist time window is realized in the optical domain. We used a WDM filter for completing the inner product as well as providing WDM demultiplexing scheme. In theory, this technique can sample the data tributaries without inter-symbol interference from neighbor tributaries or other wavelength channels. We showed successful demultiplexing of WDM-Nyquist superchannels with 8 orthogonal time division multiplexed tributaries for 3 WDM channels. This scheme can in theory improve the WDM network performance by enabling a simple error-free demultiplexing scheme. However, the resulting performance is lower than predictions due to imperfect implementation of the technique.

6.2 Future Works

In the continuation of this work, the following topics are suggested for future possible research:

- In chapter 3 we studied pulse generation in single and dual-pump FOPA and observed that these pulses undergo a pump induced chirp which can be later compensated. However, another approach is to directly produce chirp-free pulses at the FOPA output. This can be achieved by pre-chirping the pumps using a phase modulator driven by the same RF frequency used for modulating their intensity. The pump phase modulation not only compensates the chirp term but it brings the advantage of increasing the Brillouin threshold, avoiding any additional phase modulation for pump linewidth broadening. Our calculation shows by implementing this technique a pulse source based on parametric amplification can be realized with zero output chirp and no degradation due to residual pump phase modulation which is a severe obstacle in feasibility of this pulse generation technique.
- The other possibility in chapter 3 is further investigation of dissimilar modulation of the FOPA pumps. As explained in section 3.3.4, employing two sinusoidal waves with different frequencies, enables partial de-correlation of pulse duration and repetition rate. However, extensive studies need to be done for removing the pulse pedestals using for example various thresholding techniques. Moreover, employing other modulation waveforms such as rectangular or triangular shapes provides new schemes in shaping the idler pulses or providing new degrees of freedom such as tuning the pulse width by inserting proper delay between the two waves. More importantly, as dual-pump FOPA transfers the multiplication of the pumps to the idler, it can be used as a flexible mixing technique which has various application such as generating microwave signals.
- Referring to chapter 4 on 3R WDM regeneration, we showed successful regeneration

of five WDM channels, each with 2 mW input power. In actual conditions, the power of input signal to undergo regeneration could be much lower. However, the necessity to operate FOPA in saturation regime at moderate gain level, imposes a limit on the minimum signal power. One interesting direction is to deal with this issue by employing a dummy signal at the regenerator input. Proper adjustment of the dummy signal position and power, can substantially reduce the saturation power without introducing any interfering frequency components. Another noteworthy direction on this topic, is to verify the regenerator performance for RZ signals that convey information in their phase such as PSK or DPSK modulation formats.

- As it was explained in chapter 5, we developed a simple all-optical technique for demultiplexing WDM-Nyquist superchannels which samples the desired tributaries without any interference in time or frequency from other channels. Using Gaussian filters instead of rectangular-shaped filters and also the symbol switch during an integration period, are two issues that prevented a perfect system implementation. One important future direction of this research is to use rectangular time-response filters (sinc-shaped in frequency) to provide the condition that is required from theory. Moreover, the symbol switch problem, (introduced as bit non-assigned format in chapter 5) can be solved by first delaying the Nyquist pulse trains to form orthogonal tributaries and then modulated them with data (bit assigned format). Furthermore, verifying the demultiplexing scheme for DPSK modulated WDM-Nyquist superchannels is another valuable direction which would show the effectiveness of our scheme for phase modulation formats.

A Appendix

A.1 Gain Sensitivity

To derive $S_{P_1}^G$ we first find the derivative of G with respect to P_1 :

$$\frac{\partial G}{\partial P_1} = \frac{\partial}{\partial P_1} \left(\frac{r}{g} \sinh(gL) \right)^2 = \frac{\partial}{\partial P_1} \left(\frac{r}{g} \right)^2 \sinh^2(gL) + \left(\frac{r}{g} \right)^2 \frac{\partial}{\partial P_1} \sinh^2(gL) \quad (\text{A.1})$$

We proceed with A.1 by taking the partial derivative of Eq. 3.17(b) with respect to P_1 to obtain $dg/dP_1 = r(2\gamma P_2 - \kappa/4)/g$. Therefore, Eq. A.1 can be written as:

$$\frac{\partial G}{\partial P_1} = 2 \left(\frac{r}{g} \right)^2 \sinh^2(gL) \left(\frac{1}{2P_1} - \frac{\gamma}{g} (2P_2 - \kappa/4) + \frac{\gamma L}{g} (2P_2 - \kappa/4) \coth(gL) \right) \quad (\text{A.2})$$

Referring to the definition of Eq. 3.19 and using Eq. A.2, the gain sensitivity is obtained as:

$$S_{P_1}^G = \frac{\partial G / \partial P_1}{G} = \frac{1}{P_1} - \frac{\gamma}{g^2} (4\gamma P_2 - \kappa/2) + \frac{\gamma L}{g} (4\gamma P_2 - \kappa/2) \coth(gL) \quad (\text{A.3})$$

The same calculation for $S_{P_2}^G$ leads to a similar expression as Eq. A.3 except that P_1 is replaced with P_2 and vice versa.

Equation A.3 has a determinate value for any phase-matching condition in the range $-3 < \Delta\beta/\gamma P_0 < 1$. However, when $\Delta\beta/\gamma P_0 = -3, 1$ it leads to an indeterminate form of $0/0$. To evaluate $S_{P_1}^G$ when $\Delta\beta/\gamma P_0 = -3, 1$ which leads to $g = 0$, one can replace $\coth(gL)$ with its Laurant series expansion in the range $0 < |gL| < \pi$ i.e. $\coth(gL) = \frac{1}{gL} + \frac{gL}{3} + O((gL)^3)$. Therefore, Eq. A.3 can be rewritten as:

$$S_{P_1}^G = \frac{1}{P_1} + (4\gamma^2 P_2 - \kappa\gamma/2) \times \left(\frac{L^2}{3} + \frac{L}{g} O(gL)^3 \right), \quad 0 < |gL| < \pi \quad (\text{A.4})$$

from which we obtain:

$$\lim_{\Delta\beta/\gamma P_0 \rightarrow -3} S_{P_1}^G = \frac{1}{P_1} + \frac{\gamma^2 L^2 (4P_2 + P_0)}{3}, \quad \lim_{\Delta\beta/\gamma P_0 \rightarrow 1} S_{P_1}^G = \frac{1}{P_1} + \frac{\gamma^2 L^2 (4P_2 - P_0)}{3} \quad (\text{A.5})$$

It worth noting that the gain sensitivity at $\Delta\beta/\gamma P_0 = -3$ is the supermum of $S_{P_1}^G$. As a result, based on the definition of of gain sensitivity it is assured the generated pulses have lowest *DC* when operating at $\Delta\beta/\gamma P_0 = -3$. To verify this theory we employ the approximation of Eq. A.3 when $\pi < |gL|$ leading to:

$$S_{P_1}^G = \frac{1}{P_1} + (4\gamma^2 P_2 - \kappa\gamma/2) \times \left(\frac{L}{g} - \frac{1}{g^2} \right), \quad \pi < |gL| \quad (\text{A.6})$$

Equation A.6 can be analyzed together with Eq. A.4 to show that the gain sensitivity at $\Delta\beta/\gamma P_0 = -3$ is an upper bound for $S_{P_1}^G$. In fact the second term at the right side of both equations consists of two multiplied terms. In one hand the first term $(4\gamma^2 P_2 - \kappa\gamma/2)$ is maximized at $\Delta\beta/\gamma P_0 = -3$ in the range $-3 \leq \Delta\beta/\gamma P_0 \leq 1$. On the other hand the second term takes the maximum value $L^2/3$ for all $0 < |gL|$. Therefore, the expression $1/P_1 + \gamma^2 L^2 (4P_2 + P_0)/3$ that is derived in Eq. A.5 would be the supermum of $S_{P_1}^G$.

A.2 Pulse Shape

In this section we obtain the expression for the idler pulses at different values of $\Delta\beta/\gamma P_0 = -3, -1, 1$. Since the pumps are modulated sinusoidally referring to Eq. 3.21 we can write:

$$\begin{aligned} r(t) &= \gamma P_0 \cos^2(\pi f_R t) \\ \kappa(t) &= \Delta\beta + \gamma P_0 \cos^2(\pi f_R t) \end{aligned} \quad (\text{A.7})$$

Using Eq. A.7, we can obtain the values of $\kappa(t)$ at $\Delta\beta/\gamma P_0 = m$ as following:

$$\Delta\beta/\gamma P_0 = m : \kappa(t) = \gamma P_0 (m + \cos^2(\pi f_R t)) \quad (\text{A.8})$$

According to Eqs. A.8, A.7 and 3.17 and assuming that the pump expression can be replaced with its development to the second order in t , the g factor can be approximated as:

$$\begin{aligned} \Delta\beta/\gamma P_0 = -3 : g &\approx j\sqrt{3}\gamma P_0 |\sin(\pi f_R t)| \approx j\sqrt{3}\pi\gamma P_0 f_R t \\ \Delta\beta/\gamma P_0 = -1 : g &\approx \gamma P_0 (1 - \sin^2(\pi f_R t))^{1/2} \approx \gamma P_0 (1 - (\pi f_R t)^2) \\ \Delta\beta/\gamma P_0 = 1 : g &\approx j\gamma P_0 |\sin(\pi f_R t)| = j\pi\gamma P_0 f_R t \end{aligned} \quad (\text{A.9})$$

from Eqs. A.9 and 3.16 we can write the idler pulse expression as:

$$\begin{aligned} \Delta\beta/\gamma P_0 = -3 : P_{out}(t) &\approx P_S (\gamma P_0 L)^2 \text{sinc}^2(\sqrt{3}\gamma P_0 L f_R t) \\ \Delta\beta/\gamma P_0 = -1 : P_{out}(t) &\approx P_S \exp(2\gamma P_0 L)/4 \times \exp(-2\gamma P_0 L (\pi f_R t)^2) \\ \Delta\beta/\gamma P_0 = 1 : P_{out}(t) &\approx P_S (\gamma P_0 L)^2 \text{sinc}^2(\gamma P_0 L f_R t) \end{aligned} \quad (\text{A.10})$$

Bibliography

- [1] R.-J. Essiambre and R. W. Tkach, "Capacity trends and limits of optical communication networks," *Proceedings of the IEEE*, vol. 100, no. 5, pp. 1035–1055, 2012.
- [2] R. W. Tkach, "Scaling optical communications for the next decade and beyond," *Bell Labs Technical Journal*, vol. 14, no. 4, pp. 3–9, 2010.
- [3] P. J. Winzer, "High-spectral-efficiency optical modulation formats," *Lightwave Technology, Journal of*, vol. 30, no. 24, pp. 3824–3835, 2012.
- [4] R.-J. Essiambre, G. J. Foschini, G. Kramer, and P. J. Winzer, "Capacity limits of information transport in fiber-optic networks," *Physical review letters*, vol. 101, no. 16, p. 163901, 2008.
- [5] R.-J. Essiambre, G. Kramer, P. J. Winzer, G. J. Foschini, and B. Goebel, "Capacity limits of optical fiber networks," *Lightwave Technology, Journal of*, vol. 28, no. 4, pp. 662–701, 2010.
- [6] G. Bosco, V. Curri, A. Carena, P. Poggiolini, and F. Forghieri, "On the performance of nyquist-wdm terabit superchannels based on pm-bpsk, pm-qpsk, pm-8qam or pm-16qam subcarriers," *Lightwave Technology, Journal of*, vol. 29, no. 1, pp. 53–61, 2011.
- [7] R. Schmogrow, M. Winter, M. Meyer, D. Hillerkuss, S. Wolf, B. Baeuerle, A. Ludwig, B. Nebendahl, S. Ben-Ezra, J. Meyer *et al.*, "Real-time nyquist pulse generation beyond 100 gbit/s and its relation to ofdm," *Optics Express*, vol. 20, no. 1, pp. 317–337, 2012.
- [8] H. Nyquist, "Certain topics in telegraph transmission theory," *American Institute of Electrical Engineers, Transactions of the*, vol. 47, no. 2, pp. 617–644, 1928.
- [9] D. Hillerkuss, R. Schmogrow, M. Meyer, S. Wolf, M. Jordan, P. Kleinow, N. Lindenmann, P. C. Schindler, A. Melikyan, X. Yang *et al.*, "Single-laser 32.5 tbit/s nyquist wdm transmission," *Journal of Optical Communications and Networking*, vol. 4, no. 10, pp. 715–723, 2012.
- [10] R. Ramaswami and K. N. Sivarajan, "Routing and wavelength assignment in all-optical networks," *IEEE/ACM Transactions on Networking (TON)*, vol. 3, no. 5, pp. 489–500, 1995.

Bibliography

- [11] M. Kovačević and A. Acampora, "Benefits of wavelength translation in all-optical clear-channel networks," *Selected Areas in Communications, IEEE Journal on*, vol. 14, no. 5, pp. 868–880, 1996.
- [12] R. J. S. Pedersen, B. Mikkelsen, B. Jorgensen, M. Nissov, K. E. Stubkjaer, K. Wunstel, K. Daub, E. Lach, G. Laube, W. Idler *et al.*, "Wdm cross-connect cascade based on all-optical wavelength converters for routing and wavelength slot interchanging using a reduced number of internal wavelengths," in *Optical Fiber Communication Conference and Exhibit, 1998. OFC'98., Technical Digest*. IEEE, 1998, pp. 58–59.
- [13] P. Barnsley and P. Fiddyment, "Wavelength conversion from 1.3 to 1.55 μm using split contact optical amplifiers," *Photonics Technology Letters, IEEE*, vol. 3, no. 3, pp. 256–258, 1991.
- [14] K. Shimizu, T. Horiguchi, and Y. Koyamada, "Technique for translating light-wave frequency by using an optical ring circuit containing a frequency shifter," *Optics letters*, vol. 17, no. 18, pp. 1307–1309, 1992.
- [15] C. R. Giles, T. Li, T. H. Wood, C. A. Burrus, and D. A. Miller, "All-optical regenerator," *Electronics letters*, vol. 24, no. 14, pp. 848–850, 1988.
- [16] M. Jinno and M. Abe, "All-optical regenerator based on nonlinear fibre sagnac interferometer," *Electronics Letters*, vol. 28, no. 14, pp. 1350–1352, 1992.
- [17] J. Lucek and K. Smith, "All-optical signal regenerator," *Optics letters*, vol. 18, no. 15, pp. 1226–1228, 1993.
- [18] R. Schmogrow, D. Hillerkuss, S. Wolf, B. Bäuerle, M. Winter, P. Kleinow, B. Nebendahl, T. Dippon, P. Schindler, C. Koos *et al.*, "512qam nyquist sinc-pulse transmission at 54 gbit/s in an optical bandwidth of 3 ghz," *Optics express*, vol. 20, no. 6, pp. 6439–6447, 2012.
- [19] T. Hirooka, P. Ruan, P. Guan, and M. Nakazawa, "Highly dispersion-tolerant 160 gbaud optical nyquist pulse tdm transmission over 525 km," *Optics express*, vol. 20, no. 14, pp. 15 001–15 007, 2012.
- [20] M. Nakazawa, T. Hirooka, P. Ruan, and P. Guan, "Ultrahigh-speed "orthogonal" tdm transmission with an optical nyquist pulse train," *Optics express*, vol. 20, no. 2, pp. 1129–1140, 2012.
- [21] A. Vedadi, M. A. Shoaie, C.-S. Brès *et al.*, "Near-nyquist optical pulse generation with fiber optical parametric amplification," *Optics express*, vol. 20, no. 26, pp. B558–B565, 2012.
- [22] K. Harako, D. O. Otuya, K. Kasai, T. Hirooka, and M. Nakazawa, "Novel ultrafast tdm demultiplexing scheme using orthogonality in coherent nyquist pulses," in *Optical Communication (ECOC), 2014 European Conference on*. IEEE, 2014, pp. 1–3.

-
- [23] J. R. Stroud and M. A. Foster, "All-optical demultiplexing of nyquist otdm using a nyquist gate," in *CLEO: Science and Innovations*. Optical Society of America, 2014, pp. SW1J–4.
- [24] D. K. Cheng, *Field and wave electromagnetics*. Addison-wesley New York, 1989, vol. 2.
- [25] G. P. Agrawal, *Nonlinear fiber optics*. Academic press, 2007.
- [26] S. Guo, F. Wu, S. Albin, H. Tai, and R. Rogowski, "Loss and dispersion analysis of microstructured fibers by finite-difference method," *Optics Express*, vol. 12, no. 15, pp. 3341–3352, 2004.
- [27] P. Russell, "Photonic crystal fibers," *science*, vol. 299, no. 5605, pp. 358–362, 2003.
- [28] A. C. Turner, C. Manolatou, B. S. Schmidt, M. Lipson, M. A. Foster, J. E. Sharping, and A. L. Gaeta, "Tailored anomalous group-velocity dispersion in silicon channel waveguides," *Optics express*, vol. 14, no. 10, pp. 4357–4362, 2006.
- [29] S. Le Floch and P. Cambon, "Theoretical evaluation of the brillouin threshold and the steady-state brillouin equations in standard single-mode optical fibers," *JOSA A*, vol. 20, no. 6, pp. 1132–1137, 2003.
- [30] D. Fishman, J. Nagel *et al.*, "Degradations due to stimulated brillouin scattering in multigigabit intensity-modulated fiber-optic systems," *Lightwave Technology, Journal of*, vol. 11, no. 11, pp. 1721–1728, 1993.
- [31] S. Korotky, P. Hansen, L. Eskildsen, and J. Veselka, "Efficient phase modulation scheme for suppressing stimulated brillouin scattering," in *Tech. Dig. Int. Conf. Integrated Optics and Optical Fiber Communications*, vol. 2, 1995, pp. 110–111.
- [32] J. Hansryd, F. Dross, M. Westlund, P. Andrekson, and S. Knudsen, "Increase of the sbs threshold in a short highly nonlinear fiber by applying a temperature distribution," *Journal of lightwave technology*, vol. 19, no. 11, p. 1691, 2001.
- [33] M.-J. Li, X. Chen, J. Wang, S. Gray, A. Liu, J. A. Demeritt, A. B. Ruffin, A. M. Crowley, D. T. Walton, and L. A. Zenteno, "Al/ge co-doped large mode area fiber with high sbs threshold," *Optics Express*, vol. 15, no. 13, pp. 8290–8299, 2007.
- [34] T. Tanemura, H. C. Lim, and K. Kikuchi, "Suppression of idler spectral broadening in highly efficient fiber four-wave mixing by binary-phase-shift-keying modulation of pump wave," *Photonics Technology Letters, IEEE*, vol. 13, no. 12, pp. 1328–1330, 2001.
- [35] R. G. Smith, "Optical power handling capacity of low loss optical fibers as determined by stimulated raman and brillouin scattering," *Applied Optics*, vol. 11, no. 11, pp. 2489–2494, 1972.
- [36] Y. Emori, K. Tanaka, and S. Namiki, "100 nm bandwidth flat-gain raman amplifiers pumped and gain-equalised by 12-wavelength-channel wdm laser diode unit," *Electronics letters*, vol. 35, no. 16, pp. 1355–1356, 1999.

Bibliography

- [37] T. Sylvestre, H. Maillotte, E. Lantz, and P. Tchofo Dinda, "Raman-assisted parametric frequency conversion in a normally dispersive single-mode fiber," *Optics letters*, vol. 24, no. 22, pp. 1561–1563, 1999.
- [38] R. H. Stolen, W. Tomlinson, H. Haus, and J. Gordon, "Raman response function of silica-core fibers," *JOSA B*, vol. 6, no. 6, pp. 1159–1166, 1989.
- [39] O. V. Sinkin, R. Holzlöhner, J. Zweck, and C. R. Menyuk, "Optimization of the split-step fourier method in modeling optical-fiber communications systems," *Lightwave Technology, Journal of*, vol. 21, no. 1, pp. 61–68, 2003.
- [40] T. R. Taha and M. I. Ablowitz, "Analytical and numerical aspects of certain nonlinear evolution equations. ii. numerical, nonlinear schrödinger equation," *Journal of Computational Physics*, vol. 55, no. 2, pp. 203–230, 1984.
- [41] R. Tang, J. Lasri, P. S. Devgan, V. Grigoryan, P. Kumar, and M. Vasilyev, "Gain characteristics of a frequency nondegenerate phase-sensitive fiber-optic parametric amplifier with phase self-stabilized input," *Optics Express*, vol. 13, no. 26, pp. 10 483–10 493, 2005.
- [42] M. Marhic, F. Yang, L. Kazovsky, and Y. Park, "Broadband fiber-optical parametric amplifiers and wavelength converters with low-ripple chebyshev gain spectra," *Optics letters*, vol. 21, no. 17, pp. 1354–1356, 1996.
- [43] A. Mussot, E. Lantz, A. Durecu-Legrand, C. Simonneau, D. Bayard, T. Sylvestre, and H. Maillotte, "Zero-dispersion wavelength mapping in short single-mode optical fibers using parametric amplification," *arXiv preprint physics/0606026*, 2006.
- [44] L. Provino, A. Mussot, E. Lantz, T. Sylvestre, and H. Maillotte, "Broadband and flat parametric amplifiers with a multisection dispersion-tailored nonlinear fiber arrangement," *JOSA B*, vol. 20, no. 7, pp. 1532–1537, 2003.
- [45] M. E. Marhic, *Fiber optical parametric amplifiers, oscillators and related devices*. Cambridge university press, 2008.
- [46] J. Chavez Boggio, J. Marconi, S. Bickham, and H. Fragnito, "Spectrally flat and broadband double-pumped fiber optical parametric amplifiers," *Optics express*, vol. 15, no. 9, pp. 5288–5309, 2007.
- [47] M. Onishi, T. Okuno, T. Kashiwada, S. Ishikawa, N. AKASAKA, and M. Nishimura, "Highly nonlinear dispersion shifted fiber and its application to broadband wavelength converter," in *IEE conference publication*. Institution of Electrical Engineers, 1997, pp. 115–118.
- [48] M. Onishi, T. Okuno, T. Kashiwada, S. Ishikawa, N. Akasaka, and M. Nishimura, "Highly nonlinear dispersion-shifted fibers and their application to broadband wavelength converter," *Optical Fiber Technology*, vol. 4, no. 2, pp. 204–214, 1998.

-
- [49] K. P. Hansen and A. O. Bjarklev, "Nonlinear photonic crystal fibers: Design and applications," Ph.D. dissertation, unknown.
- [50] R. Tang, J. Lasri, P. Devgan, J. E. Sharping, and P. Kumar, "Microstructure-fibre-based optical parametric amplifier with gain slope of 200 db/w/km in the telecom range," *Electronics Letters*, vol. 39, no. 2, pp. 195–196, 2003.
- [51] E. Yoshida, N. Shimizu, and M. Nakazawa, "A 40-ghz 0.9-ps regeneratively mode-locked fiber laser with a tuning range of 1530-1560 nm," *Photonics Technology Letters, IEEE*, vol. 11, no. 12, pp. 1587–1589, 1999.
- [52] A. Vedadi, A. M. Ariaei, M. M. Jadidi, J. A. Salehi *et al.*, "Theoretical study of high repetition rate short pulse generation with fiber optical parametric amplification," *Journal of Lightwave Technology*, vol. 30, no. 9, pp. 1263–1268, 2012.
- [53] E. Lichtman, A. Friesem, R. G. Waarts, and H. Yaffe, "Exact solution of four-wave mixing of copropagating light beams in a kerr medium," *JOSA B*, vol. 4, no. 11, pp. 1801–1805, 1987.
- [54] D. Dahan and G. Eisenstein, "Tunable all optical delay via slow and fast light propagation in a raman assisted fiber optical parametric amplifier: a route to all optical buffering," *Optics express*, vol. 13, no. 16, pp. 6234–6249, 2005.
- [55] A. Mussot, A. Kudlinski, E. Louvergneaux, M. Kolobov, and M. Taki, "Impact of the third-order dispersion on the modulation instability gain of pulsed signals," *Optics letters*, vol. 35, no. 8, pp. 1194–1196, 2010.
- [56] T. Torounidis, M. Karlsson, P. Andrekson *et al.*, "Fiber optical parametric amplifier pulse source: Theory and experiments," *Lightwave Technology, Journal of*, vol. 23, no. 12, pp. 4067–4073, 2005.
- [57] A. A. Vedadi, M. A. Shoaie, and C.-S. Brès, "Experimental investigation of pulse generation with one-pump fiber optical parametric amplification," *Optics express*, vol. 20, no. 24, pp. 27 344–27 354, 2012.
- [58] C. J. McKinstrie, S. Radic, and A. Chraplyvy, "Parametric amplifiers driven by two pump waves," *IEEE Journal of selected topics in quantum electronics*, vol. 8, no. 3, pp. 538–547, 2002.
- [59] M. A. Shoaie, A. Mohajerin-Ariaei, A. Vedadi, C.-S. Brès *et al.*, "Wideband generation of pulses in dual-pump optical parametric amplifier: theory and experiment," *Optics express*, vol. 22, no. 4, pp. 4606–4619, 2014.
- [60] M. A. Shoaie, A. Vedadi, and C.-S. Brès, "Wideband uniform generation of shape-adjustable pulses in two-pump fiber optic parametric amplifier," in *Optical Communication (ECOC 2013), 39th European Conference and Exhibition on.* IET, 2013, pp. 1–3.

Bibliography

- [61] R. Stolen, J. Botineau, and A. Ashkin, "Intensity discrimination of optical pulses with birefringent fibers," *Optics Letters*, vol. 7, no. 10, pp. 512–514, 1982.
- [62] N. Doran and D. Wood, "Nonlinear-optical loop mirror," *Optics Letters*, vol. 13, no. 1, pp. 56–58, 1988.
- [63] F. Yaman, Q. Lin, G. P. Agrawal, and S. Radic, "Pump-noise transfer in dual-pump fiber-optic parametric amplifiers: walk-off effects," *Optics letters*, vol. 30, no. 9, pp. 1048–1050, 2005.
- [64] A. Bogris, D. Syvridis, P. Kylemark, P. Andrekson *et al.*, "Noise characteristics of dual-pump fiber-optic parametric amplifiers," *Lightwave Technology, Journal of*, vol. 23, no. 9, pp. 2788–2795, 2005.
- [65] P. Kylemark, J. Ren, M. Karlsson, S. Radic, C. J. McKinstrie, and P. A. Andrekson, "Noise in dual-pumped fiber-optical parametric amplifiers: theory and experiments," *Journal of Lightwave Technology*, vol. 25, no. 9, pp. 2837–2846, 2007.
- [66] O. Gerstel, M. Jinno, A. Lord, and S. B. Yoo, "Elastic optical networking: A new dawn for the optical layer?" *Communications Magazine, IEEE*, vol. 50, no. 2, pp. s12–s20, 2012.
- [67] A. H. Gnauck, E. Myslivets, M. Dinu, B. P. P. Kuo, P. Winzer, R. Jopson, N. Alic, A. Konczykowska, F. Jorge, J.-Y. Dupuy *et al.*, "All-optical tunable wavelength shifting of a 128-gbit/s 64-qam signal," in *European Conference and Exhibition on Optical Communication*. Optical Society of America, 2012, pp. Th-2.
- [68] G.-W. Lu, T. Sakamoto, and T. Kawanishi, "Wavelength conversion of optical 64qam through fwm in hnlf and its performance optimization by constellation monitoring," *Optics express*, vol. 22, no. 1, pp. 15–22, 2014.
- [69] H. Hu, R. Jopson, A. Gnauck, M. Dinu, S. Chandrasekhar, X. Liu, C. Xie, M. Montoliu, S. Randel, and C. McKinstrie, "Parametric amplification and wavelength conversion of a 2.048-tbit/s wdm pdm 16-qam signal," in *2014 The European Conference on Optical Communication (ECOC)*, 2014.
- [70] S. S. Haykin, *Digital communications*. Wiley New York, 1988.
- [71] D. Marcuse, "Pulse distortion in single-mode fibers. 3: Chirped pulses," *Applied optics*, vol. 20, no. 20, pp. 3573–3579, 1981.
- [72] D. Anderson and M. Lisak, "Analytic study of pulse broadening in dispersive optical fibers," *Physical Review A*, vol. 35, no. 1, p. 184, 1987.
- [73] D. Marcuse, "Pulse distortion in single-mode fibers. part 2," *Applied optics*, vol. 20, no. 17, pp. 2969–2974, 1981.

- [74] M. A. Shoaie, A. Vedadi, C.-S. Brès *et al.*, “Broadband uniform wavelength conversion and time compression of wdm channels,” in *CLEO: Science and Innovations*. Optical Society of America, 2015, pp. SM2M–4.
- [75] R. INOHARA, K. NISHIMURA, M. TSURUSAWA, M. USAMI, and S. AKIBA, “40 gbit/s transmission with all-optical 3r regeneration using two-stage soa-based polarization discriminated switch with assist light injection,” *IEICE transactions on electronics*, vol. 87, no. 7, pp. 1106–1113, 2004.
- [76] M. Hayashi, T. Otani, H. Tanaka, and M. Suzuki, “Analysis on jitter tolerance of optical 3r regenerator,” *Photonics Technology Letters, IEEE*, vol. 15, no. 11, pp. 1609–1611, 2003.
- [77] J. Nakagawa, M. Marhic, and L. Kazovsky, “All-optical 3r regeneration technique using injection-locking in gain-switched dfb-ld,” *Electronics Letters*, vol. 37, no. 4, pp. 231–232, 2001.
- [78] D. Dahan, R. Alizon, A. Bilenca, and G. Eisenstein, “Optical noise reduction in inter-band raman mediated wavelength conversion,” *Electronics Letters*, vol. 39, no. 3, pp. 307–309, 2003.
- [79] Y. Su, L. Wang, A. Agarwal, and P. Kumar, “Simultaneous 3r regeneration and wavelength conversion using a fiber-parametric limiting amplifier,” in *Proc. Opt. Fiber Commun. Conf*, vol. 1, 2001.
- [80] O. Leclerc, B. Dany, D. Rouvillain, P. Brindel, E. Desurvire, C. Duchet, A. Shen, F. Devaux, A. Coquelin, M. Goix *et al.*, “Simultaneously regenerated 4 × 40 gbit/s dense wdm transmission over 10,000 km using single 40 ghz inp mach-zehnder modulator,” *Electronics Letters*, vol. 36, no. 18, pp. 1574–1575, 2000.
- [81] E. Desurvire, O. Leclerc, and O. Audouin, “Synchronous in-line regeneration of wavelength-division multiplexed solitons signals in optical fibers,” *Optics letters*, vol. 21, no. 14, pp. 1026–1028, 1996.
- [82] C. Kouloumentas, L. Provost, F. Parmigiani, S. Tsolakidis, P. Petropoulos, I. Tomkos, and D. J. Richardson, “Four-channel all-fiber dispersion-managed 2r regenerator,” *Photonics Technology Letters, IEEE*, vol. 20, no. 13, pp. 1169–1171, 2008.
- [83] L. Provost, F. Parmigiani, P. Petropoulos, D. Richardson, K. Mukasa, M. Takahashi, J. Hiroishi, and M. Tadakuma, “Investigation of four-wavelength regenerator using polarization-and direction-multiplexing,” *Photonics Technology Letters, IEEE*, vol. 20, no. 20, pp. 1676–1678, 2008.
- [84] T. Nguyen, M. Gay, L. Bramerie, T. Chartier, J.-C. Simon, and M. Joindot, “Noise reduction in 2r-regeneration technique utilizing self-phase modulation and filtering,” *Optics express*, vol. 14, no. 5, pp. 1737–1747, 2006.

Bibliography

- [85] M. Gao, J. Kurumida, and S. Namiki, "43-gb/s operation of wavelength-tunable optical parametric regenerator," *Photonics Technology Letters, IEEE*, vol. 23, no. 11, pp. 718–720, 2011.
- [86] K. Solis-Trapala, J. Kurumida, M. Gao, T. Inoue, and S. Namiki, "Tunable optical parametric regenerator assessment in a 43 gb/s rz-dpsk signal transmission link," *Photonics Technology Letters, IEEE*, vol. 26, no. 6, pp. 629–632, 2014.
- [87] C. Yu, T. Luo, B. Zhang, Z. Pan, M. Adler, Y. Wang, J. McGeehan, and A. Willner, "3r regeneration of a 40-gbit/s optical signal by optical parametric amplification in a highly-nonlinear fiber," in *Optical Fiber Communication Conference*. Optical Society of America, 2005, p. OTuO1.
- [88] P. Guan, K. M. Røge, N.-K. Kjølner, H. C. H. Mulvad, H. Hu, M. Galili, T. Morioka, and L. K. Oxenløwe, "All-optical wdm regeneration of dpsk signals using optical fourier transformation and phase sensitive amplification," 2015.
- [89] A. Bogris and D. Syvridis, "40 gb/s all-optical regeneration based on the pump depletion effect in fiber parametric amplification," *Optical Fiber Technology*, vol. 14, no. 1, pp. 63–71, 2008.
- [90] J. C. Boggio, J. Marconi, and H. Fragnito, "Crosstalk in double-pumped fiber optic parametric amplifiers for wavelength division multiplexing systems," *Optics communications*, vol. 259, no. 1, pp. 94–103, 2006.
- [91] O. Leclerc, B. Lavigne, E. Balmeffre, P. Brindel, L. Pierre, D. Rouvillain, and F. Segueineau, "Optical regeneration at 40 gb/s and beyond," *Journal of Lightwave Technology*, vol. 21, no. 11, p. 2779, 2003.
- [92] F. Callegari, J. C. Boggio, and H. Fragnito, "Spurious four-wave mixing in two-pump fiber-optic parametric amplifiers," *Photonics Technology Letters, IEEE*, vol. 16, no. 2, pp. 434–436, 2004.
- [93] M. Cai, X. Liu, J. Cui, P. Tang, and J. Peng, "Study on noise characteristic of gain-clamped erbium-doped fiber-ring lasing amplifier," *Photonics Technology Letters, IEEE*, vol. 9, no. 8, pp. 1093–1095, 1997.
- [94] B. P. Kuo, P. Chui, and K. K. Wong, "Comparison on crosstalk tolerance of rz-dpsk and rz-ook modulation format in fiber optical parametric amplifier," *ECOC 2007*, 2007.
- [95] B. P.-P. Kuo, P. Chui, and K. K.-Y. Wong, "A comprehensive study on crosstalk suppression techniques in fiber optical parametric amplifier by modulation format," *Selected Topics in Quantum Electronics, IEEE Journal of*, vol. 14, no. 3, pp. 659–665, 2008.
- [96] D. Hillerkuss, R. Schmogrow, T. Schellinger, M. Jordan, M. Winter, G. Huber, T. Vallaitis, R. Bonk, P. Kleinow, F. Frey *et al.*, "26 tbit s⁻¹ line-rate super-channel transmission utilizing all-optical fast fourier transform processing," *Nature Photonics*, vol. 5, no. 6, pp. 364–371, 2011.

-
- [97] T. Hirooka and M. Nakazawa, "Linear and nonlinear propagation of optical nyquist pulses in fibers," *Optics express*, vol. 20, no. 18, pp. 19 836–19 849, 2012.
- [98] G. Bosco, A. Carena, V. Curri, P. Poggiolini, and F. Forghieri, "Performance limits of nyquist-wdm and co-ofdm in high-speed pm-qpsk systems," *Photonics Technology Letters, IEEE*, vol. 22, no. 15, pp. 1129–1131, 2010.
- [99] H. Nguyen Tan, T. Inoue, and S. Namiki, "Pass-drop operations of 4x172gb/s nyquist otdm-wdm over cascade of wsss using distributed matched filtering," in *Optical Fiber Communication Conference*. Optical Society of America, 2013, pp. JW2A–50.
- [100] C. Finot, L. Provost, P. Petropoulos, and D. J. Richardson, "Parabolic pulse generation through passive nonlinear pulse reshaping in a normally dispersive two segment fiber device," *Optics express*, vol. 15, no. 3, pp. 852–864, 2007.
- [101] M. A. Soto, M. Alem, M. A. Shoaie, A. Vedadi, C.-S. Brès, L. Thévenaz, and T. Schneider, "Optical sinc-shaped nyquist pulses of exceptional quality," *Nature communications*, vol. 4, 2013.
- [102] M. A. Soto, M. Alem, M. A. Shoaie, A. Vedadi, C. S. Brès, L. Thévenaz, T. Schneider *et al.*, "Generation of nyquist sinc pulses using intensity modulators," in *CLEO: Science and Innovations*. Optical Society of America, 2013, pp. CM4G–3.
- [103] J. G. Proakis and M. Salehi, *Digital communications*. McGraw-Hill, 2008.
- [104] B. Washburn, R. Fox, N. Newbury, J. Nicholson, K. Feder, P. Westbrook, and C. Jørgensen, "Fiber-laser-based frequency comb with a tunable repetition rate," *Optics express*, vol. 12, no. 20, pp. 4999–5004, 2004.
- [105] A. Bartels, R. Gebs, M. S. Kirchner, and S. A. Diddams, "Spectrally resolved optical frequency comb from a self-referenced 5 ghz femtosecond laser," *Optics letters*, vol. 32, no. 17, pp. 2553–2555, 2007.
- [106] R. Wu, V. Supradeepa, C. M. Long, D. E. Leaird, and A. M. Weiner, "Generation of very flat optical frequency combs from continuous-wave lasers using cascaded intensity and phase modulators driven by tailored radio frequency waveforms," *Optics letters*, vol. 35, no. 19, pp. 3234–3236, 2010.
- [107] S. Ozharar, F. Quinlan, I. Ozdur, S. Gee, and P. Delfyett, "Ultraflat optical comb generation by phase-only modulation of continuous-wave light," *IEEE Photonics Technology Letters*, vol. 1, no. 20, pp. 36–38, 2008.
- [108] T. Yang, J. Dong, S. Liao, D. Huang, and X. Zhang, "Comparison analysis of optical frequency comb generation with nonlinear effects in highly nonlinear fibers," *Optics express*, vol. 21, no. 7, pp. 8508–8520, 2013.

Bibliography

- [109] V. Ataie, B. P.-P. Kuo, E. Myslivets, and S. Radic, "Generation of 1500-tone, 120nm-wide ultraflat frequency comb by single cw source," in *Optical Fiber Communication Conference*. Optical Society of America, 2013, pp. PDP5C-1.
- [110] Z. Jiang, D. Seo, D. E. Leaird, and A. M. Weiner, "Spectral line-by-line pulse shaping," *Optics letters*, vol. 30, no. 12, pp. 1557-1559, 2005.
- [111] Z. Jiang, C.-B. Huang, D. E. Leaird, and A. M. Weiner, "Optical arbitrary waveform processing of more than 100 spectral comb lines," *Nature Photonics*, vol. 1, no. 8, pp. 463-467, 2007.
- [112] G. A. Sefler and K.-i. Kitayama, "Frequency comb generation by four-wave mixing and the role of fiber dispersion," *Journal of lightwave technology*, vol. 16, no. 9, p. 1596, 1998.
- [113] G. Baxter, S. Frisken, D. Abakoumov, H. Zhou, I. Clarke, A. Bartos, and S. Poole, "Highly programmable wavelength selective switch based on liquid crystal on silicon switching elements," in *Optical Fiber Communication Conference*. Optical Society of America, 2006, p. OTuF2.
- [114] S. Cordette, A. Vedadi, M. A. Shoaie, and C.-S. Brès, "Bandwidth and repetition rate programmable nyquist sinc-shaped pulse train source based on intensity modulators and four-wave mixing," *Optics letters*, vol. 39, no. 23, pp. 6668-6671, 2014.
- [115] D. Kong, J. Zang, M. Yu, Y. Li, S. Zhou, H. Guo, and J. Wu, "A novel detection scheme for nyquist optical time-division multiplexed signal with coherent matched sampling," in *Optical Fiber Communication Conference*. Optical Society of America, 2015, pp. W3C-4.
- [116] M. A. Shoaie, A. Vedadi, and C.-S. Brès, "A simple all-optical format transparent time and wavelength demultiplexing technique for wdm & orthogonal-tdm nyquist channels," in *Optical Communication (ECOC), 2015 European Conference on*. IEEE, 2015, pp. 1-3.
- [117] J. Azaa, "Ultrafast analog all-optical signal processors based on fiber-grating devices," *IEEE Photonics Journal*, vol. 3, no. 2, pp. 359-386, 2010.
- [118] A. J. Lowery, C. Zhu, E. Viterbo, and B. Corcoran, "All-optical generation of dft-s-ofdm superchannels using periodic sinc pulses," *Optics express*, vol. 22, no. 22, pp. 27 026-27 041, 2014.

List of Acronyms

AOWC	All-optical wavelength conversion
ASE	Amplified spontaneous emission
AWG	Arbitrary waveform generator
BER	Bit-error rate
BERT	Bit-error rate tester
BRM	Bit rate multiplier
CF	Compression factor
CW	Continuous wave
DC	Duty cycle
DCF	Dispersion compensated fiber
DPSK	Differential phase shift keying
DSF	Dispersion-shifted fiber
DSP	Digital signal processing
DWDM	Dense wavelength division multiplexing
ER	Extinction ratio
FEC	Forward error correction
FM	Frequency modulation
FOPA	Fiber optical parametric amplifier
FS	Four sideband
FWHM	Full-width half maximum
FWM	Four-wave mixing
GVD	Group velocity dispersion
HNLF	Highly nonlinear fiber
IM	Intensity modulation
ISI	Inter-symbol interference
ITU	International telecommunication union
LCM	Least common
MI	Modulation instability
MMF	Multi mode fiber
MZM	Mach-Zehnder modulator
NLSE	Nonlinear Schrodinger equation
NRZ	Non-return to zero
OEO	Optical-electrical-optical
OFDM	Orthogonal frequency division multiplexing
OOK	On-off keying
OSA	Optical spectrum analyzer
O-TDM	Orthogonal time division multiplexing
PCF	Photonic crystal fiber
PI	Phase-insensitive
PM	Phase modulation

PRBS	Pseudo random bit sequence
PS	Phase-sensitive
PSD	Power spectral density
RF	Radio frequency
RIN	Relative intensity noise
RMS	Root mean square
ROADM	Reconfigurable optical add-drop multiplexer
RPD	Relative pump depletion
SBS	Stimulated Brillouin scattering
SMF	Single mode fiber
SPM	Self-phase modulation
SSF	Split-step Fourier
SVE	Slowly varying envelop
TB	Time-Bandwidth
TDM	Time division multiplexing
TF	Transfer function
TL	Tunable laser
TS	Two sideband
VOA	Variable optical attenuator
WC	Wavelength conversion
WDM	Wavelength division multiplexing
WSS	Wavelength selective switch
XPM	Cross-phase modulation
ZDW	Zero dispersion wavelength

AMIN SHOAIE

Ave. des Boveresses, 92
1010 Lausanne, Switzerland
Mobile: +41786298775
Email: mashoaie@gmail.com

Linked in



EDUCATION

- **PhD in Photonics, Spring 2012 – Now (Expected Feb. 2016)**
École Polytechnique Fédérale de Lausanne (EPFL), Lausanne, Switzerland.
- **M.Sc. in Electrical Engineering, Major: Communication Systems, 2008 – 2010**
Sharif University of Technology, Tehran, Iran.
- **B.Sc. in Electrical Engineering, Major: Communication, 2004 – 2008**
Sharif University of Technology, Tehran, Iran.

HONORS AND AWARDS

- **Recipient of the grant** for graduate studies from Alcatel-Lucent, Bell-Labs mobile network center (Paris) 2011.
- **Ranked 5** in “Nationwide Graduate Examinations” for Masters in Electrical Engineering major, amongst more than **8000** participants, Iran, 2008.
- **Ranked 87** in “Nationwide Undergraduate Examinations” for Bachelors in Mathematics and Physics branch, amongst more than **350,000** participants, Iran, 2004.

PROFESSIONAL EXPERIENCE

ERICSSON, Summer 2011-Winter 2011 (6 months), full-time, Tehran, Iran.
ERICSSON provides the charging system of a major mobile company established by MTN in Iran.

- Working experience in a multi-national company with over 500 employees.
- Worked as “Network Engineer” for debugging the real time network functionality.
- Gained valuable experience in performance monitoring solutions. Obtained detailed knowledge in network software & hardware design.

Chabahr Maritime University, Spring 2011 (4 months), Chabahr, Iran.
Worked as “Lecturer”. Held class lectures and office hours, prepared homework and exams.

- Course title: Communication Circuits.
- Course title: Radar Systems.

PARMAN Group, Summer 2008-Winter 2011, (31 months), part-time 80%, Tehran, Iran.
The company is a successful startup in developing SDH transmission device technology.

- Worked as “Embedded Linux, C and C++ Programmer”.
- Implemented “Auto Protection Switching” standard (ITU G841) on our SDH systems supporting linear and ring topologies.
- Run and configured OSPF standard on our SDH device to enable data packet routing. I succeeded to correct a critical bug in the open source OSPF code.
- Developed significant teamwork and time-managing skills due to the complex and interconnected stages of the project.

NOKIA, Summer 2007, (3 months), internship, Tehran, Iran.

NOKIA runs a complete GSM network in Iran. One major issue of the company is the failure of some communication sites.

- Worked in a team responsible to troubleshoot transceiver stations (BTS) in Tehran.
- Upon receiving error reports, visited faulty sites and performed fault detection procedure to spot the source of error. If possible, we fixed the problem on-site.
- Developed systematic debugging skills in dealing with a complex system.

RESEARCH EXPERIENCE	<p>Photonic Systems Lab. Supervisor: Prof. C.S.Brès. Spring 2012-Now PhD student with research focus on non-linear optics and optical communication.</p> <ol style="list-style-type: none"> Studied (<i>experiment & theory</i>) dual-pump optical parametric amplifiers as a uniform wideband signal processing device for WDM channels. <ul style="list-style-type: none"> Demonstrated the first scalable method for 3R regeneration of WDM channels. Studied (<i>experiment & theory</i>) optical Nyquist pulse generation and detection. <ul style="list-style-type: none"> Demonstrated a novel and simple method to generate high quality Nyquist pulses. Developed a matched filter for our pulses as the optimum sampling scheme. My thesis results have led to 2 patents, 20 journal and conference publications including one publication in Nature Communication. Obtained significant skills in assembling and debugging fiber-optics experiments. Gained strong knowledge in linear & non-linear light propagation phenomena. <p>Optical Network Research Lab. Supervisor: Prof. J. A. Salehi. Summer 2009- 2010 Research Assistant, in a team to design and experiment a free-space optical link.</p> <ul style="list-style-type: none"> The prototype done by the team was a 2 Gb/s point-to-point link at 5 km distance. Automatic gain control, second order space diversity and CDMA technique was implemented to increase system stability and capacity. <p>A telescope was used as the receiver's front-end where the incoming light was detected and passed to a FPGA for further processing. I designed the electronic circuit at receiver's front-end and optimized the laser diversity scheme at transmitter.</p>
TECHNICAL EXPERTISE	<ul style="list-style-type: none"> Fiber Optics: Theory, Experiment, Simulation, Mathematical modeling. Computer Programming: C++ (expert), MATLAB (expert), LabVIEW, Java. Embedded Programming: Embedded Linux programming, VHDL, Verilog. Communication Systems: Knowledgeable in communication transmitters, receivers, channel noise and modulation techniques.
RELEVANT COURSES	<ul style="list-style-type: none"> École Polytechnique Fédérale de Lausanne: Lasers and optics of nano-structures, Advanced optics, Non-linear optics, Non-linear spectroscopy. Sharif University of Technology: Optical communication networks, Statistical optical communication, Advanced digital communication, Data networks, Wireless communication, Digital signal processing, Information theory.
EXTRA CREDITS	<ul style="list-style-type: none"> École Polytechnique Fédérale de Lausanne: Management of innovation and technology transfer, Venture challenge @EPFL, Principles of finance, Quantitative methods in finance, Scientific writing, Space mission design and operations.
EXTRA ACTIVITIES	<ul style="list-style-type: none"> Committee member of Iranian Student Association (IRSA) EPFL, Lausanne, 2013, 2105. Treasurer of EPFL Toastmaster club, Lausanne, 2013-14. Toastmaster communication manual completed (public speaking), 2012-14. Sports Volleyball, Squash. Reading biography books and Economist magazine.
LANGUAGE	English Fluent (C2), French Advanced (B2, in progress), German (A1), Persian Native
STATUS	29 years old, Single, Owner of Swiss permit-B

PUBLICATIONS

JOURNALS

- Cordette, S., Vedadi, A., **Shoaie, M. A.**, & Brès, C. S. "Bandwidth and repetition rate programmable Nyquist sinc-shaped pulse train source based on intensity modulators and four-wave mixing". *Optics letters*, (2014).
- Alishahi, F., Vedadi, A., **Shoaie, M.A.**, et al. "Power evolution along phase-sensitive parametric amplifiers: an experimental survey". *Optics letters*, (2014).
- Khazraei, S., **Shoaie, M. A.**, & Pakravan, M. R. "Efficient modulation technique for optical code division multiple access networks: differential pulse position modulation". *IET Optoelectronics*, (2014).
- **Shoaie, M. A.**, Mohajerin-Ariaei, A., et al. "Wideband generation of pulses in dual-pump optical parametric amplifier: theory and experiment". *Optics express*, (2014).
- Soto, M. A., Alem, M., **Shoaie, M. A.**, et al. "Optical sinc-shaped Nyquist pulses of exceptional quality". *Nature communications*, (2013).
- Vedadi, A., **Shoaie, M. A.**, & Brès, C. S. "Near-Nyquist optical pulse generation with fiber optical parametric amplification". *Optics express*, (2012).
- Vedadi, A., **Shoaie, M. A.**, et al. "Experimental investigation of pulse generation with one-pump fiber optical parametric amplification". *Optics express*, (2012).
- **Shoaie, M. A.**, Khazraei, S., & Pakravan, M. R. "Performance analysis of slotted ALOHA random access packet-switching optical CDMA networks using generalized optical orthogonal codes and M-ary overlapping PPM signaling". *Journal of Optical Communications and Networking*, (2011).

CONFERENCES

- Bres, C. S, **Shoaie, M. A.**, et al. "Advances in frequency comb synthesis-based Nyquist pulse-train carver and applications in optical systems". *ICTON* (2015).
- **Shoaie, M. A.**, et al. "A simple all-optical format transparent time and wavelength demultiplexing technique for WDM & Orthogonal-TDM Nyquist channels". *ECOC* (2015).
- **Shoaie, M. A.**, Vedadi, A., & Brès, C. S. "Broadband Uniform Wavelength Conversion and Time Compression of WDM Channels". *CLEO* (2015).
- Khazraei, S., **Shoaie, M. A.**, et al. "Packet switching unslotted optical CDMA system with variable length data traffic: Throughput, delay and stability analysis". *IST, IEEE* (2014).
- Bres, C. S., Soto, M., Alem, M., **Shoaie M. A.**, et al. "Towards highest spectral efficiency: Optical sinc-shaped Nyquist pulses generation from rectangular frequency comb". *ICTON, IEEE* (2014).
- Vedadi, A., **Shoaie, M. A.**, Soto, M. A., et al. "Effect of dispersion fluctuations on longitudinal gain evolution in phase-sensitive parametric amplifiers". *CLEO* (2014).
- Soto, M. A., Alem, M., **Shoaie, M. A.**, Vedadi, A., Brès, C. S., Schneider, T., & Thévenaz, L. "Optical sinc-shaped Nyquist pulses with very low roll-off generated from a rectangular frequency comb". *Asia Communications and Photonics Conference* (2013).
- Soto, M. A., Alem, M., **Shoaie, M. A.**, Vedadi, A., Brès, C. S., Thévenaz, L., & Schneider, T. "Highly tunable method to generate sinc-shaped Nyquist pulses from a rectangular frequency comb". *Signal Processing in Photonic Communications* (2013).
- Soto, M. A., Alem, M., **Shoaie, M. A.**, Vedadi, A., Brès, C. S., Thévenaz, L., & Schneider, T. "Generation of Nyquist sinc pulses using intensity modulators". *CLEO* (2013).
- **Shoaie, M. A.**, Vedadi, A., & Brès, C. S. "Wideband uniform generation of shape-adjustable pulses in two-pump fiber optic parametric amplifier". *ECOC* (2013).
- Vedadi, A., **Shoaie, M. A.**, & Bres, C. S. "Near Nyquist sinc optical pulse generation with fiber optical parametric amplification". *ECOC* (2012).
- Alishahi, F., Vedadi, A., **Shoaie, M. A.**, Mehrany, K., & Salehi, J. A. "Low Resolution Distributed Measurement of Fiber Optical Parametric Amplifiers Gain". *OFC* (2012).
- Vedadi, A., Ranjbar-Zefreh, M., Ziyadi, M., Naimi, S. T., **Shoaie, A. M.**, & Salehi, J. A. "All-fiber autocorrelator based on parametric amplification". *OFC* (2011)